Tailoring Wetting Behavior at Extremes

by

Kyle Lucas Wilke

SM, Mechanical Engineering (2016)

Massachusetts Institute of Technology

BS, Mechanical Engineering (2013)

University of Wisconsin, Madison

Submitted to the Department of Mechanical Engineering in

Partial Fulfillment of the Requirements for the Degree of

Doctor of Philosophy in Mechanical Engineering

at the

Massachusetts Institute of Technology

June 2019

Signature redacted

Signature of Author:. .....
Department of Mechanical Engineering
May 24, 2019

Signature redacted

Certified by:..... .....
Evelyn N. Wang
Gail E. Kendall Professor of Mechanical Engineering
Thesis Supervisor

Signature redacted

Accepted by:... .....
Nicolas Hadjiconstantinou
Professor of Mechanical Engineering
Chairman, Department Committee on Graduate Theses

Intentionally blank page

Tailoring Wetting Behavior at Extremes

by

Kyle Lucas Wilke

Submitted to the Department of Mechanical Engineering on May 24th, 2019,
in Partial Fulfillment of the Requirements for the Degree of Doctor of Philosophy

Abstract

In the classical understanding of liquid interactions with surfaces, liquid/surface chemistry dictates wetting behavior, requiring use of specific materials to achieve desired behavior. This restriction creates a number of challenges this thesis aims to address. First, high-thermal-conductance, hydrophobic coatings are used enhance condensation heat transfer, but have poor durability due to the extreme environment. We developed polymer infused porous surfaces, which 1. provided a large surface area to adhere and constrain the polymer to the condenser surface and 2. created a network of high-thermal-conductivity material through the otherwise low-thermal-conductivity polymer. These surfaces enhanced condensation heat transfer 8x and showed no degradation over 200 days. Next, we demonstrated the use of reentrant microstructures and contact line pinning to shift the wetting paradigm, achieving any wetting behavior independent of the chemical nature of the surface and liquid, i.e., a surface with omniphobicity (repels all liquids), omniphilicity (wicks all liquids), switchability between repelling and wicking, and selectivity (repels or wicks only certain liquids). We then addressed robustness issues of reentrant microstructures during condensation on the surface by designing reentrant cavities with a pitch on the order of 100 nanometers. These dense, isolated cavities ensured nucleating droplets did not occur within all cavities and prevented liquid propagation within the structures, maintaining repellency to various liquids up to 10 °C below the dew point. We explored alternative fabrication methods for omniphobic, doubly reentrant microstructures by using intrinsic stresses in thin films to induce bending, achieving omniphobicity with standard microfabrication processes. Finally, we enhanced wicking in pillar arrays by allowing pillar pitch and diameter to vary along the surface, optimizing each section of the surface for minimal pressure drop, increasing the wicking performance relative to uniform arrays. Each chapter of this thesis is dedicated to one of these challenging areas in tailoring wetting behavior at extremes.

Thesis Committee:

Professor Evelyn N. Wang (Thesis Advisor/Chair), Department of Mechanical Engineering

Professor Rohit Karnik, Department of Mechanical Engineering

Professor Michael Short, Department of Nuclear Engineering

Intentionally blank page

Acknowledgements

First and foremost, I would like to express my deep gratitude for the opportunity to work with Evelyn in the DRL over the last 6 years. Her guidance and support, as well as the fantastic group of lab members she has brought together, made this experience incredibly rewarding. Thank you, Evelyn. You have been a role model in research and mentorship. The DRL fosters growth and collaboration, and so I would like to also thank each and every lab member. Discussion with and input from the group was invaluable. Without it this work would not have been possible. In particular, I would like to thank Banafsheh Barabadi and Dion Antao for guidance and support early on in my graduate studies, and Daniel Preston and Zhengmao Lu for discussing and shaping nearly every aspect of my work.

I would also like to thank my committee members Professor Rohit Karnik and Professor Michael Short. Your advice and suggestions helped improve and drive the direction of this research.

The rest of the staff and students, particularly within the MTL (Microsystems Technology Laboratories), NSL (Nanostructures Laboratory), and CNS (Center for Nanoscale Systems), have also been incredible. These communities have taught me so much.

I am grateful for the friendships I have made over these last years. You all have made MIT much more than an opportunity for academic growth. You all will do great things. I hope I can remain at least a small part of that moving forward.

Finally, to my family and Alex, who have been by my side for so long, my love for you only grows. To my siblings and Alex, words cannot express how proud I am of what you all have become. To my parents and grandparents, there is no doubt in my mind I am here today because of you, your love, and your support, thank you so much for everything. To all of you, your support and caring are truly a light in my life.

Intentionally blank page

Table of Contents

Intentionally blank page

List of Figures

Intentionally blank page

1. Introduction and Background

1.1 Motivation

In all aspects of our lives, liquids interact with surfaces. From every day examples like rain on our clothing and buildings or food in our pots and pans, to medical devices that need to interact with our bodies and blood, to some of our greatest engineering challenges such as sustainability of energy generation or providing clean water, a common thread is that control over how liquids behave on surfaces is crucial to performance. For this reason, significant research and development has focused on creating methods to control liquid/surface interactions, achieving liquid behaviors ranging from surfaces that spontaneously absorb liquids to surfaces that repel all liquids. However, many challenges remain, particularly when surfaces are exposed to extreme conditions, when extreme liquid behaviors are desired, and when extreme combinations of liquids and surface materials are used. Here, we introduce classical wetting behavior and key challenges created by this wetting paradigm that will be addressed within this thesis.

1.2 Classical Wetting Behavior

1.2.1 Flat, Homogeneous Surface Wetting Behavior

A liquid in contact with a solid surface assumes a particular shape in order to minimize its overall energy. For an ideal (flat and chemically homogeneous) solid surface the liquid shape, which can be characterized by the contact angle the liquid makes with the surface, θ, is determined by the surface tension of the different interfaces (Figure 1). In this scenario, a derivation for contact angle based on a force balance at the three-phase contact line is commonly used[1].

$$\gamma_{gs} = \gamma_{ls} + \gamma_{gl} \cos\theta \tag{1}$$

As evident from Eq. 1, the contact angle of a liquid is solely dependent on the surface tension, γ, of the different interfaces, where g,*l*, and *s* represent the gas, liquid, and solid phases, respectively. This equation also allows us to make some simple observations to understand typical wetting behavior. If $\gamma_{vs} > \gamma_{ls} + \gamma_{vl}\cos(0\text{ deg})$, the liquid will be perfectly wetting and spontaneously spread on the surface with a contact angle of 0 degrees. Alternatively, if $\gamma_{vs} > \gamma_{ls} + \gamma_{vl}\cos(180\text{ deg})$, then the liquid will be perfectly non-wetting. For surface tensions in between these extreme scenarios, a contact angle between 0 and 180 degrees is observed, where $\theta < 90$ degrees is termed philic, and $\theta > 90$ degrees is termed phobic, i.e, hydrophilic or hydrophobic in the case of water. Generally speaking, a surface with a large gas-solid surface tension will be more philic than a surface with a lower gas-solid surface tension.

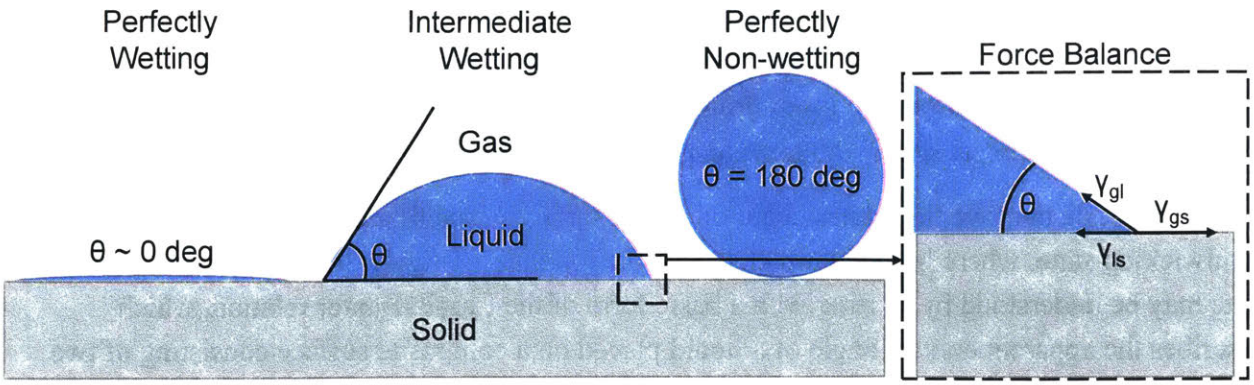

Figure 1: Contact angle on a flat surface (Young's angle).

Liquid on a homogeneous flat surface forms a contact angle dependent on the surface tension of the different liquid, solid, and gas interfaces. A simple force balance at the three-phase contact line can be used to determine the contact angle, or Young's angle, the liquid assumes, which can range from perfectly wetting (θ = 0 deg) to perfectly non-wetting (θ = 180 deg).

1.2.2 Rough Surface Wetting Behavior

When a flat surface is roughened, the macroscopic liquid behavior of a droplet on the surface is an enhanced version of the behavior on a flat surface[1]. A liquid that naturally wets a surface (Young's angle on a smooth surface, θ, less than 90 degrees) typically becomes more wetting with surface roughening such that the apparent contact angle of liquid on the surface, θ^*, is less than θ (Figure 2a). In contrast, a liquid that is non-wetting on a surface ($\theta > 90$ degrees) becomes more non-wetting with surface roughening such that θ^* is greater than θ (Figure 2b).

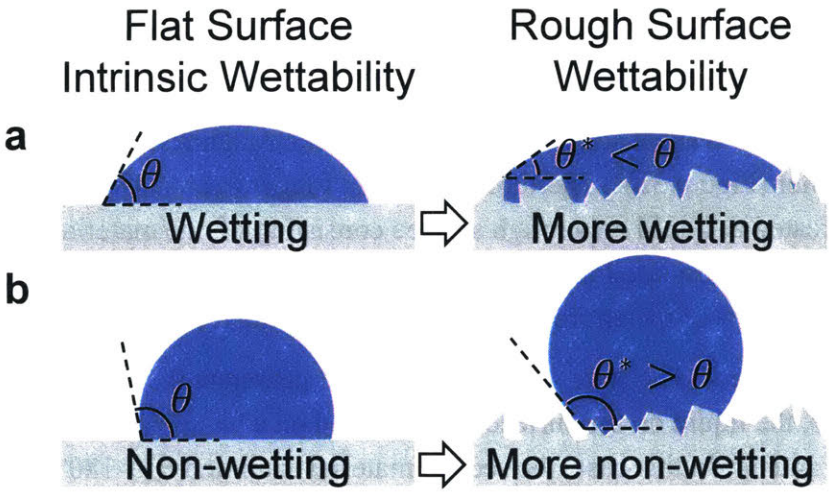

Figure 2: Roughness enhances intrinsic wettability.

***a**, When a surface that is wetting to a given liquid is roughened, it becomes more wetting such that the apparent contact angle, θ^*, is less than the intrinsic contact angle, θ. **b**, Likewise, when a surface that is non-wetting to a given liquid is roughened it becomes more non-wetting such that the apparent contact angle, θ^*, is greater than the intrinsic contact angle, θ.*

Three distinct wetting states occur on rough surfaces. The first is the highly wetting hemiwicking state, where liquid completely fills the roughness (Figure 3a). The behavior in this state may be understood by starting with a basic form of the Cassie-Baxter relation, which describes the apparent contact angle of a liquid placed on a composite surface consisting of two distinct materials[2]

$$\cos\theta^* = f_1\cos\theta_1 + f_2\cos\theta_2 \tag{2}$$

where f_1 and f_2 are the areal fractions of the two different materials that constitute the wetted surface. θ_1 and θ_2 are the intrinsic contact angles of liquid on those materials, respectively. For a flat surface consisting of two distinct materials, $f_1 + f_2 = 1$. However, if the material is roughened, $f_1 + f_2 = r$, where r is the roughness factor of the surface, i.e., the ratio of total surface area including the roughness to that of the projected area. Each of the distinct mateirals may also have their own roughness, r_1 and r2. When liquid is placed on a surface that exhibits hemiwicking, any liquid that does not wick into the roughness sits on a composite interface consisting of a solid-liquid interface and a liquid-liquid interface, where the liquid within the roughness is treated as material 2 in Eq. 2. In this scenario, because material 2 is the liquid itself, $\theta_2 = 0$ degrees, and Eq. 2 reduces to:

$$\cos\theta^* = f_1\cos\theta_1 + f_2 \tag{3}$$

For the hemiwicking case, f_1 then becomes the roughness and solid fraction of the reentrant feature only, $r_1\phi$, and $f_2 = (1 - \phi)$.

Second is the Wenzel state, where liquid fills the roughness below the droplet but does not spread further (Figure 3b)[3]. Therefore, this is no longer treated as a composite interface. Instead, it is treated as liquid on a rough surface consisting of one material where $f_2 = 0$ and $f_1 = r$. Note that the roughness used for the Wenzel state is different than that for Eq. 2 and Eq. 4 in that it is the roughness of the entire surface and not only the reentrant feature.

Finally, in the Cassie state, the liquid does not penetrate the surface roughness (Figure 3c)[4]. Therefore, the liquid on the surface is suspended on a composite interface consisting of the solid material and air. In this case, the second material is air and $\theta_2 = 180°$. Eq. 2 reduces to:

$$\cos\theta^* = f_1\cos\theta_1 - f_2 \tag{4}$$

Once again, f_1 then becomes the roughness and solid fraction of the reentrant feature, $r_1\phi$, and $f_2 = (1 - \phi)$.

Furthermore, based on surface energy and the geometry of the roughness, one can predict critical intrinsic contact angles at which each of these states is expected to occur[1]. When $\cos\theta > (1 - \phi)/(r - \phi)$, the hemiwicking state is expected[5]. Because the right-hand side of this inequality is always positive, the hemiwicking state is only expected for wetting liquids. Meanwhile, when $\cos\theta < -(1 - \phi)/(r - \phi)$, the Cassie state is favorable. Therefore, the Cassie state is only expected for non-wetting liquids. At intermediate contact angles, the Wenzel state is expected.

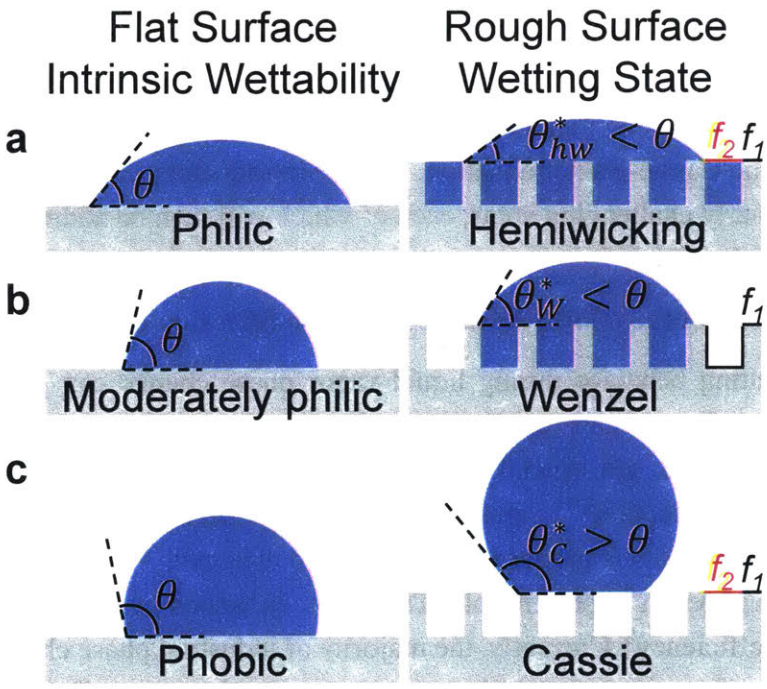

Figure 3: Wetting states on rough surfaces.

***a**, Liquid that is highly wetting on a flat surface spreads completely and fills a rough surface, reducing the apparent contact angle. This state is known as the hemiwicking state due to its similarity to wicking in porous media. The areal fractions of the composite interfaces, f_1 and f_2, are depicted by the black and red solid lines, respectively, for all states. **b**, When a moderately wetting liquid is placed on a rough surface, the liquid enters the surface roughness below the droplet but does not spread through the roughness beyond the droplet. This state is known as the Wenzel state. This state is not treated as a composite interface. As such $f_2 = 0$ and $f_1 = r$. **c**, When*

a non-wetting liquid is placed on a rough surface, the droplet is suspended on top of the structure. This state is known as the Cassie state.

1.3 Challenges in Tailoring Wetting Behavior at Extremes

Many works have been dedicated to understanding classical wetting behavior and achieving different wetting states. However, many significant challenges remain, particularly when tailoring wetting behavior at different extremes. As seen in Eq. 1, the Young's angle of the surface is solely determined by the chemical nature of the liquid and surface. Therefore, challenges often revolve around the necessity to control the chemical nature of the surface, i.e., choose specific materials or liquids. Therefore, to achieve specific wetting behavior, sacrifices are often made in other aspects such as surface durability, or certain wetting behaviors cannot be achieved at all. In other cases, although Eq. 2 - 4 generally describe the macroscopic behavior of a liquid on a surface, further thought must be given into the design of the surface structures to both ensure the surface can be fabricated, as well as to optimize liquid dynamics and kinetics that are not captured by the Cassie-Baxter equation. Further introductory details are given here in each of these particularly challenging areas, each of which will then be addressed within this thesis with a dedicated chapter.

1.3.1 Robustness of Coatings for Surface Energy Modification during Heat Transfer

Tailoring wetting behavior during liquid-vapor phase change can greatly enhance heat transfer performance for various applications. Evaporation and condensation, phenomena commonly found in nature, are crucial components in industrial applications such as power generation[6-8], water purification[9-11], and thermal management[12,13]. In fact, the majority of electricity in the United States is produced using steam power cycles, in which condensation and evaporation of water plays an important role. Therefore, enhanced heat transfer performance can directly affect cycle efficiency[8]. Currently, the majority of industrial phase change processes don't utilize modification of surface wettability to enhance performance. For example, industrial condensers used for power generation use metals that are highly wetting to water. This leads to filmwise condensation, where the condensate wets the surface of condenser and forms a thick liquid film, impeding heat transfer. However, by utilizing low-surface-energy coatings on condenser surfaces to render the surface hydrophobic, enhanced condensation heat transfer can be achieved in the so-called dropwise condensation mode, causing condensate to form discrete droplets that nucleate, grow, coalesce, and easily shed[14]. In dropwise condensation, because condensate is removed from the surface more efficiently, heat and mass transfer performance can be improved by an order of magnitude. Similarly, heat transfer performance during boiling can be significantly enhanced by controlling wetting behavior, where hydrophobic coatings promote nucleation of vapor bubbles[15]. However, despite the fact that low-surface-energy coatings for heat

transfer enhancement have been explored for close to a century[16-18], industry continues to rely on systems without modified wetting behavior. This is due primarily to a lack of durability of developed coatings. Past work has focused on developing numerous low-surface-energy coatings, including monolayer promoters[19-23], organic films[24-28], lubricant infused surfaces (LIS)[29-32], and graphene[33]. Recent work has also focused on combining these coatings with surface structuring to further enhance hydrophobicity[34-38]. However, robust coatings have not been demonstrated while still achieving significant performance enhancement (Figure 4). Instead, adequate lifetimes of organic coatings (years) were only achieved when the coating thickness was large (>4 μm). Due to the low thermal conductivity of the coatings, the added thermal resistance of the coating at this thickness was large enough to significantly reduce the performance enhancement. Thinner coatings of various types, which achieved significant performance enhancement, failed quickly. Therefore, more practical forms of enhancement have focused on increasing heat transfer area through use of fins and extended surfaces[39,40]. However, overall heat transfer enhancement was not as significant as strategies that alter surface wettability.

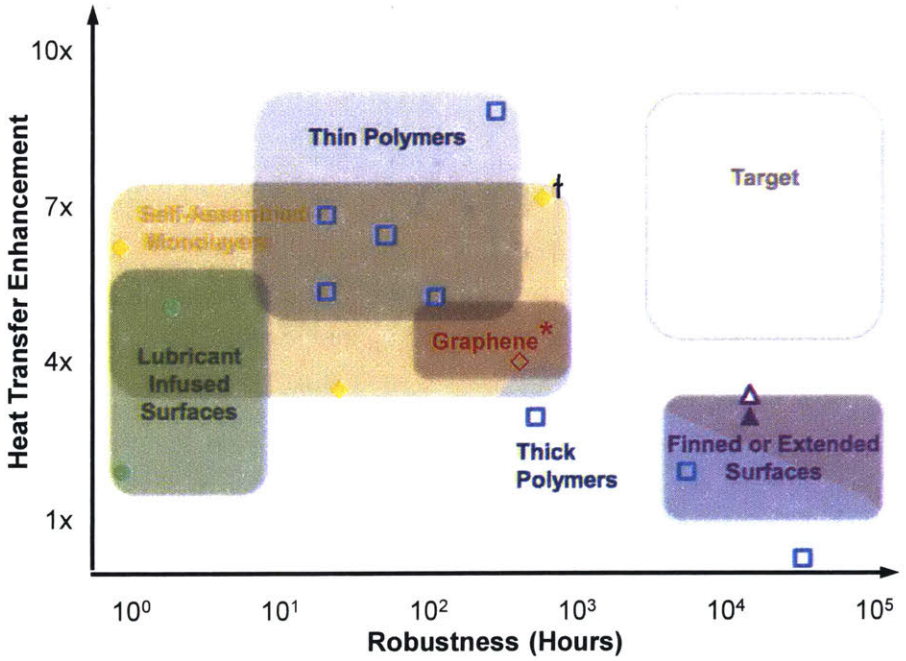

Figure 4: Robustness and heat transfer enhancement of hydrophobic coatings.

Heat transfer enhancement of various hydrophobic surface coatings, including lubricant infused surfaces, monolayer promoters, polymers, graphene, and finned surfaces, and observed robustness (lifetime). Coatings that achieve large improvements in performance are thin, which

limits the heat transfer resistance through the coating, but also causes the coatings to fail quickly. Similarly, thick, robust coatings have minimal performance enhancement.

1.3.2 Shifting the Wetting Paradigm: Reentrance for Omniphobicity

Surfaces that exhibit extreme liquid wetting behavior, ranging from wicking to repelling, have broad applications for various high-performance systems. Roughening of a smooth surface enables these extreme wetting behaviors to be achieved. At one extreme, this enables a surface to wick liquid, which is desired for microfluidics[41], anti-fogging[42], and heat transfer enhancement via boiling and thin film evaporation[43,44]. At the other extreme, a liquid contacting the surface is suspended on the roughness, beads, and is thus repelled and shed[45], which is needed for anti-fouling[46,47], water purification[48], heat transfer enhancement[34,49], drag reduction[50], and self-cleaning surfaces[51]. However, because roughening tends only to enhance the intrinsic wetting behavior, chemical modification of the surface is necessary for control of θ in order to achieve wicking or repellency. Although this control of θ is well-developed for a liquid like water, it is difficult to achieve $\theta > 90°$ for a low-surface-energy liquid such as a fluorinated solvent[52] as well as $\theta < 90°$ for a high-surface-energy liquid such as a liquid metal[53]. Therefore, this approach requires selection of specific surface materials for desired behavior, cannot be applied to all liquids and applications, and is sensitive to changes in surface chemistry such as degradation or contamination[14,54]. Furthermore, this approach cannot enable surfaces that can easily switch between repelling and wicking[55] and requires complex chemical coatings for surfaces to selectively wick certain liquids while repel others[56]. Such wetting behaviors are highly desirable for liquid separation[57,58], microfluidics[59], and microrobotics[60]. Accordingly, all of these wetting behaviors remain very challenging and often unutilized despite the broad impact they would have.

In order to shift the paradigm that surface roughness only enhances intrinsic wettability and rather render a surface repellent to wetting liquids as well, surfaces with specific reentrant and doubly reentrant microstructures have been used[52,61,62]. Reentrant structures achieve fluid repellency by trapping air underneath liquid on the surface via specific "reentrant" microstructures that prevent liquid from entering the roughness. The geometry takes advantage of the surface tension of the fluid to create a local energy barrier for fluid propagation which keeps liquid from entering the microstructure. Depending on the level of reentrance of the geometry, α, the surface is able to repel fluids with different contact angles, θ (depicted in Figure 5a). The black arrow in the schematics represents the direction of the surface tension force that prevents liquid from entering the structure. For a normal microstructure ($\alpha \leq 0°$), the surface tension force only acts to prevent liquid entering the microstructure if $\theta > 90 - \alpha$. As the level of reentrance increases, the surface is able to repel liquids with lower contact angles. A reentrant

microstructure ($0° < \alpha \leq 90°$) can repel liquids with a contact angle less than 90°. However, for perfectly wetting fluids with $\theta = 0°$, the surface tension force would no longer have a component in the vertical direction. Therefore, to be omniphobic and repel all fluids, including perfectly wetting fluids, a doubly reentrant microstructure is needed[52]. Therefore, repellency has been achieved independent of surface chemistry, but similar success had not yet been achieved for other desired wetting behaviors such as wicking, selective surfaces, or switchable surfaces despite its potential to benefit a wide range of technical applications.

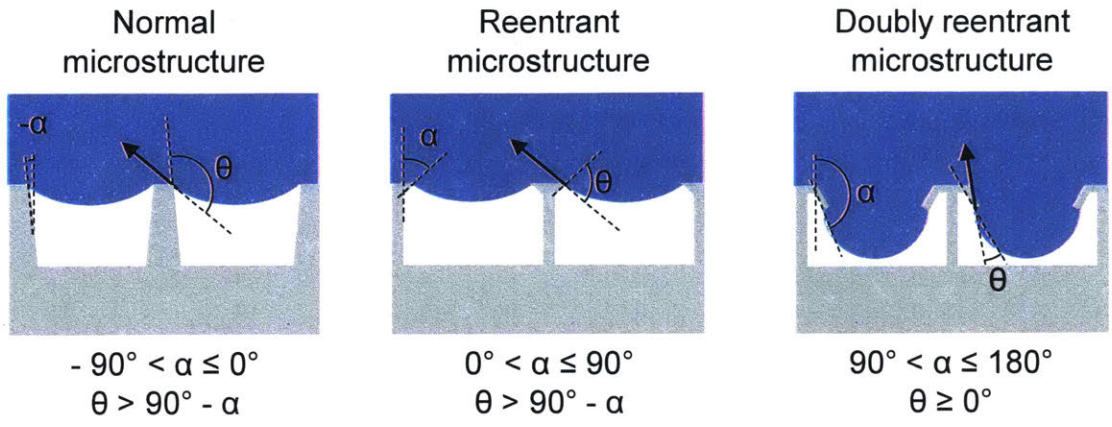

Figure 5: Reentrant microstructures enable omniphobic and omniphilic behavior.

Normal microstructures only repel liquids that are non-wetting ($\theta > 90°$). In order to repel all liquids, i.e., omniphobic, reentrant and doubly reentrant structures are required.

Furthermore, despite the fact that reentrant surfaces enable amazing wetting behavior, a number of significant challenges prevent their widespread use. First, reentrant geometry achieve repellency by creating a metastable Cassie state, but the global energy minimum for the surface is often a Wenzel or hemiwicking state. This metastability causes reentrant surfaces to be highly susceptible to defects or other forms of failure that destroy their omniphobicity. Further work needs to explore methods to improve the stability of these surfaces. Finally, because reentrant surfaces require specific, and complex, geometry to achieve omniphobicity, fabrication is challenging.

1.3.3 Wicking Dynamics: Optimizing Structured Surfaces

The highly wetting hemiwicking state, in which liquid is spontaneously drawn into the surface structuring via capillary pressure (the pressure generated by a curved liquid-gas interface), has broad applications in microfluidics[63] such as in lab-on-a-chip[64], electro-chromatography[65], resin molding[66], biomedical devices[67], and thermal management[68-70]. In particular, wicking in micro/nano scale wicks has emerged as a promising method to enhance thermal management

techniques such as thin film evaporation[43,71-73], pool boiling[74,75], and flow boiling[76-78]. In these thermal management schemes, cooling is achieved via liquid-vapor phase change which takes advantage of the large latent heat of evaporation. Once liquid to be evaporated can no longer be adequately supplied the cooling scheme fails, which happens at the dry-out heat flux in thin film evaporation or the critical heat flux (CHF) in boiling. To prevent dry-out and CHF, micro/nanostructures have been introduced to the surface. Wicking due to the capillary pressure produced by the surface structuring provides passive supply of liquid to be evaporated, as seen in Figure 6a for thin film evaporation. How well the surface wicks liquid has been shown to determine the heat transfer enhancement for both thin film evaporation and boiling[43,72,75,79]. Therefore, a variety of wicks have been tested, with features ranging from nanoscale to microscale and with different feature shapes and designs[80,81].

A commonly used wicking structure is a micropillar array due both to the ability to model flow in the well-defined structure and the effectiveness of the design for wicking. Previous studies have typically modelled flow in a pillar array using either the Brinkman equation or Darcy's law, treating the array as an isotropic porous medium [82-87]. The permeability of a quadratic pillar array, for example, needed to use the Brinkman equation or Darcy's law has also been determined computationally and confirmed experimentally [84,88]. More detailed numerical models to accurately capture wicking in pillar arrays accounting for such effects as meniscus curvature have also been developed [43]. In all of these studies, the pillar arrays used have been uniform (i.e., same pillar pitch (l), diameter (d), and height (h) everywhere in the array). In a uniform array, the competing effects of capillary pressure and viscous resistance give rise to an optimum pillar pitch and diameter (for a given pillar height) to maximize the ability of the surface to wick fluid [83]. The liquid pressure along the wicking direction (generated via capillarity) for one such array (h = 25 μm), calculated using the model described in chapter 6 of this thesis, is shown in Figure 6b. As the heat flux, q'', increases the pressure drop also increases. Eventually, the pressure drop becomes large enough that the maximum possible capillary pressure sustainable by the wick is reached and dry-out occurs at q'' = 61 W/cm^2. However, the maximum capillary pressure is only reached at the end of the structured surface (x = 5mm). Therefore, due to the coupling between capillary pressure and viscous resistance, locations on the wick that are not near the maximum capillary pressure could be designed to have enhanced permeability to reduce pressure drop, i.e., wick geometry is varied along the wick length, improving wicking performance, benefiting a range of applications.

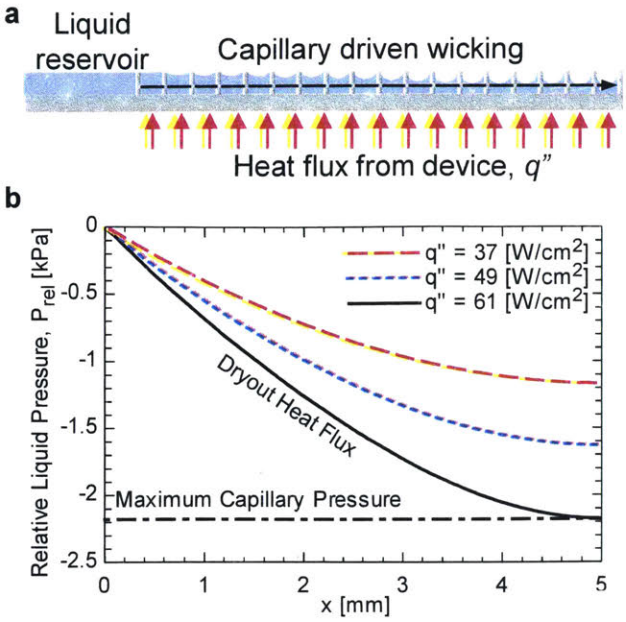

Figure 6: Wicking in uniform pillar arrays.

a*, Schematic of thermal management based on thin film evaporation from structured surfaces. Fluid for evaporation is supplied passively via capillary driven wicking in the structured surface.* ***b****, Relative liquid pressure at different applied heat fluxes along an optimized 5 mm wicking length for a uniform square pillar array with pillar height, pitch, and diameter of 25 μm, 30 μm, and 10 μm, respectively. At a heat flux of 61 W/cm^2, the maximum possible capillary pressure sustainable by the surface is reached and dry-out occurs.*

1.4 Thesis Objective and Outline

This thesis explores methods to tailor wetting behavior in these challenging scenarios by understanding the limitations of tailoring wetting behavior with the classical approach, and rationally designing surfaces that overcome these limitations.

In Chapter 1, the motivation for studying and tailoring wetting behavior was discussed. Significant challenges in the field were explained.

In Chapter 2, we address the durability of hydrophobic coatings in heat transfer applications. Specifically, polymer infused porous surfaces were designed and demonstrated for stable promotion of dropwise condensation for 200+ days.

In Chapter 3, reentrant surfaces are used to shift the classical wetting paradigm. Specifically, we demonstrated that reentrant microstructures enable any wetting behavior to be achieved independent of surface chemistry. We showed a surface design that can be omniphobic

(repel all liquids), omniphilic (wick all liquids), switchable between omniphobicity and omniphilicity, and selective (repel and wick only certain liquids). Applications of this type of surface are also discussed.

In Chapter 4, we address robustness issues with using reentrant surfaces to tailor wetting behavior. Specifically, reentrant surfaces lose their omniphobicity during condensation. We designed and demonstrated a reentrant surface that maintained it's repellency during condensation, and was also robust to other forms of failure common to omniphobic reentrant surfaces.

In Chapter 5, we address the challenging fabrication of doubly reentrant, omniphobic surfaces. Specifically, we leveraged intrinsic stressed in films of silicon nitride to create doubly reentrant surfaces via stress induced bending. This enabled the use of standard microfabrication processes to achieve omniphobicity.

In Chapter 6, we improve wicking performance by 300%. Specifically, we designed nonuniform surfaces where the wick geometry changed along the wicking direction. This enabled the permeability at each location to be optimized, improving overall performance significantly.

In Chapter 7, perspectives on the work are presented.

2. Robust, Repairable, High Thermal Conductance Hydrophobic Coatings

Hydrophobic coatings with high thermal conductance have been explored for nearly a century due to the significant enhancement to performance they promise in systems such as the condensers and boilers in power plants. However, coatings with adequate robustness have remained elusive due to a combination of the lack of proper adhesion to substrates and the typically low thermal conductivity of hydrophobic materials necessitating very-thin coatings to achieve high thermal conductance. In this work, we simultaneously address both of these issues by infusing hydrophobic polymers into nanostructured surfaces. The nanostructures in this polymer infused porous surface (PIPS) provide 1. large surface area for adhesion and physically constrains the hydrophobic polymer to the surface and 2. form a percolated network of high thermal conductivity material throughout the polymer, greatly enhancing the thermal conductivity of the composite material. We demonstrate that these surfaces are durable in extreme environments, where enhanced condensation of steam at conditions typical in power plants was achieved for more than 200 days without any degradation. Furthermore, we show the surfaces are corrosion resistant and also self-repairing to damage simply by raising the temperature to the polymers melting point, which allows the polymer to reflow and repair local damage.

2.1 Introduction

Tailoring wetting behavior during liquid-vapor phase change can greatly enhance heat transfer performance for various applications. Evaporation and condensation, phenomena commonly found in nature, are crucial components in industrial applications such as power generation[6-8], water purification[9-11], and thermal management[12,13]. In fact, the majority of electricity in the United States is produced using steam power cycles, in which condensation and evaporation of water plays an important role. Therefore, enhanced heat transfer performance can directly affect cycle efficiency[8]. An effective method for enhancing heat transfer performance during phase change is to tailor the wettability of the surface. For example, dropwise condensation, enabled by hydrophobic low-surface-energy coatings, has heat transfer performance approximately one order of magnitude better than the filmwise mode of condensation prevalent in industry[14]. For this reason, nearly a century of work has been conducted on developing coatings (Figure 7, which shows coating development for condensation heat transfer enhancement)[17-19,24,25,28,33,34,89-93].

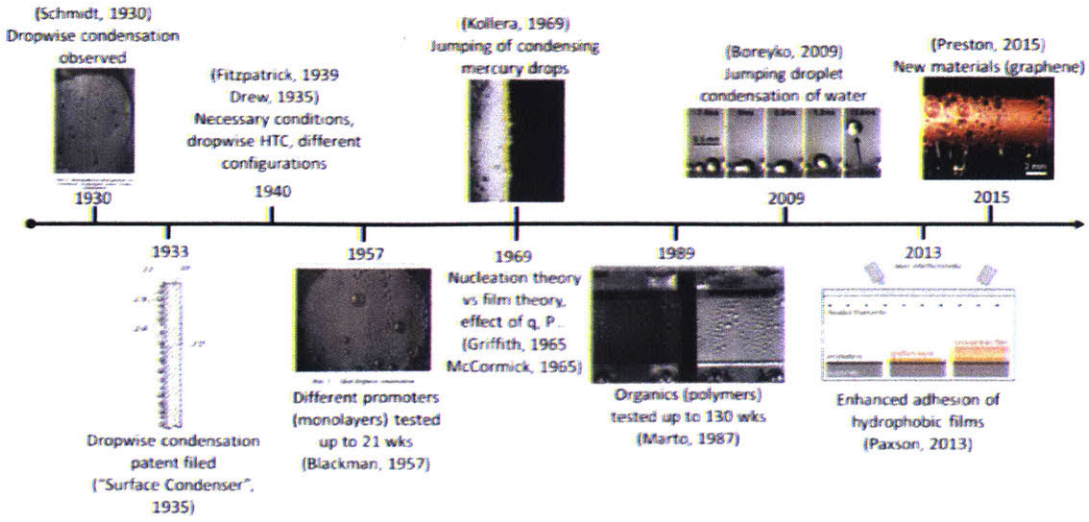

Figure 7: History of the development of coatings for enhanced condensation heat transfer.

However, industrial applications have not taken advantage of these coatings due to challenges developing a coating that can enhance heat transfer performance while also being robust enough to have an adequate lifetime (Figure 4). Generally speaking, this problem arises because the types of materials that enable dropwise condensation, such as low-surface-energy polymers, have low thermal conductivity and poor adhesion to surfaces. Therefore, coatings must be thin, and, as a result, have poor lifetime. In Figure 8, dropwise condensation at 60 ° C on copper surfaces coated with Teflon AF is shown over time. Thickness and adhesion were varied. Lifetime of the coating was increased both with increasing thickness and increasing adhesion (adhesion is best on a silane modified copper surface, and worst on copper oxide[94]); however, lifetime was only a matter of hours or days whereas industrial applications require a lifetime of years, highlighting the severe durability issues coatings have.

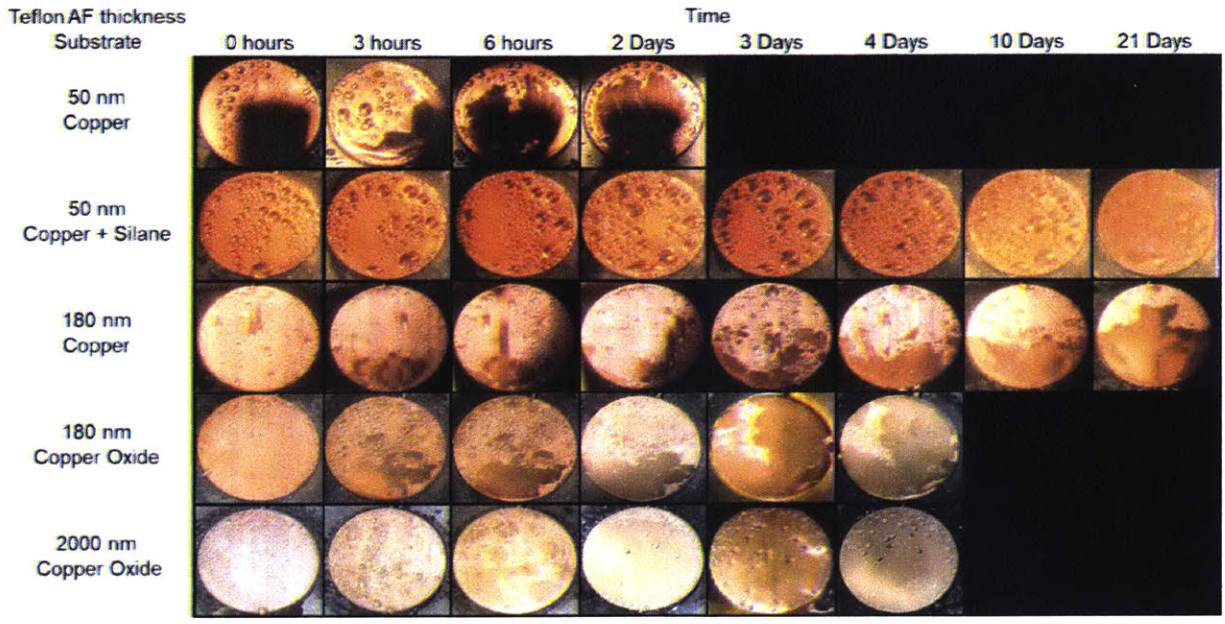

Figure 8: Poor Robustness of Thin Polymer Coatings.

Images of dropwise condensation on copper coated with Teflon AF with various thicknesses and adhesion. Adhesion is worst on copper oxide and best on a copper modified with a silane. Improving adhesion increases lifetime. Increasing thickness also improves lifetime. However, coatings still fail too quickly for use in most practical applications.

Herein, we demonstrate an approach to address both the low thermal conductivity and poor robustness of hydrophobic coatings simultaneously. A hydrophobic polymer (Teflon AF) was infused into nanostructures grown directly on condenser surfaces. The nanostructures create large surface area for adhesion and constrain the polymer on the surface. Furthermore, because the nanostructures create a percolated network of high thermal conductivity material through the low thermal conductivity polymer, the thermal conductance of the coating is greatly increased. We discuss the design and fabrication of these polymer infused porous surfaces (PIPS), and demonstrate dropwise condensation for more than 200 days without any sign of degradation. We also show that coatings of this type are self-healing simply by raising the temperature of the surface above the polymers melting point.

2.2 Design of Polymer Infused Porous Surfaces

To achieve condensation heat transfer enhancement through dropwise condensation with low-surface-energy coatings, multiple design criteria for the proposed polymer infused porous surfaces must be considered (Figure 9a). The first is that the coating must not add significant resistance to heat transfer, i.e., the thermal conductance must be high. Thermal conductance scales as k/H, where k and H are the thermal conductivity and the thickness of the coating, respectively.

Historically, because low-surface-energy coatings tend to have low thermal conductivity, this has been achieved by using very thin coatings (H < 4 μm). At these small thicknesses, adhesion of polymers is poor, resulting in inadequate robustness. Therefore, improving adhesion of the coating, as well as improving thermal conductivity such that thicker coatings may be used would both benefit coating lifetime. Second is the ability of the low-surface-energy coating to enable dropwise condensation, for which the wetting behavior on the surface is important. Generally, the quality and performance of dropwise condensation is greatest when the advancing contact angle, θ_a, is large ($\theta_a > 90$ degrees) and the contact angle hysteresis, i.e., the difference between the advancing contact angle and the receding contact angle, is small ($\theta_a - \theta_r < 15$ degrees)[95].

To enhance adhesion of polymers to a surface, surfaces are often roughened, increasing the total surface area the polymer is in contact with[96]. In the case of pillars, the surface area enhancement is

$$\text{Surface Area Enhancement} = \frac{L^2 + \pi DH}{L^2} \tag{5}$$

where L is the pitch and D is the diameter of the pillar. The surface area enhancement is shown in Figure 9b for different solid fractions, ϕ (for pillars $\phi = (\pi D^2/4)/L^2$), and a height of 10 μm. H = 10 μm was chosen as a representative case given thickness should remain relatively small to limit the thermal resistance the coating adds. The surface area enhancement in this scenario is maximized by moving to smaller pitch, i.e., tall slender structures, where significant enhancement is only reached when structure pitch is hundreds of nanometers.

The PIPS form a composite material consisting of low thermal conductivity polymer and a higher thermal conductivity nanostructure and a surface composed of highly wetting nanostructure and hydrophobic polymer. Therefore, the nanostructure exposed at the surface will affect the wettability of the surface, which would affect the quality of the dropwise condensation. Previous works have developed expressions for the expected advancing and receding contact angles[97]

$$\cos\theta_a = \cos\theta_{polymer} \tag{6}$$

$$\cos\theta_r = \sqrt{1-\phi(x=0)}\cos\theta_{polymer} + \left(1-\sqrt{1-\phi(x=0)}\right)\cos\theta_{ns} \tag{7}$$

where $\phi(x=0)$ is the solid fraction of the nanostructure at the surface exposed to the liquid. In order to minimize contact angle hysteresis, solid fraction at the surface should remain small (Figure 9c). We note that there is also the possibility to overfill the nanostructure, thereby creating a polymer only surface. However, because the overfilled polymer would have low thermal conductivity, it would create significant resistance to heat transfer and should be kept thin. Therefore, in this work, we avoid overfilling and instead design the surface to function properly assuming the nanostructures are partially exposed to the liquid.

The network of nanostructure inside the polymer enhances the thermal conductivity. In fact, because the nanostructure is grown on the surface, it inherently creates a continuous, percolated network of high thermal conductivity material through the entire thickness of the layer, forming parallel heat transfer paths. In this scenario, the effective thermal conductivity, k_{eff}, of the layer can be estimated as[98-100]

$$k_{eff}(x) = \phi(x)k_{ns} + \big(1 - \phi(x)\big)k_{polymer} \tag{8}$$

where k_{ns} and $k_{polymer}$ are the thermal conductivities of the nanostructure and polymer, respectively. Here, the effective thermal conductivity and solid fraction are shown as a function of x (see Figure 9a). Although pillars have a constant solid fraction in x, many types of nanostructures do not, which should be considered when considering the enhancement of the overall thermal conductivity. From Eq. 8 over the entire thickness of the PIPS to determine the effective thermal conductivity of the layer. In Figure 9c, we consider nanostructures with constant solid fraction throughout the layer thickness made of copper (k_{ns} = *376* W/mK). Effective thermal conductivity can be enhanced orders of magnitude over that of the polymer ($k_{polymer}$ = *0.29* W/mK) even with relatively small solid fractions of nanostructure.

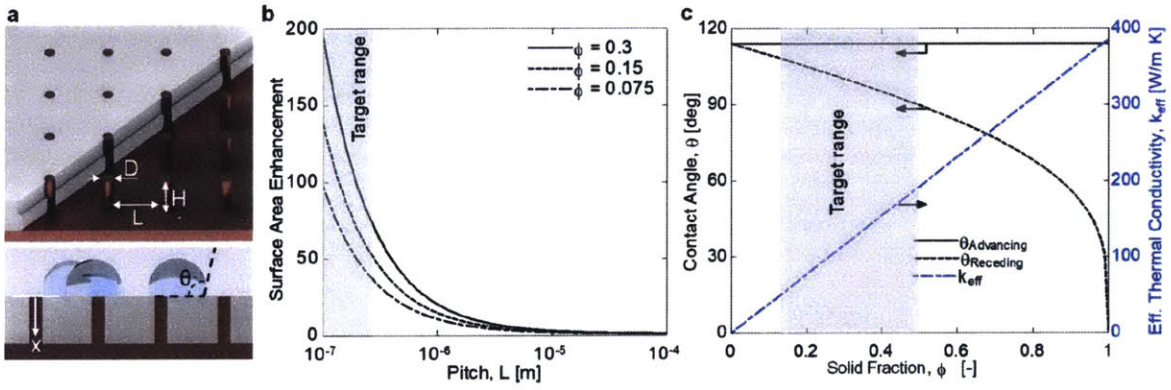

Figure 9: Design of PIPS.

***a**, Schematic of polymer infused porous surfaces. Structured surfaces (depicted with pillars in the schematic) are infused with polymer (white material in schematic). A portion of the polymer was removed in the schematic to reveal the structured surface with characteristic dimensions height, H, diameter, D, and pitch, L. **b**, Surface area enhancement for a surface with pillars and H = 10 μm as structure pitch is varied. **c**, Effective thermal conductivity of the coating (dashed blue line) as well as predicted advancing and receding contact angles (black lines) of the surface.*

However, given many nanostructures do not form a constant solid fraction, we consider the effect of varied solid fraction throughout the coating. We considered three scenarios, constant, linear, and parabolic solid fractions throughout the layer (Figure 10), where $k_{eff}(x)$ is shown along x. The resulting effective conductivity of the entire coating, i.e., the effective conductivity if the coating was treated as a homogeneous medium, is labeled for these scenarios. All types of nanostructure greatly enhanced the thermal conductivity over the polymer; however, constant solid fraction is most effective, followed by linear, and then parabolic. Parabolic performs the worst due to the small amount of nanostructure near the surface of the layer, resulting in a low effective thermal conductivity.

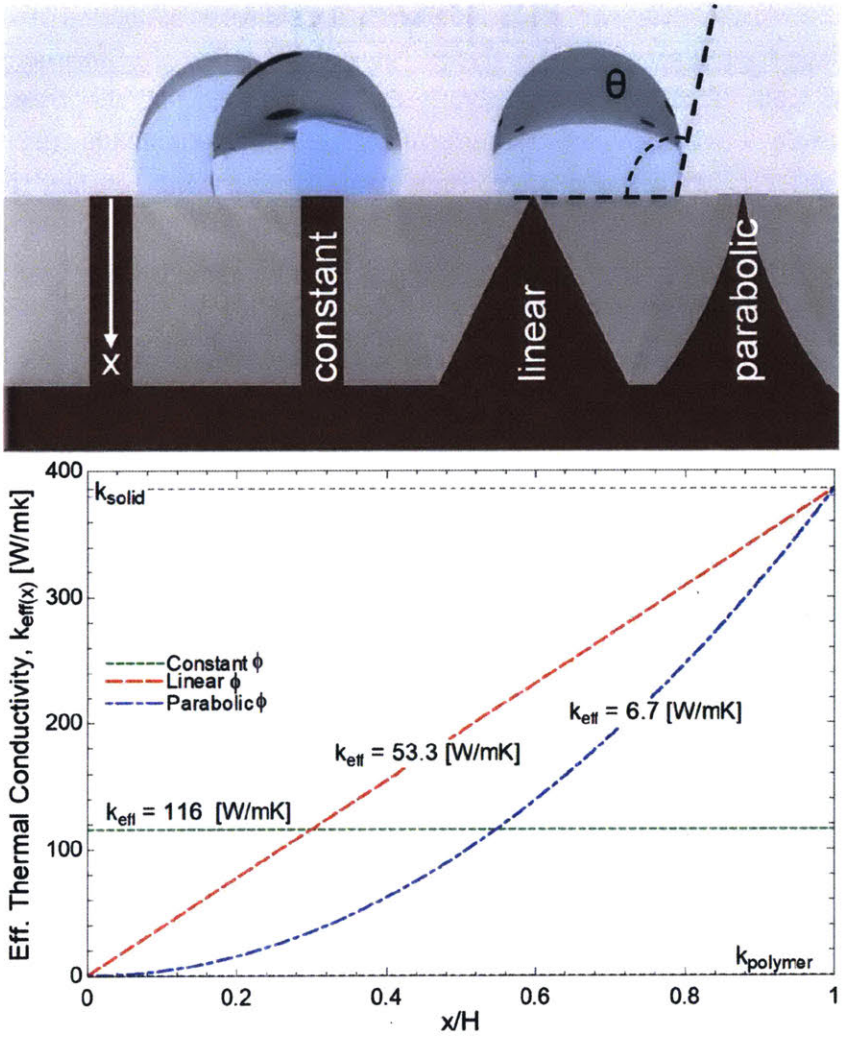

Figure 10: Effect of Variable Solid Fraction on Effective Thermal Conductivity

Three cases for variable solid fraction along x are considered. Constant solid fraction, such as pillars, linear solid fraction, such as triangular ridges, and parabolic solid fraction, such as nanocones. For simplicity, the linear and parabolic cases are assumed to go from $\boldsymbol{\phi = 0}$ *at* $\boldsymbol{x = 0}$ *to* $\boldsymbol{\phi = 1}$ *at* $\boldsymbol{x = H}$*, whereas the constant solid fraction in this figure is 0.3. The resulting* $\boldsymbol{k_{eff}(x)}$ *is shown, and the resulting overall* $\boldsymbol{k_{eff}}$*, i.e., the effective thermal conductivity of the layer assuming it were homogeneous, is calculated and labeled in the figure.*

Based on calculated effective thermal conductivities, we define a critical thickness, H_{crit}, beyond which the coating would degrade dropwise heat transfer performance by 10 percent or more. This critical thickness was estimated using a thermal resistance network

$$\frac{1.1}{h_{cond}} = \frac{1}{h_{cond}} + \frac{H_{crit}}{k_{eff}} \tag{9}$$

where h_{cond} is the heat transfer coefficient of dropwise condensation. We take a conservative value of 100 kW/m^{2}K. The resulting critical thicknesses, along with expected contact angle hysteresis are shown in Table 1 for different nanostructure solid fractions and materials.

Table 1: Critical thickness and expected contact angle hysteresis.

Different possible nanostructure type, materials, and designs are considered. The resulting critical thickness, surface solid fraction, and expected advancing and receding contact angles are shown. Highlighted in blue are designs that were chosen for this study.

Nanostructure Type	Material	H_{crit} [μm]	$\phi(x = 0)$	θ_a [deg]	θ_r [deg]
None (Teflon AF)	-	0.29	0	114	114
Parabolic	Copper	6.6	0	114	114
Linear	Copper	52	0	114	114
Constant	Copper	56.6	0.15	114	107.3
Constant	Copper	188.1	0.5	114	89.7
Parabolic	Copper Oxide	1.53	0	114	114
Constant	Copper Oxide	3.2	0.15	114	107.3

2.3 Fabrication of Polymer Infused Porous Surfaces

Based on the design consideration above, nanostructures were chosen that could be controlled within the blue highlighted rows of Table 1. Specifically, we chose copper oxide nanoblades and copper nanowires (Figure 11a) for the nanostructure due to the ability to grow them directly on the surfaces with dimensions in the required range[38,101]. These nanostructures were first grown on the condenser surface, and then infused with polymer until the entire nanostructure was filled (Figure 11b). Care was taken not to overfill the nanostructures, given

overfilling would create a layer of low-thermal-conductivity polymer on top of the nanostructures, creating additional resistance to heat transfer. As seen in Table 1, overfilling of only 290 nm would decrease performance by roughly 10 percent. The polymer Teflon AF 1600 was chosen due to its hydrophobicity and the ease of filling of the nanostructure. By spin coating consecutive layers of Teflon AF, the filling was precisely controlled and stopped before overfilling occurred (Figure 11c). Scanning electron microscope images, and contact angle measurements were used to determine when filling was complete. After spin coating, the surface was heated above the polymers melting point to ensure proper filling of the nanostructure without voids. This resulted in a predominately Teflon AF surface with very low roughness, ideal for enabling dropwise condensation, as seen in the atomic force microscope images in Figure 11d that shows a copper oxide surface at the filling stages shown in Figure 11c.

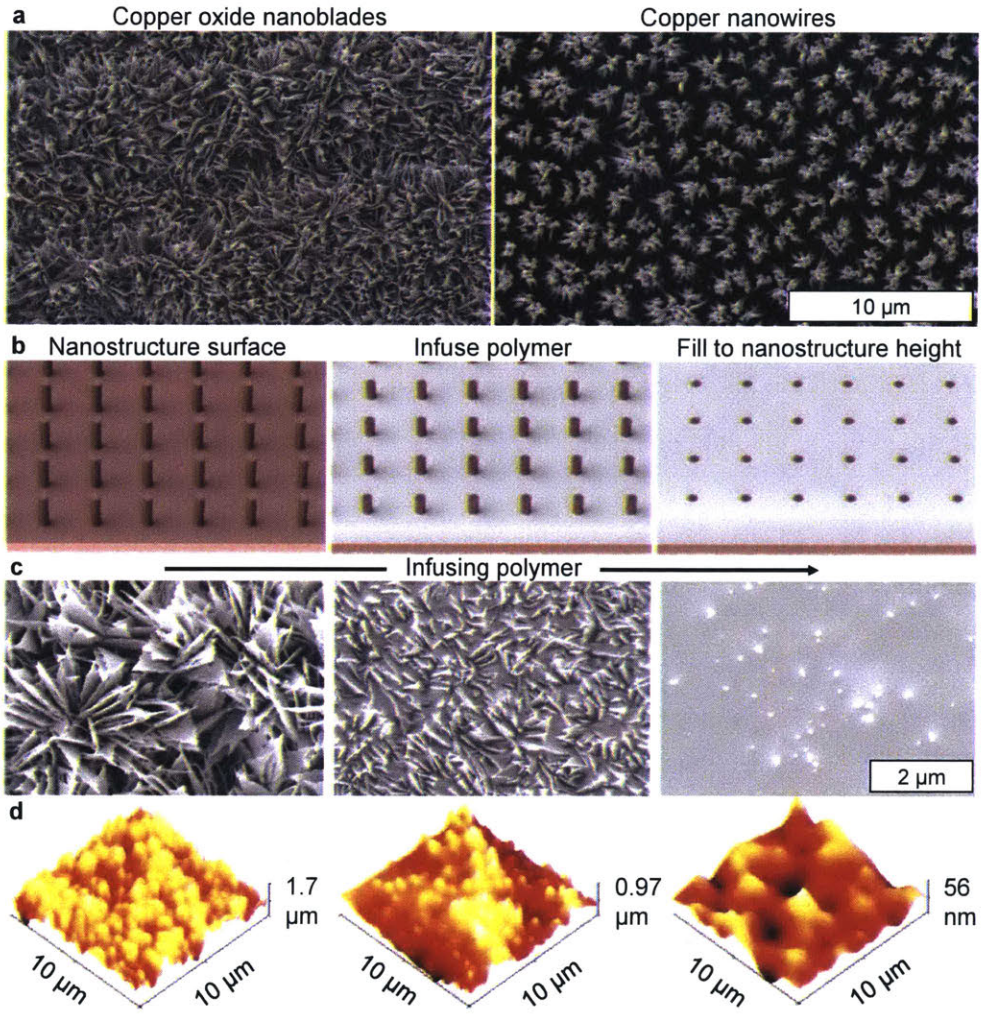

Figure 11: Fabrication of Polymer Infused Porous Surfaces

***a**, Top view scanning electron microscope images of copper oxide nanoblades and copper nanowires used in this study. **b**, Schematic of fabrication process for PIPS. First, nanostructures were grown directly on the condenser surface. Next, the polymer was infused until the nanostructure was completely filled without covering the surface with polymer to prevent additional resistance to heat transfer. **c**, Top view scanning electron microscope images of filling copper oxide nanostructures at different stages. Filling is stopped when the polymer completely fills the structure, but has not yet formed a layer on top of the nanostructure. **d**, Atomic force microscope images as the nanostructure is infused. The final surface has very small roughness, resulting in a highly smooth, hydrophobic surface.*

Table 2: Properties of fabricated surfaces.

The geometry and measured advancing and receding contact angles of all surface used in this study. These geometries were chosen to test the full range of designs that are expected to provide enhancement using standard fabrication methods. A 2 μm Teflon AF coating with no nanostructure was also fabricated as a reference.

Nanostructure	Material	H [μm]	$\phi(x=0)$	θ_a [deg]	θ_r [deg]
None	-	2	0	107.2	106
Constant	Copper	5	0.5	108	80.5
Constant	Copper	25	0.5	108.5	84.3
Parabolic	Copper Oxide	1.5	0	108.2	103.2

2.4 Testing of Polymer Infused Porous Surfaces

The resulting surfaces consisted predominately of Teflon AF. This resulted in a high quality, hydrophobic surface with large advancing contact angle and low contact angle hysteresis (Figure 12a, which shows CuO nanoblade PIPS). Furthermore, because the surface was prepared using a polymer that can melt, a simple mechanism for self-healing exists. Self-healing surfaces are generally split into two categories, autonomic, which heal automatically when damaged, and non-autonomic that require a modest external trigger, such as heat or light[102,103]. PIPS fall into the second category, where applying heat to re-melt the polymer causes it to flow across the surface, repairing local damage. In Figure 12b, a surface damaged using laser ablation is shown. The laser, which was used to create a grid of damaged lines on the surface, created roughly 100 μm wide sections, where the polymer was largely removed from the surface and the underlying nanostructure. However, by heating the surface to 330 degrees C, the polymer reflowed and largely repaired the surface, thereby recovering the original wetting properties. In Figure 12c, the

advancing and receding contact angle of the surfaces are shown. The advancing contact angle is the upper bound of the box, whereas the receding contact angle is the lower bound. The original, undamaged surface is hydrophobic with small hysteresis. The surface was then damaged different ways. Laser ablation, as see in Figure 12b, removed much of the polymer but did not completely destroy the underlying nanostructure, scraping using a multiblade cross hatch cutting tool (ISO 2409:2007) destroyed both the polymer and nanostructure, and chemical damage (achieved here by placing the surface in a plasma chamber for 3 minutes) removed fluorination (and thus hydrophobicity) at the surface of the coating but left the underlying polymer and structure undamaged[104]. After repair to all types of damage, the original contact angles were largely recovered, where the level of physical damage to the surface and nanostructure determined how well the surface could be repaired. Because chemical damage did not destroy the structure at all, the original contact angles were completely recovered, whereas with scraping, which caused significant damage to the surface, the wetting properties were only partially recovered. The recovery of surface wetting properties is demonstrated in Figure 12d, where the left images show condensation on a surface after laser ablation (top left, where the white lines are the grid of laser damage) and chemical damage (bottom left). Due to the large contact angle hysteresis, droplets on the surface grow very large and begin to spread, covering the surface. However, after repair (right images), small, highly mobile droplets are once again achieved.

Furthermore, because the PIPS are primarily non-reactive, low-surface-energy polymer at the surface, they reduce surface corrosion significantly. In Figure 12e, the potentiodynamic polarization curves for bare copper and PIPS, measured in 3.5 weight percent NaCl solution are shown. Using Tafel extrapolation, the corrosion current, I_{corr}, can be determined. This current was then used to determine the corrosion rate, CR, of the surfaces as

$$CR = \frac{I_{corr} K \cdot EW}{\rho A} \tag{10}$$

where K is a constant that defines the units of corrosion rate (K = 3272 mm/A-cm-year to find corrosion rate in mm/year), EW is the equivalent weight of the copper, ρ is the density, and A is the area of the tested surface. The corresponding corrosion rates are shown in Table 3. The corrosion rate of the PIPS on CuO nanoblades was more than two orders of magnitude less than a bare copper surface, providing significant surface protection.

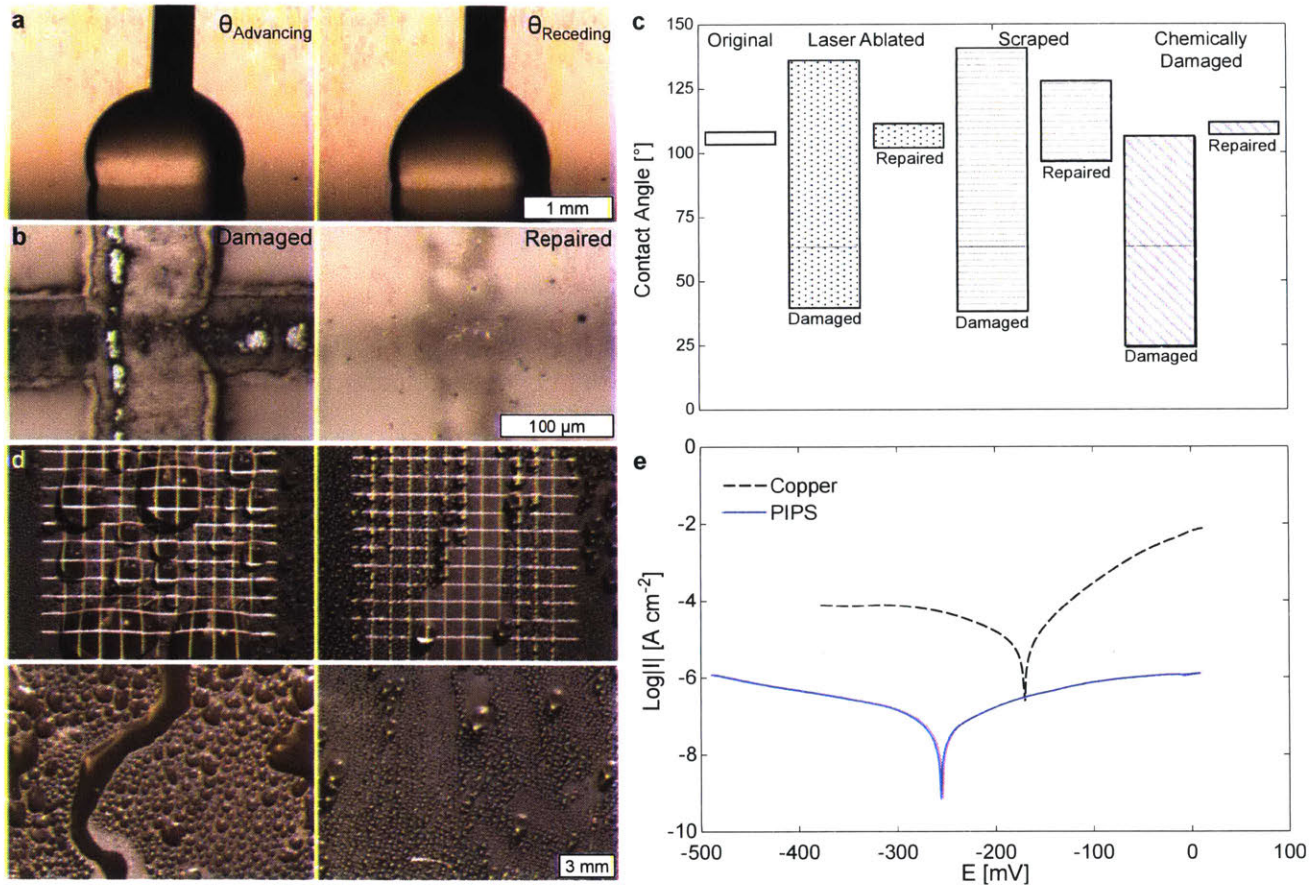

Figure 12: Properties of PIPS. Contact angle, self-healing, and corrosion resistance.

***a**, Advancing and receding contact angle measurement on copper oxide nanoblade PIPS. Hydrophobicity with low contact hysteresis was achieved. **b**, Left shows a PIPS surface damaged by laser ablation. The laser removed polymer from the surface and partially destroyed the nanostructure. However, by heating the surface past the melting point of the polymer, the surface self-healed. **c**, Advancing and receding contact angle of the PIPS surface. Advancing angle is the upper bound of the bar, whereas receding is the lower bound. After damage of various types, contact angle hysteresis was significantly increased. However, after healing, the original wetting properties are largely recovered. Scraping, i.e., significant damage to the surface and nanostructure, are most difficult to repair. **d**, Condensation on damaged PIPS (left) and repaired PIPS (right) for a laser ablated surface (top) and a chemically damaged surface (bottom). The damaged surface has large droplets on the surface due to the large contact angle hysteresis. After repair high quality dropwise condensation is recovered. **e**, Potentiodynamic polarization*

curves for bare copper and PIPS, measured in 3.5 weight percent NaCl solution. Corrosion current on PIPS is significantly reduced.

Table 3: Corrosion current and rate of copper and copper oxide nanoblade PIPS.

Surface	I_{corr} (A/cm^2)	CR (mm/year)
Copper	1.08E-5	0.25
PIPS	8.17E-8	0.0019

The, self-healing, corrosion resistant PIPS were next tested under conditions typical in a power plant condenser. An environmental chamber (Figure 13a) was used to control a pure vapor ambient for condensation. Experiments were run at 60 °C saturated vapor conditions. PIPS were fabricated directly on copper rods connected to a chiller loop, allowing accurate control over the condensation heat flux applied to the surfaces. Thermocouples embedded in the copper rod were used to extrapolate the heat flux, as well as heat transfer coefficient. This chamber allowed for simultaneous visualization of surfaces and monitoring of heat transfer performance during testing.

PIPS exhibited no observable degradation for 200 days of continuous testing (Figure 13b). In contrast, a 2 μm thick layer of Teflon AF on a flat surface of oxidized copper, i.e., a similar total thickness to PIPS on CuO nanoblades, experienced significant failure within hours, as can be seen in the images that show sections of the polymer delaminating from the surface due to poor adhesion. Furthermore, the heat transfer coefficient (HTC) of dropwise condensation on the high thermal conductance PIPS was comparable to that observed in the literature for previously developed, non-robust coatings (Figure 13c). The shaded regions show the expected performance of filmwise condensation and dropwise condensation, whereas the different lines are the expected performance including the thermal resistance of the coatings. Because the composite coatings have enhanced thermal conductance, the overall thickness could be increased significantly without decreasing heat transfer performance, whereas a traditional polymer coating would significantly reduce performance at a thickness of only a couple of micrometers. In fact, PIPS with copper nanowires demonstrated heat transfer performance near that expected of dropwise condensation without any coating resistance even at thicknesses above 20 μm.

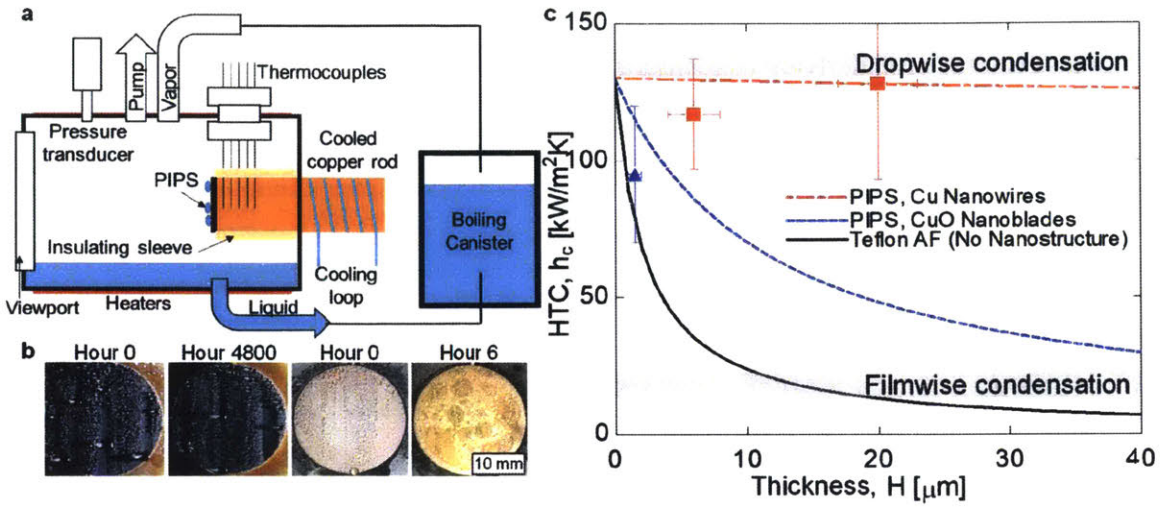

Figure 13: Robustness and Heat Transfer Testing of PIPS.

***a**, Schematic of environmental chamber for continuous testing of PIPS. A pure vapor ambient is maintained at controlled conditions. PIPS are fabricated directly on copper rods cooled by a chiller, inducing condensation on the surface at a controlled heat flux. A viewport on the window allows imaging of the surface. **b**, Images of PIPS and a Teflon AF coated flat copper condenser. PIPS maintained high-quality dropwise condensation for more than 200 days, whereas a Teflon AF coating of similar thickness on flat copper failed within hours. **c**, Measured condensation heat transfer coefficient. PIPS achieve performance similar to other state of the art coatings. However, due to the increased thermal conductivity, performance is not significantly reduced as coating thickness is increased, providing design flexibility.*

2.5 Conclusions and Outlook

At the demonstrated heat transfer performance and lifetime of PIPS, the coating enables a new regime of surface wetting modification previously not achieved (Figure 14a). Adequate lifetimes are achieved without sacrificing heat transfer enhancement. This was achieved by creating polymer infused porous surfaces that addressed the typical challenges associated with using low-surface-energy coatings. The composite surfaces we developed (Figure 14b), consisting of a high-thermal conductivity nanostructure filled with a hydrophobic polymer, create a predominately polymer surface. This renders the surface both hydrophobic and corrosion resistant. The nanostructures embedded within the polymer enhance the thermal conductivity, reducing constraints on the coating thickness while also greatly enhancing the adhesion of the coating, improving lifetime. Furthermore, the choice of nanostructure and polymer allow the

surface to be self-healing via heating. Therefore, not only are PIPS robust, high performance coatings, but they can also be easily repaired to any damage that does not significantly destroy the nanostructures or underlying condenser surface.

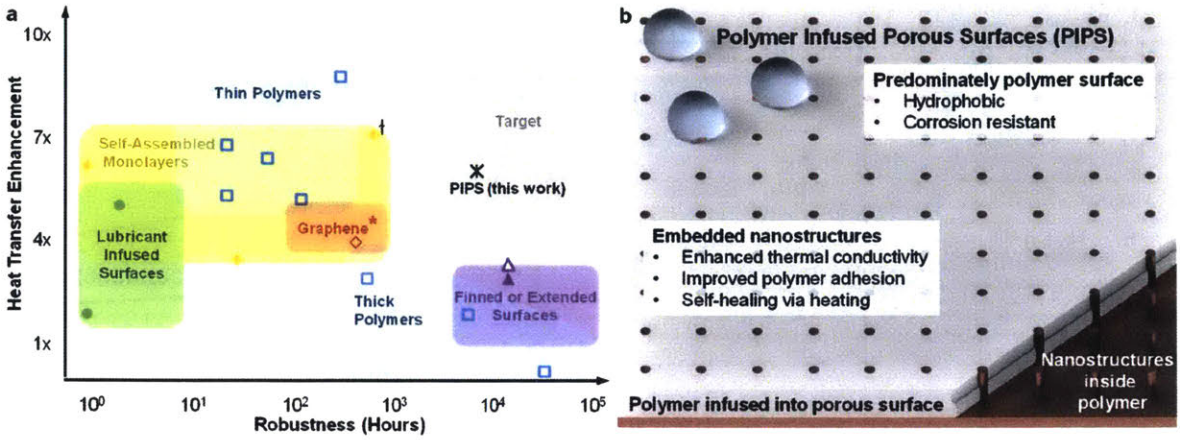

Figure 14: Comparison to previous work

a, *Heat transfer enhancement compared to robustness of previously developed coatings and PIPS. PIPS enabled the performance a lifetime needed.* ***b,*** *Advantages of PIPS.*

2.6 Methods

Fabrication of Surfaces

The fabrication procedure for PIPS is shown in Figure 11. Each step is described in further detail here.

Growth of CuO Nanoblades

The copper surfaces were first polished (SCRUBS Metal Polish Towel), cleaned with detergent (Alconox Detergent Powder), placed in an ultrasonic bath with isopropanol for 10 min, rinsed with deionized (DI) water, placed in 2 M hydrochloric acid for 30 seconds, rinsed with DI water, and then dried with compressed air. CuO nanoblades were then grown by immersing the cleaned tubes in alkaline solution composed of $NaClO_2$, NaOH, $Na_3PO_4 \cdot 12H_2O$, and DI water (3.75:5:10:100 wt %) at 96 °C for 1 hour. Based on literature characterization of this oxidation process, the CuO nanoblades have thickness of h ≈ 1 μm, solid fraction at the surface $\phi(x = 0)$ ≈ 0.023, and surface area enhancement of ≈ 10^{35}. The random orientation of the nanoblades also physically constrains the polymer to the surface, i.e., in order to delaminate the polymer coating must be significantly deformed.

Growth of Cu Nanowires

Copper nanowires were grown using a two-step templated electrodeposition process. The copper surfaces were first polished (SCRUBS Metal Polish Towel), cleaned with detergent (Alconox Detergent Powder), placed in an ultrasonic bath with isopropanol for 10 min, rinsed with deionized (DI) water, placed in 2 M hydrochloric acid for 30 seconds, rinsed with DI water, and then dried with compressed air. A 50 μm thick anodized aluminum oxide nanoporous membrane with pore diameter of 160 nm and solid fraction of 0.16 (InRedox), or 200 nm pore diameter and solid fraction of ≈ 0.4-0.5 (Sterlitech) was placed on copper surface. In the first electrodeposition step, a place of filter paper was then placed on top of the membrane and wetted with electrolyte (Elevate Cu Electrolyte 10). Finally, a piece of copper the same size as the surface (1 in diameter cylinders) was placed on top of the filter paper. The entire stack was clamped together and placed in the electrolyte. A constant current was then applied (2.5 mA for InRedox templates, 10 mA for Sterlitech templates) for one hour to bond the template to the copper surface. The clamp, filter paper, and second piece of copper were removed, leaving only the template bonded to the copper sample surface. The sample was then placed back into the electrolyte for the second electrodeposition step. A constant current was applied (2.5 mA for InRedox templates, 10 mA for Sterlitech templates), where the electrodeposition time controlled the thickness of the nanowire layer. A growth rate of 1.5 μm – 2 μm per hour was observed. After the desired thickness was reached, the surface was removed from the electrolyte, rinsed with DI water, and placed in 2 M NaOH solution for 3 hr to remove the AAO, leaving copper nanowires behind.

Infusion of Teflon AF

After growth of CuO nanoblades or Cu nanowires, Teflon AF 1601 (6% solution, Chemours) was spin coated on the surfaces at 1000 rpm. After spin coating, the surface was heated in argon to 330 °C with a ramp rate of 30 °C per minute, held at 330 °C for 30 minutes, and then allowed to cool to room temperature. This heating process allowed the spin coated layer to melt, and wick into the nanostructured surface. This spin coating process was then repeated until the nanostructure was completely filled, i.e., the number of spin coats was changed depending on nanostructure thickness and solid fraction, where each spin coat deposited ≈ 1 – 2 μm of Teflon AF.

Contact Angle Measurements

A custom-built experimental setup was used to measure contact angle (Figure 24a). The air and liquid temperature remained close to the surrounding laboratory temperature. A syringe pump (Micro4, World Precision Instruments) was used to add and remove water from a droplet on the surface. Note that the liquid was added and removed slowly enough that there was no dynamic effect on the contact angle, i.e., the capillary number was small. A DSLR camera (EOS

Rebel T3, Cannon) and macro lens were used to collect images of the droplet advancing on the surface. Lighting of the droplet was supplied with a light source (Intenselight C-HGFI, Nikon) and lens (C-HGFIB, Nikon). Contact angle was extracted from the images using ImageJ.

Self-Healing: Damage and Repair

The PIPS surface was damaged in three different ways. First was laser ablation using a commercial laser cutter (Epilog Laser Zing 24). The laser power was set to 15% and cutting speed to 100%. The laser cutter then produced a 10x10 grid of lines spaced 1 mm apart. This removed the polymer but did not completely destroy the nanostructure. Scraping was achieved using a multiblade cross hatch cutting tool (ISO 2409:2007), which destroyed both the polymer and nanostructure, and chemical damage was achieved here by placing the surface in a plasma chamber (790 series, Plasmatherm) for 3 minutes, which removed fluorination (and thus hydrophobicity) at the surface of the coating but left the underlying polymer and structure undamaged[104].

Corrosion Testing

The potentiodynamic polarization curves were measured in 1 liter of 3.5 weight percent NaCl solution. 1 cm^2 surfaces were used for the tests. The surface was first allowed to sit in the solution for 15 minutes before starting the test. Voltage was then swept at a rate of 0.1 mV/s from 250 mV below to 250mV above the open circuit voltage and the current monitored. Using Tafel extrapolation, the corrosion current was then determined[105].

Continuous Condensation Testing

Before condensation testing all thermocouples (ungrounded J-type, Omega) were calibrated to ±0.1 °C in a water bath (Lauda recirculating chiller). Surfaces for testing were prepared directly on 1 inch diameter copper cylinders that extended through the walls of an environmental chamber. These cylinders were connected to a chilling loop, which was used to set condensation heat flux. The environmental chamber was evacuated to less than 1 Pa to remove all non-condensable gases. Steam was then added via a boiler filled with degassed DI water. Steam conditions were set to 60 °C by heaters in the boiler, and the chamber walls were maintained at this temperature using heaters applied directly to the chamber walls. Steam pressure was monitored (Baratron Capacitance Manometer, MKS). Chiller temperature was set to produce roughly 50 thousand W/m^2 heat flux at the condenser surface, extrapolated from temperatures measured by 5 thermocouples embedded along the length of the copper cylinder. Fitting the temperature profile in the copper cylinder also allowed the surface subcooling, and condensation heat transfer coefficient, to be calculated. For long term testing, vacuum was

periodically pulled on the chamber to ensure non-condensable gases did not accumulate over time.

3. Omniphilic, Omniphobic, Switchable, and Selective Surfaces Independent of Surface/Liquid Chemistry

In classical wetting, control over surface chemistry is required to achieve the desired wetting behavior, which inherently limits this approach. Shifting the paradigm of liquid wetting behavior on surfaces promises widespread and powerful functionalities. For example, reentrant microstructures enabled omniphobic surfaces that repel all liquids, which was otherwise not possible. Similar success had not been achieved for other desired liquid behaviors. Here, we demonstrated a single surface design via reentrant microstructures that is not only omniphobic, but also omniphilic (wicks all liquids), switchable between repelling and wicking, and selective (repels or wicks certain liquids) without requiring complex chemical coatings. The reentrant microstructures utilize pinning of the three-phase contact line to create multiple stable wetting states. Therefore, all functionalities are achieved on the exact same surface simply by placing the surface in the corresponding stable state, removing the need to chemically modify a surface to achieve desired wetting behavior, impacting areas ranging from liquid separation, to metal processing, to microfluidics.

3.1 Introduction

In order to shift the paradigm that surface roughness only enhances intrinsic wettability and rather render a surface repellent to wetting liquids as well, surfaces with specific reentrant and doubly reentrant microstructures have been used[52,61,62]. As a wetting liquid comes into contact with a reentrant microstructure initially filled with air (Figure 15a i – Figure 15a ii), the three-phase contact line of the liquid pins at the reentrant feature (Figure 15a iii). This effect produces a surface tension force, F, that prevents liquid from entering the structure even for intrinsically wetting liquids (Figure 15a iv, which depicts a wetting liquid with $\theta = 45°$), thereby avoiding a completely filled wicking state (Figure 15a v). By using doubly reentrant microstructures, this approach enabled an unprecedented ability for any surface material to be omniphobic and repel all liquids[52]. However, similar success had not yet been achieved for other desired wetting behaviors such as wicking, selective surfaces, or switchable surfaces despite its potential to benefit a wide range of technical applications.

In this study, we conceived and demonstrated reentrant surface structures that are not only omniphobic, but also enable a variety of other desired wetting behaviors such as omniphilicity, i.e., wicking all liquids including non-wetting liquids. Control over the initial wetting state of the reentrant surface dictates its behavior as repellent or wicking. If a surface with reentrant microstructures starts in a liquid-filled state (Figure 15b i), contact line pinning occurs at the reentrant feature as the liquid is removed from the surface (Figure 15b ii and iii). This creates a surface tension force that keeps even a non-wetting liquid within the structure

(Figure 15b iv, which depicts a non-wetting liquid with $\theta = 135°$), avoiding a completely dry repellent state (Figure 15b v). Instead, the surface becomes wicking.

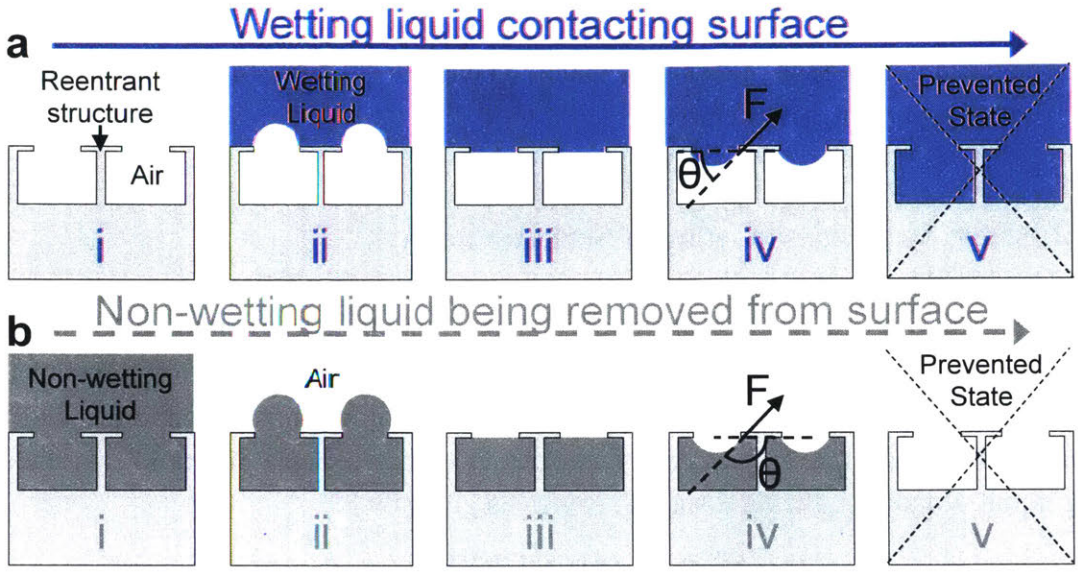

Figure 15: Reentrant surfaces: the ability to both repel and wick all liquids.

***a**, A reentrant structure initially filled with air (i) begins filling with a wetting liquid from above (ii). The three-phase contact line pins at the reentrant feature (iii) which produces a surface tension force, F, that prevents liquid from entering the structure further regardless of contact angle, θ (iv). Therefore, the structure is unable to fill completely (v) and the surface remains repellent. **b**, A reentrant structure initially filled with a non-wetting liquid (i) begins emptying (ii). The three-phase contact line pins at the reentrant feature (iii) which produces a surface tension force, F, that prevents liquid from being removed further regardless of contact angle, θ (iv). Therefore, the structure is unable to empty completely (v) and the surface remains wicking.*

Therefore, reentrant structures create bistable surfaces (surfaces with two stable states), where a local energy minimum enables both wicking and repellency independent of the intrinsic wettability of the liquid/surface used. In this work, we first demonstrate these bistable surfaces through characterization of wetting behavior, demonstrating both omniphobicity and omniphilicity on the same surface. We show that the surface can maintain both positive and negative Laplace pressures, i.e., the pressure generated by a curved liquid-gas interface, which is what allows the bistable surface. We then discuss a variety of functionalities these surfaces enable along with experimental demonstrations. For example, these bistable surfaces can be actively switched between the wicking and repellent state, creating surfaces where wetting

behavior is controlled between both wetting extremes, which is typically very challenging[55]. We also show selective wicking and repellency, i.e., the ability to wick certain liquids while repelling others, which would otherwise require complex chemical modification of the surface specific to the liquids for which selectivity is desired[106]. This switchable, selective, omniphilic/omniphobic surface enables unique capabilities in tailoring the behavior of liquids on solid surfaces independent of liquid/surface chemistry.

3.2 Bistable Surfaces: Modeling of Surface Energy

This bistable surface can be understood by modeling the total surface energy as a function of the liquid volume while a wetting liquid is added to the reentrant structure and while a non-wetting liquid is removed from the structure (based on states shown in Figure 15). The calculation was based on a unit depth of the unit cell with dimensions scaled to those of the reentrant surfaces that were fabricated and experimentally tested (see Figure 17). In the case of a wetting liquid, for state i, the total surface energy is given by

$$E_1^w = \gamma_{sg}(4D + l + 2H) \tag{11}$$

where γ_{sg} is the surface energy of solid-gas interfaces and the thickness of the overhang is assumed to be minimal compared to other dimensions. The initial gas volume is set to be V_0. As liquid is added from above, more solid-gas interfaces are replaced by liquid-gas interfaces. The top corner of the overhang creates a local energy barrier, where the three phase contact line pins. As pinning occurs, with more liquid added to the system, the liquid-gas and solid-gas interface area stays the same while the liquid-gas interface area decreases until the liquid-gas interface becomes flat (state iii). Between state ii and state iii, the total surface energy is

$$E_{23}^w = \gamma_{sg}(4D + l - d + 2H) + \gamma_{sl}d + 2\gamma_{lg}R_{lg}(\pi - \xi) \tag{12}$$

where γ_{sl} is the surface energy for solid-liquid interfaces, γ_{lg} is the surface energy for liquid-gas interfaces, R_{lg} is the radius of curvature of the liquid-gas interface, and ξ is the contact angle of the liquid front with regard to the top surface. During this stage, $\theta < \xi < \pi$ and

$$R_{lg} = \frac{l - d}{2\cos\left(\xi - \frac{\pi}{2}\right)} \tag{13}$$

and the liquid volume can be written as

$$V_{23}^w = V_0 - (l - d)H - {R_{lg}}^2\left[(\pi - \xi) - \frac{\sin 2(\pi - \xi)}{2}\right] \tag{14}$$

After state iii, the liquid-gas interface area starts increasing again while we add more liquid into the system. Between state iii and state iv, the total surface energy is

$$E_{34}^{w} = \gamma_{sg}(4D + l - d + 2H) + \gamma_{sl}d + 2\gamma_{lg}R_{lg}\psi \tag{15}$$

where ψ is the contact angle of the liquid front with respect to the bottom surface of the overhang, which varies from 0 to θ. During this stage,

$$R_{lg} = \frac{l - d}{2\cos\psi} \tag{16}$$

and the liquid volume can be described as

$$V_{34}^{w} = V_0 - (l - d)H + {R_{lg}}^2\left[[\psi - \frac{\sin 2\psi}{2}\right] \tag{17}$$

Adding more liquid after $\psi = \theta$ results in the solid-liquid interface area replacing the solid-gas interface area inside the structure. Eventually, at state v, the unit cell is filled with liquid, and the total surface energy is

$$E_{5}^{w} = \gamma_{sl}(4D + l + 2H) \tag{18}$$

In the case of removing non-wetting liquid from the unit cell, at state i, the unit cell is filled with liquid, so

$$E_{1}^{nw} = \gamma_{sl}(4D + l + 2H). \tag{19}$$

Between state ii and state iii,

$$E_{23}^{nw} = \gamma_{sl}(4D + l - d + 2H) + \gamma_{sg}d + 2\gamma_{lg}R_{lg}\chi \tag{20}$$

where χ is the contact angle of the liquid front with respect to the top surface, and

$$R_{lg} = \frac{l - d}{2\cos\chi} \tag{21}$$

The liquid volume during this stage is

$$V_{23}^{nw} = (l - d)H + {R_{lg}}^2\left[(\pi - \xi) - \frac{\sin 2\chi}{2}\right] \tag{22}$$

Between state iii and state iv,

$$E_{34}^{nw} = \gamma_{sl}(4D + l - d + 2H) + \gamma_{sg}d + 2\gamma_{lg}R_{lg}(\pi - \varphi) \tag{23}$$

where φ is the contact angle of the liquid front with respect to the bottom surface of the overhang, and during this stage,

$$R_{lg} = \frac{l - d}{2\cos(\pi - \varphi)} \tag{24}$$

The liquid volume can be expressed as

$$V_{34}^{nw} = V_0 - (l - d)H + {R_{lg}}^2 \left[[\psi - \frac{\sin 2\,(\pi - \varphi)}{2} \right] \tag{25}$$

When the liquid is completely removed from the unit cell, the total surface energy then becomes

$$E_5^{nw} = \gamma_{sg}(4D + l + 2H) \tag{26}$$

The results of this surface energy model are shown in Figure 16. Independent of whether or not a wetting or non-wetting liquid is used, a local energy minimum on the surface enables the surface to wick or repel the liquid. Note, the total surface energy and the liquid volume are normalized to take values between 0 and 1. Therefore, the values in Figure 16 do not have specific physical meanings whereas the trend does show that a stable energy state (a local energy minimum) exists for both wicking and repelling independent of the intrinsic wettability of the liquid/surface used.

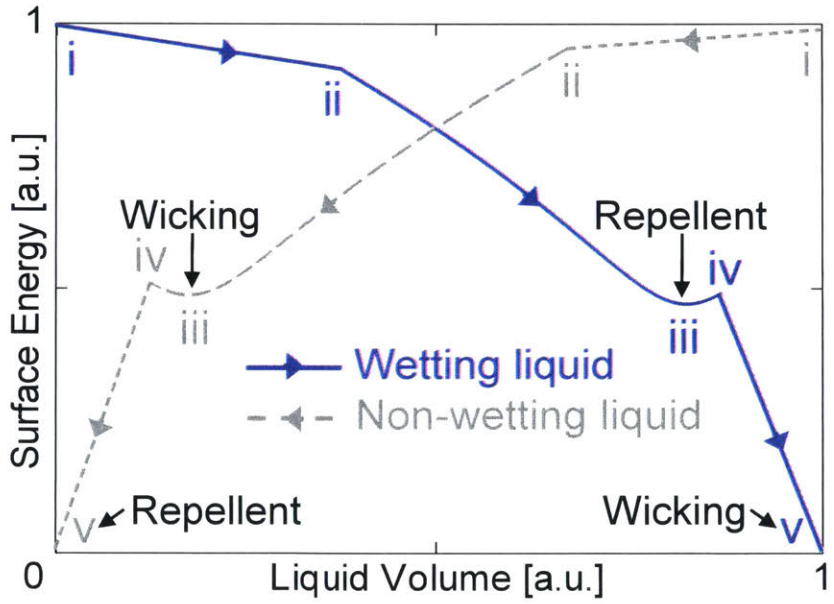

Figure 16: Bistable surfaces for wicking or repelling any liquid.

The total surface energy while a wetting liquid is added to a reentrant structure (blue line) and while a non-wetting liquid is removed from the structure (dashed grey line). States i through v from Figure 15a and Figure 15b are labeled. The surface is always bistable regardless of whether a wetting or non-wetting liquid is used due to contact line pinning between states ii and iv, enabling both repellency and wicking for all liquids. Line segments i-ii and iv-v capture the

overall change in surface energy between these states which were not solved explicitly given the dependence on the specific geometry and liquid path.

3.3 Fabrication and Testing of Reentrant Channels

To experimentally demonstrate that reentrant structures enable repellency, wicking, switchability, and selectivity with a single surface design, we fabricated normal microchannels (no reentrant feature) and reentrant microchannels. Channels were chosen due to the simplicity of fabrication and the well-established understanding of typical wetting behavior[97]. The normal channels were fabricated in silicon (Figure 17a) and had channel walls of width d, height H, and pitch l. The reentrant channels were fabricated in silicon with a silicon dioxide reentrant overhang (Figure 17b) of thickness t, length D, and reentrance angle α (Figure 19b). We fabricated surfaces with $l = 500$ μm, $H \approx 400$ μm, $d = 90$ μm, $t = 1$ μm, $D = 25$ μm, and $\alpha = 90°$ (schematics of surface shown in Figure 17c and d and a typical sample cross section in Figure 17e). We chose to use reentrant microstructures as opposed to doubly reentrant structures given fabrication is less complex and most liquids do not exhibit a contact angle of 180°. Therefore, doubly reentrant structures are not required to achieve the desired wetting behavior.

Table 4 summarizes the geometry of tested samples. Before testing, unless otherwise stated, the surfaces were coated with a conformal, 60 nm thick, low-surface-energy polymer (C_4F_8) to create a uniform and repeatable contact angle across different tested surfaces, but the coating is not required for the functionalities we demonstrate.

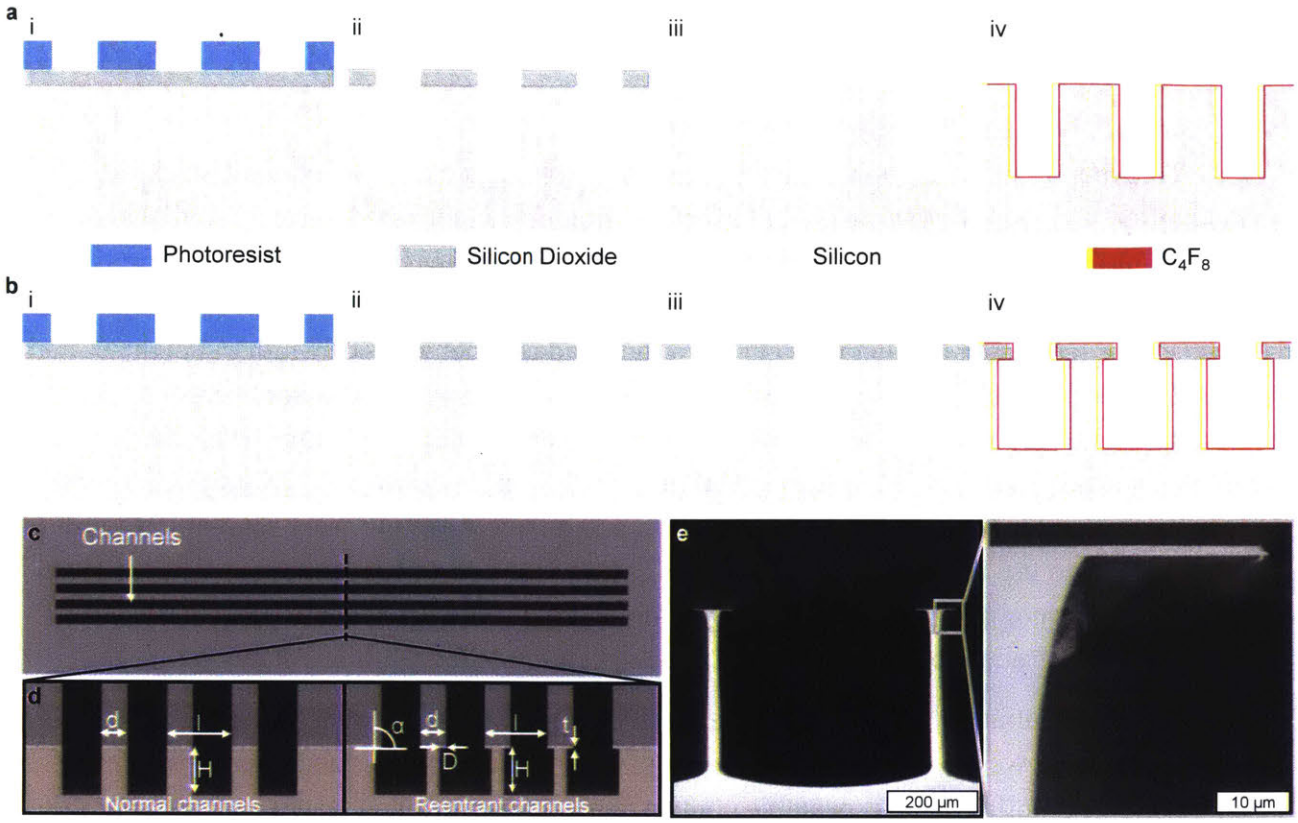

Figure 17: Fabricated surfaces.

***a**, Normal channel fabrication. i. Photoresist exposure and development. ii. Reactive ion etch of the silicon dioxide and silicon to form channels. iii. Removal of oxide layer to ensure no reentrant feature was unintentionally created during reactive ion etching. iv. Deposition of a conformal hydrophobic coating to enable a range of intrinsic contact angles on the surface. **b**, Reentrant channel fabrication. i. Photoresist exposure and development. ii. Reactive ion etch of the silicon dioxide and silicon to form channels. iii. Isotropic etch of silicon to create a reentrant feature made of silicon dioxide. iv. Deposition of a conformal hydrophobic coating to enable a range of intrinsic contact angles on the surface. **c**, Top view of a 3D schematic of the surfaces consisting of parallel channels. Although only four channels are depicted, surfaces had up to 10 to allow for sufficient area to characterize the apparent contact angle on the surface. **d**, Cross-sections of the 3D schematic for normal channels (left) and reentrant channels (right). **e**, Cross-section scanning electron microscope images of a cleaved section of a reentrant channel surface used in this work.*

Table 4: Tested surfaces

Geometric parameters of tested surfaces. l is pitch, d is width of the channel wall or reentrant feature, h is the channel height, t is the thickness of the reentrant feature, D is the length of the reentrant overhang, α is the reentrance angle, ϕ is the surface solid fraction, r is the roughness factor of the entire surface, r_f is the roughness factor of the reentrant feature or in the case of normal channels of the top of the channel wall, and the critical contact angle is the intrinsic contact angle at which the hemiwicking and Cassie states are expected to occur.

Sample #	l [μm]	d [μm]	H [μm]	t [μm]	D [μm]	α [deg]	ϕ [-]	r [-]	r_f [-]	Critical cosθ [-]
1	500	90	400	-	-	0	0.18	2.6	1	± 0.34
2	500	90	400	1	25	90	0.18	2.7	1	± 0.33

First, we demonstrate that, in contrast to normal channels, reentrant microstructures enable both omniphilicity and omniphobicity. In this experiment, the apparent contact angle (cos θ^*) was measured for a variety of liquids with different intrinsic contact angles (cos θ) ranging from highly wetting to highly non-wetting (liquid properties listed in Table 5).

Table 5: Liquid properties

*Properties of tested liquids. Water and ethanol are soluble, and may therefore be used to create liquids with a range of surface tensions and contact angles[107]. Weight percentages of the components are listed. *Surface tension values are for the liquid in air.*

Liquid [weight percent]	Surrounding environment	Density [kg/m^3]	Surface tension [N/m]	θ_{adv} [degrees]	θ_{rec} [degrees]
Mercury	Air	13690	0.430	143.6	132.1
Water	Air	997	0.0721	116.0	95.8
92% Water, 8% Ethanol	Air	986	0.0599	105.0	90.0
83% Water, 17% Ethanol	Air	973	0.0502	91.6	69.4
68% Water, 32% Ethanol	Air	949	0.0402	74.6	57.3
38% Water, 62% Ethanol	Air	888	0.0302	56.4	40.3
Ethanol	Air	789	0.0232	43.0	30.5
FC-40	Air	1855	0.0160	3.0	0
Water	Hexane	997	0.0721*	25.4	-
Hexane	Water	655	0.0184*	150	-

A syringe was used to add and remove a droplet from the surface, while a camera recorded the apparent contact angle as the droplet's three-phase contact line advanced and receded parallel to the channels. Although Eq. 2 predicts a single value for the apparent contact angle on a surface, a range of values have often been observed due to distortion of the three-phase contact line and variation in the surface solid fraction on the heterogeneous surface[108]. This leads to variation in the contact angle as the droplet grows (advancing contact angle) and as it shrinks (receding contact angle). Furthermore, on it can lead to differences in the advancing and receding contact angles depending on the orientation of the droplet relative to the surface structures. Therefore, the "local" solid fraction at the three-phase contact line has been used[97,109,110]. The solid-fraction of the three-phase contact line may vary when a droplet moves perpendicular to the channels (compare planes 3 and 4 in Figure 18). However, parallel to the channels, the solid fraction remains constant (e.g., comparing planes 1 and 2 in Figure 18). As such, we use the contact angle measurement parallel to the channels while interpreting the experimental results. Parallel to the channels $\phi = d/l$ and for the Wenzel state $r = (2h+l)/l$.

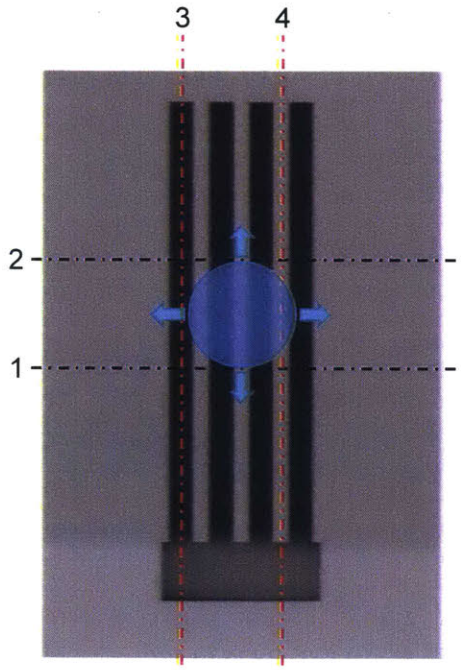

Figure 18: Wetting on channels

Liquid placed on top of channels rests on a heterogeneous surface. As the liquid moves in different directions, the three-phase contact line observes a different solid fraction. We compare the solid fraction at plane 1 and 2. As the droplet moves parallel to the channels, the surface the three-phase contact line interacts with remains the same. However, when the droplet moves

perpendicular to the channels, the three-phase contact line may observe different solid fractions ranging from 0 to 1 (plane 3 and 4, respectively).

The advancing contact angles of the normal channels (black triangles in Figure 19a) highlighted typical wetting behavior where highly wetting liquids formed the hemiwicking state, moderately wetting liquids formed the Wenzel state, and non-wetting liquids formed the Cassie state. Note that the Cassie state was observed at contact angles less than the critical angle due to a commonly observed metastable Cassie state[45]. Reentrant channels, on the other hand, allowed the Cassie state to be extended to wetting liquids (area shaded in red indicates region that requires reentrant geometry for repellency) by trapping air within the channels (red squares). Therefore, θ^* was determined by Eq. 4 and the surface was repellent for all liquids, hence achieving omniphobic behavior. However, we also show that by first filling the reentrant channels with the same liquid as that in the syringe, i.e., placing the surface into a stable wicking state, the hemiwicking state was also extended to non-wetting liquids (blue squares, area shaded in blue indicates region that requires reentrant geometry for hemiwicking). As such, Eq. 3 governed the wetting behavior and a small apparent contact angle was achieved for all liquids regardless of intrinsic contact angle (omniphilic behavior). Counterintuitively, the exact same surface was able to exhibit both omniphobic and omniphilic behavior. Therefore, a liquid such as ethanol that is typically wetting on a flat surface can have both wicking and repellent behavior on a reentrant surface (Figure 19b). Similarly, a typically highly non-wetting liquid such as mercury may also have both wicking and repellent behavior. The receding contact angle had similar behavior (Figure 19c).

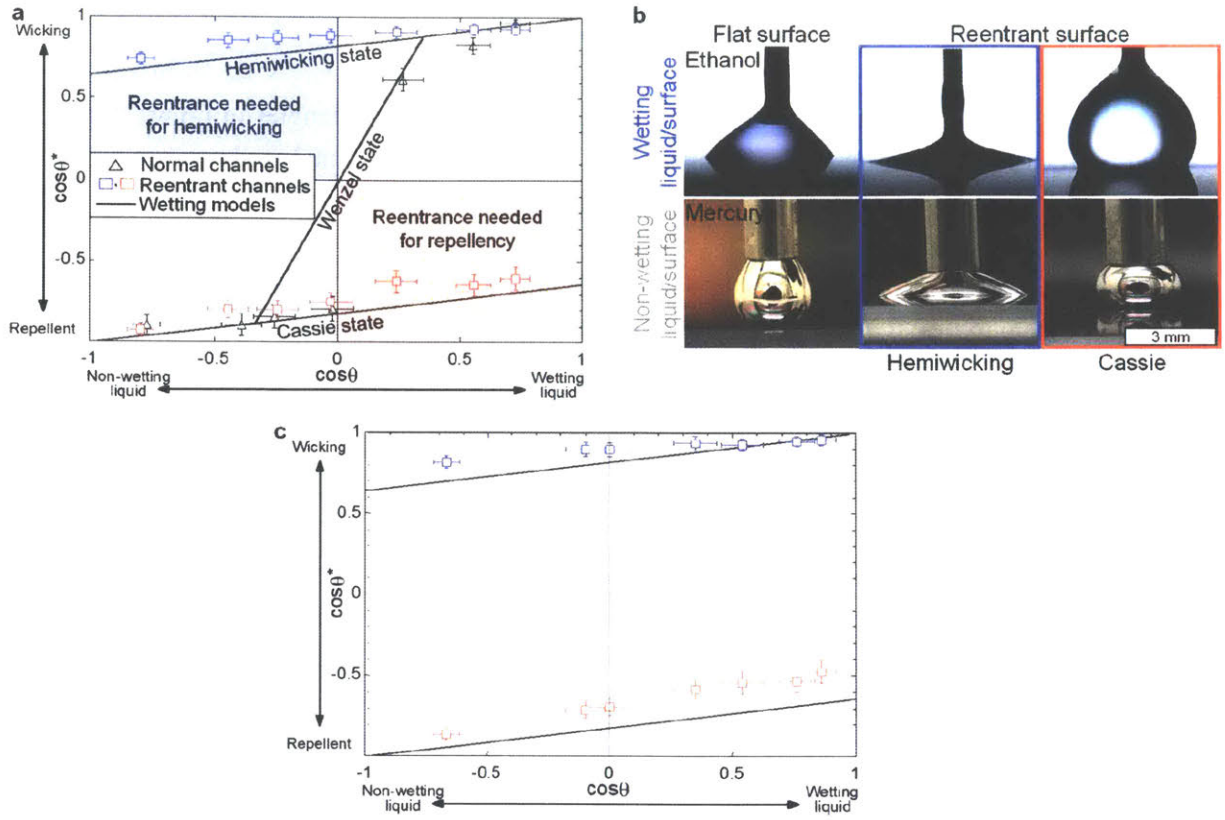

Figure 19: Omniphilic and omniphobic behaviors.

***a**, Apparent advancing contact angle (cos θ*) on normal and reentrant microstructures parallel to the channels for liquids with different intrinsic wettability (cos θ). The normal channels highlight typical behavior, where non-wetting liquids form a Cassie wetting state with large apparent contact angle, while wetting liquids form a hemiwicking state with small apparent contact angle. Reentrant features, however, enable both of these states to be extended to all liquids, regardless of intrinsic wettability. **b**, Images of a wetting liquid (ethanol) and a non-wetting liquid (mercury). The first column shows the liquids on a smooth surface (intrinsic contact angle). Reentrant surfaces were able to achieve both wicking (blue box) and repellency (red box) for both liquids despite their intrinsic wetting behaviors. **c**, Apparent receding contact angle (cos θ*) on reentrant microstructures parallel to the channels for liquids with different intrinsic wettability (cos θ), where the receding contact angle on a smooth surface is used for the intrinsic wettability. The same behavior was observed as that for the advancing contact angle in Figure 19a.*

The reason for this contradictory wetting behavior is the reentrant surface's unique ability to sustain both positive and negative Laplace pressures, P_L, independent of the liquid's intrinsic contact angle (Figure 20). We quantify this pressure by measuring the capillary height of the surface. A rough surface dipped into a liquid exhibits a capillary height, h, similar to a capillary tube. This capillary height is a function of the geometry of the surface roughness, the liquid properties, and the contact angle formed between the liquid and the solid. The surface tension of the liquid produces a force, F_l, which can either prevent liquid from entering the roughness or draw the liquid into the roughness. The vertical component of this force, $F_{l,y}$, dictates the behavior and for a normal channel (Figure 20a) is given by:

$$F_{1,y} = \gamma L \cos\theta \tag{27}$$

where γ is the surface tension of the liquid and L is the length of the channel. If the liquid is wetting ($\theta < 90°$), this force is positive and if the surface is non-wetting ($\theta > 90°$), the force is negative. Therefore, the pressure a channel can withstand, P_L, is the sum of the forces on both sides of the channel, divided by the projected area of the channel:

$$-P_L = \frac{2F_{1,y}}{(l-d)L} = \frac{2\gamma\cos\theta}{(l-d)} \tag{28}$$

In this equation, θ and d dictate the curvature of the liquid-gas interface and is therefore the same equation as that for the Laplace pressure[111]. Meanwhile, the hydrostatic pressure, P_h, as a function of liquid height is:

$$-P_h = \Delta\rho g h \tag{29}$$

where $\Delta\rho$ is the density difference between the liquid and air and g is the gravitational acceleration. By setting P_L equal to P_h and rearranging for h we find:

$$h = \frac{2\gamma\cos(\theta)}{(l-d)\Delta\rho g} \tag{30}$$

However, the reentrant structure modifies the apparent contact angle in the channel (Figure 20b). In the Cassie state, the reentrant feature increases the contact angle by α, whereas in the hemiwicking state, it reduces the contact angle by α. Eq. 31 is then modified to account for reentrance as:

$$h = \frac{2\gamma\cos(\theta \pm \alpha)}{(l-d)\Delta\rho g} \tag{31}$$

Finally, we also recognize that due to contact line pinning the maximum force may not occur at $\theta + \alpha$. Rather, as the liquid advances or recedes in the reentrant channel the maximum vertical component of the contact line force occurs when $\theta + \alpha = 180°$ for the Cassie state and $\theta - \alpha = 0°$

for the hemiwicking state (Figure 20c). Therefore, in the Cassie state, when $\theta + \alpha > 180°$, the liquid entering the structure must pass through this maximum and $\theta + \alpha$ is set to 180° instead. Similarly, when $\theta - \alpha < 0°$, we set $\theta - \alpha$ to 0 for the hemiwicking state.

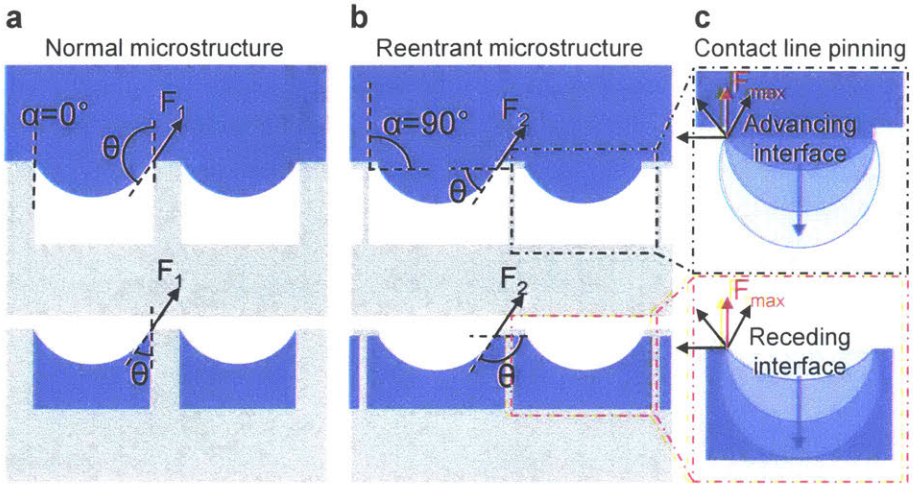

Figure 20: Surface tension forces for positive and negative Laplace pressures.

***a**, The surface tension force on a normal microstructure, F_1, that enables air to be trapped within the surface (top schematic) or enables liquid to wick up the surface when dipped into a liquid (bottom schematic). On a normal microstructure, air is trapped when $\theta > 90°$ (negative capillary height) and liquid may wick up the surface when $\theta < 90°$ (positive capillary height). **b**, The surface tension force on a reentrant microstructure, F_2, that enables air to be trapped within the surface (top schematic) or enables liquid to remain in the structures (bottom schematic) when dipped into or pulled out of a liquid, respectively. On a reentrant microstructure with $\alpha = 90°$ air is trapped when $\theta > 0°$ (negative capillary height) and liquid may remain in the structure when pulled out of a liquid when $\theta < 180°$ (positive capillary height). **c**, When $\theta + \alpha > 180°$, contact line pinning at the reentrant feature causes the advancing interface of liquid being pushed into the reentrant feature to pass through a maximum for Eq. S8. Therefore, this maximum is used for capillary height estimations. Similarly, when $\theta - \alpha < 0°$, the receding interface of liquid within the reentrant structure also passes through a maximum.*

A normalized capillary height, h^*, is then calculated to account for the surface geometry and different properties of liquids used as:

$$h^* = \frac{h\big((l-d)\Delta\rho g\big)}{2\gamma} = \cos(\theta \pm \alpha) \tag{32}$$

A surface without reentrance ($\alpha = 0°$) has a positive capillary height for wetting liquids and a negative capillary height for non-wetting liquids, a behavior which was captured by the normal channels (black triangles in Figure 21b). When the surface was dipped into a pool of wetting liquid it exhibited hemiwicking, where the liquid rose up in the channels a given height due to the negative Laplace pressure counteracting gravity. In contrast, when a non-wetting liquid was used, air was trapped within the surface down to a given depth in the liquid due to the positive Laplace pressure. However, adding reentrance ($\alpha = 90°$) allowed both negative (red squares) and positive (blue squares) capillary heights for all liquids simply by controlling the initial wetting state. The error bars for the positive capillary height reentrant surface were larger to account for the receding contact angle governing the capillary height as opposed to the advancing contact angle. When a reentrant channel prefilled with liquid, i.e., in the hemiwicking state, was raised out of the liquid (Figure 21c, which shows a liquid with $\theta = 91.6°$), liquid remained trapped within the structures. At a given height, the maximum sustainable capillary height was exceeded and the liquid dewet from the reentrant channels. Likewise, when a reentrant channel filled with air was lowered into the same liquid (Figure 21d), air remained trapped within the structures. At a given depth into the liquid, the maximum negative capillary height was exceeded and the liquid entered the reentrant structures.

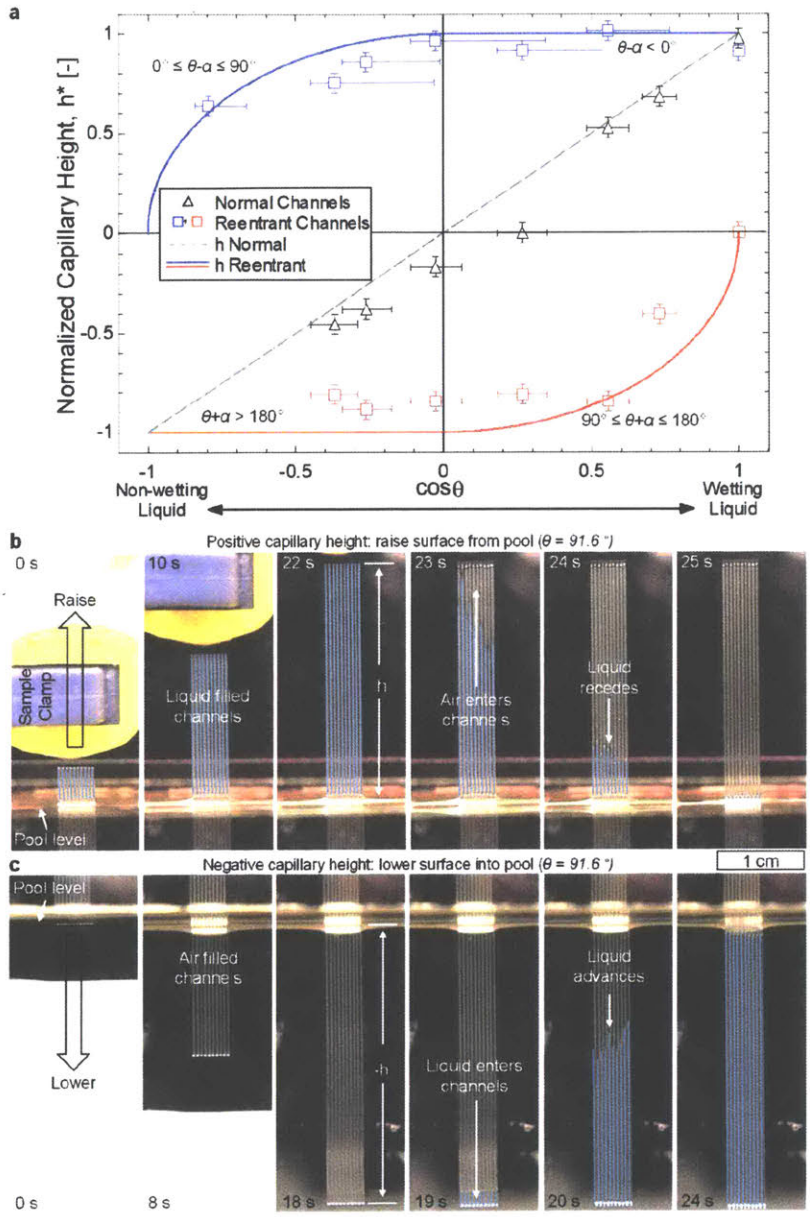

Figure 21: Both positive and negative Laplace pressures on the same surface.

***a**, Normalized capillary height on normal and reentrant channels for liquids with different intrinsic wettability. The normal channels highlight typical behavior, where non-wetting liquids trap air to a given liquid depth and wetting liquids fill the roughness to a given height (black triangles). Reentrant channels dipped in liquid, however, trapped air for wetting liquids as well*

(red squares). Furthermore, when prefilled with liquid, reentrant channels allowed a positive capillary height for all liquids (blue squares). ***b****, Time-lapse images showing reentrant channels prefilled with liquid with* $\theta = 91.6°$ *being raised from a pool of the same liquid. Once the capillary height was exceeded, the channel naturally dewet. This corresponded to the bistable surface transitioning from its local energy minimum hemiwicking state into its global energy minimum state. The liquid is false coloured blue for convenience.* ***c****, Time-lapse showing reentrant channels filled with air being dipped into a pool of liquid with* $\theta = 91.6°$*. Once the capillary height was exceeded, liquid entered the channels. This corresponded to the bistable surface transitioning from its local energy minimum repellent state into its global energy minimum state.*

3.4 Applications of Omniphilic/Omniphobic Bistable Surfaces

The measurements of apparent contact angle and capillary height highlight that reentrant surfaces enable stable states for both wicking and repellency of all liquids on the exact same surface independent of intrinsic wettability. This omniphilic/omniphobic duality can be utilized to enhance current technologies and also enables a number of unique wetting functionalities. First, the ability to achieve wicking and repellency independent of the intrinsic wettability of the surface material, as presented in this work, broadens the potential materials used for many applications. For example, a surface can be made highly wetting and wicking to typically non-wetting liquids such as metals (Figure 22a shows mercury highly wetting on the surface). This ability could be useful in many scenarios, such as high temperature heat pipes[44] or metal processing[112], which use liquid/surface combinations that are often non-wetting but could benefit greatly from wetting or wicking. For example, ceramic materials must be used in high temperature heat pipes due to their temperature stability, however, these ceramics are generally non-wetting, and therefore non-wicking to liquid metals. Alternatively, a surface can be made repellent which is useful in chemical processing[113] and phase-change heat transfer[49]. Finally, because the wetting behavior can be made independent of the intrinsic wettability, wicking or repellent systems that are robust to changes in intrinsic wettability due to surface contamination or degradation are also possible, both of which commonly occur in systems that rely on chemical modification to tailor wetting[14,54].

Furthermore, a filled reentrant channel can support both positive and negative Laplace pressures (Figure 22b i). In fact, the channel can simultaneously exhibit both positive and negative Laplace pressures. This enhances the total Laplace pressure of the surface, which can be used to further enhance the capillary height and wicking[1]. To demonstrate this ability, we conducted another capillary height experiment in which the channels were prefilled, but no pool of liquid was used such as in Figure 20b and c. Instead, the capillary height was increased by

gradually tilting the prefilled surface starting from horizontal (Figure 22b ii, in which ethanol was used). The observed capillary height (*h enhanced*) was the sum of the heights predicted by Eq. 31 for the positive (h +) and negative (h -) Laplace pressures. The sustainable capillary height of the surface was greatly increased for a variety of liquids with a range of intrinsic wettability (Figure 22c).

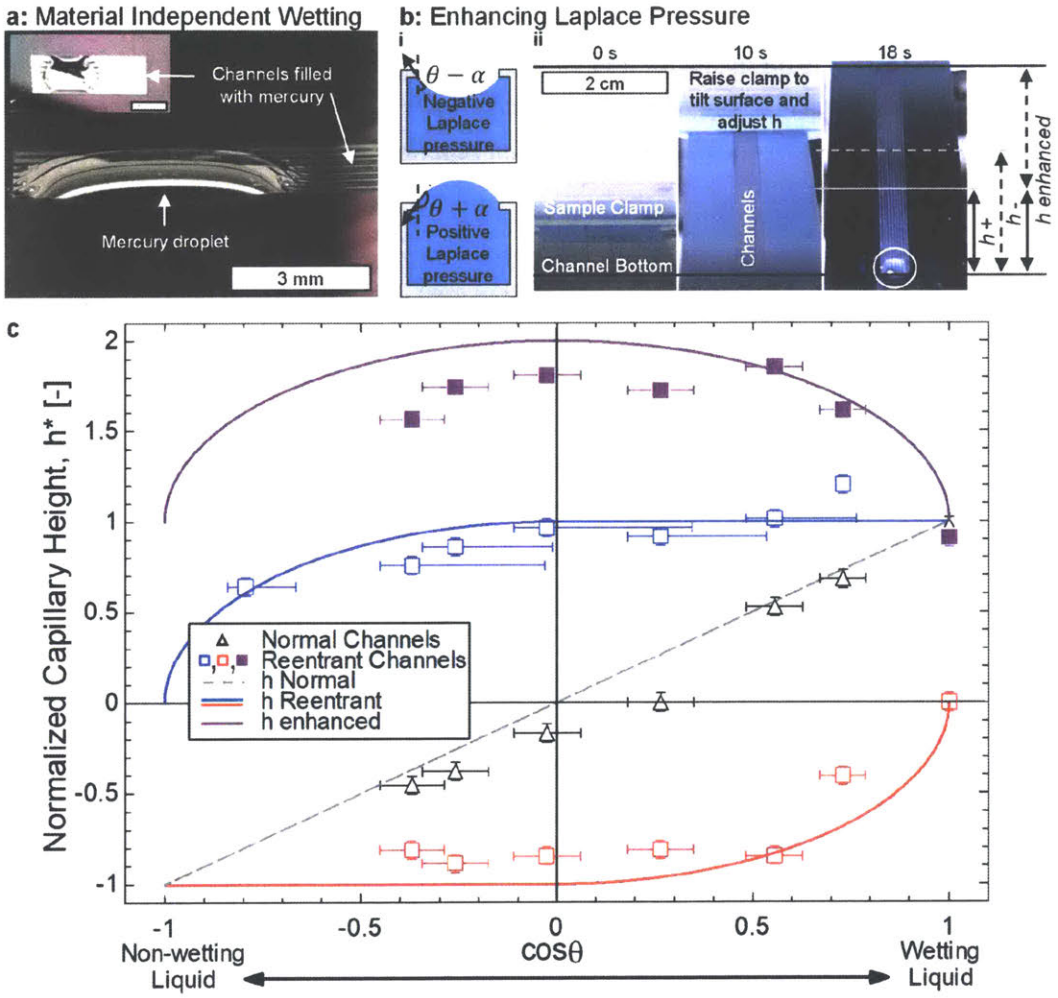

Figure 22: Applications of omniphilic/omniphobic surfaces.

***a**, Mercury filled in the channels of the reentrant surface, thus rendering that section of the surface highly wetting despite mercury's highly non-wetting intrinsic nature on the surface. The inset shows the top view of the channels at smaller magnification. **b**, (i) Schematics of liquid in a reentrant channel. Due to the reentrant feature, the same channel can sustain both negative and positive Laplace pressures. (ii) Time-lapse images measuring the capillary height by tilting the*

reentrant channel surface prefilled with ethanol. The observed capillary height was greatly increased. h + and h - are the portions of the capillary height from the positive and negative capillary pressures, respectively, and combined equal h enhanced. The white circle shows the ethanol bursting from the lower portion of the channels as the maximum capillary height was exceeded and liquid receded from the higher portion of the channels. ***c****, Normalized capillary height on normal and reentrant channels for liquids with different intrinsic wettability. The normal channels highlight typical behavior, where non-wetting liquids trap air to a given liquid depth and wetting liquids fill the roughness to a given height (triangles). Reentrant channels dipped in liquid, however, trap air for wetting liquids as well (red squares). Similarly, when prefilled with liquid, reentrant channels allow a positive capillary height for all liquids (blue squares). Furthermore, the reentrant surface is able to sustain both negative and positive Laplace pressures simultaneously. Therefore, reentrant structures further enhance the capillary height by utilizing both Laplace pressures (purple filled squares). These measurements were conducted by prefilling the channels, but not dipping the channels into a pool of liquid. Instead, the channels were initially horizontal and were then tilted. As the surface was tilted the hydrostatic pressure increased. The point at which the liquid dewet from the channel was recorded as the enhanced capillary height, h enhanced. The purple solid line is the sum of the positive and negative capillary height predictions.*

In addition, because the surface is bistable, it is possible to actively switch the surface between wicking and repellent behavior (Figure 23a). In this demonstration, liquid droplets with an intrinsic advancing contact angle of 91.6° were added to the reentrant channel surface. Initially, the surface was filled with air and as such, was repellent with high droplet mobility. However, by pumping the same liquid into the channels via a reservoir, the surface was switched to a wicking state where liquid added to the surface was sucked into the structures. By once again removing the liquid in the channel (achieved in this demonstration by exceeding the capillary height such that gravity naturally emptied the channels), the surface transitioned back to the repellent state, demonstrating a simple method for active tailoring of the surface wettability between the two extreme wetting states, which would typically require complex coatings and external stimuli to change the chemical nature of the surface[114]. Furthermore, even with active methods to tailor intrinsic contact angle such as electrowetting, switching between these two extreme wetting states had not been achieved[55].

Finally, we demonstrate the wetting behavior of the reentrant structures is determined solely by the initial wetting state in other systems as well, i.e., liquid-liquid mixtures. Therefore, although the previously described experiments were demonstrated in liquid-air systems, by

infusing (prefilling) reentrant microstructures with a desired liquid, selective wetting of surfaces was enabled. One liquid may be selectively wicked or repelled in the presence of another liquid without the need for complex chemical coatings. In this demonstration, reentrant channels without the C_4F_8 coating, i.e., a simple silicon and silicon dioxide surface without a chemical coating, were able to repel and absorb both hexane in a water environment and vice versa (Figure 23b). In the first image, a smooth silicon dioxide surface is phobic to a hexane droplet in a water environment. The surface is inverted because hexane is less dense than water. For convenience, the hexane droplets in a water environment were dyed yellow and the water droplets in a hexane environment were dyed blue. By infusing the reentrant channels with either water or hexane (second and third images) the surface could be made either repellent or wetting to the hexane. Similarly, the same behavior could be achieved for water in a hexane environment (fourth and fifth images). Therefore, the same ability to tailor wetting behavior independent of intrinsic wettability also exists in liquid-liquid systems (Figure 23c). This flexibility in creating selective surfaces could be beneficial for many applications such as liquid separation[57], oil-spill remediation[115], and for the creation of lubricant infused surfaces[47,116].

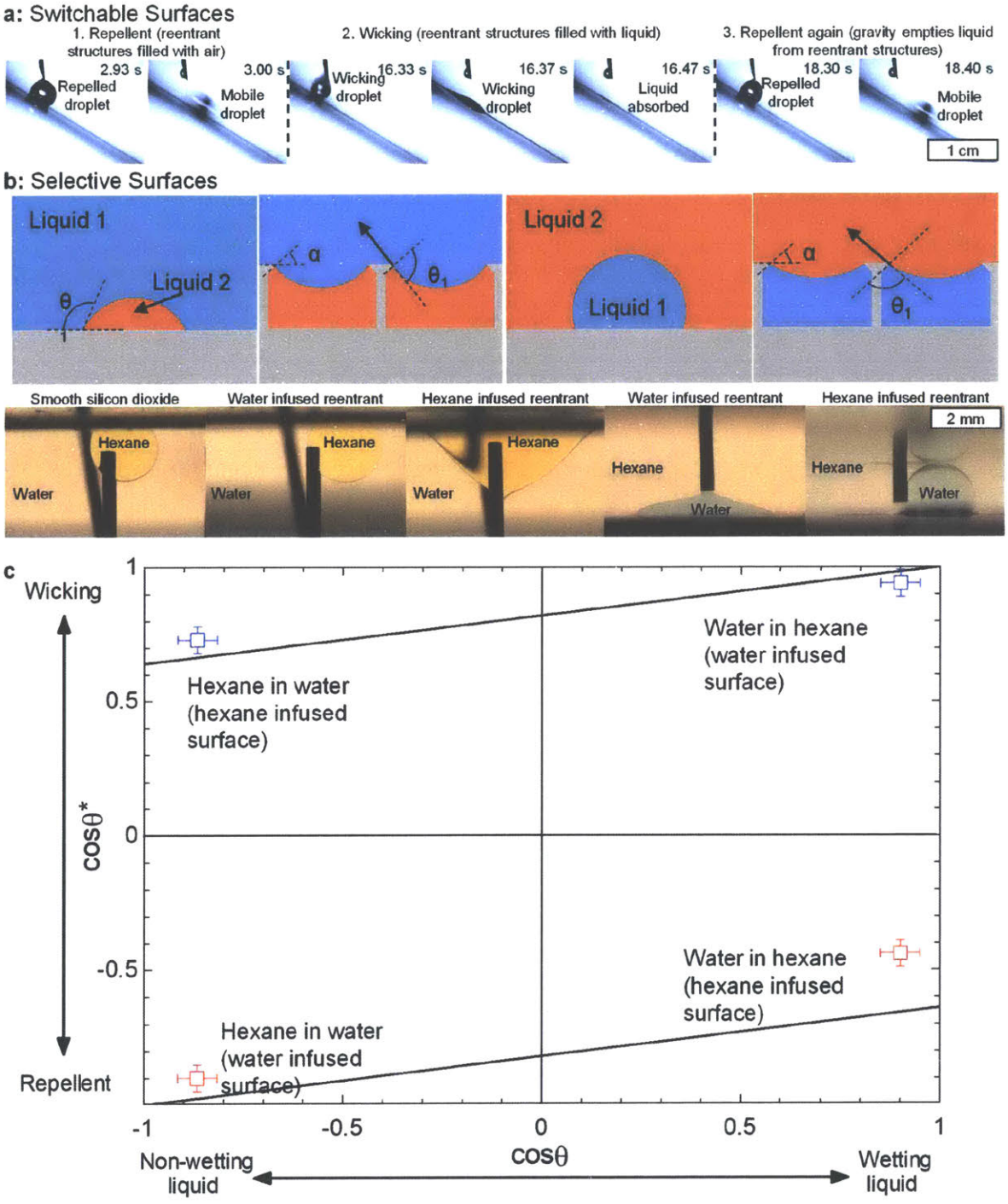

Figure 23: Further applications of omniphilic/omniphobic surfaces.

***a**, The surface can be switched between repelling and wicking. A tilted reentrant channel surface filled with air initially repelled liquid in the Cassie state. However, by pumping liquid into the reentrant channels a droplet placed on the surface was wicked into the channels. Finally, by removing the liquid in the channels (in this case achieved with gravity) the surface became repellent again. **b**, Wicking/repellency selectivity can be set by controlling initial wetting states. Contact line pinning at the reentrant feature allows a surface in contact with two liquids to be stable (or metastable) filled with either liquid as long as $\theta_1 + \alpha > 90°$ and $\theta_1 - \alpha < 90°$, where θ_1 is the contact angle liquid 1 makes with a flat surface in an environment of the second liquid. Therefore, by prefilling the surface with one liquid or the other, selective repellency or wicking of either liquid may be set arbitrarily. In the images, the surface was set to wick or repel both hexane and water in the presence of the other. **c**, Apparent advancing contact angle (cos θ*) on reentrant microstructures parallel to the channels for liquid/liquid systems with different intrinsic wettability (cos θ), where the advancing contact angle on a smooth surface is used for the intrinsic wettability. The same trends were seen as for liquid-air systems. Both wicking and repellency can be achieved regardless of the intrinsic contact angle. No low-surface energy coating was used in these tests, i.e., the surface was simply silicon and silicon dioxide.*

We have demonstrated that both omniphilicity and omniphobicity can be achieved with reentrant surface structuring, which enables rational control over wetting behavior on a surface independent of intrinsic wettability of the material/liquid combination used. Furthermore, functional surfaces such as switchable omniphilicity and omniphobicity, as well as selective wicking and repellency, can be achieved using this surface design. Although challenges remain in fabrication and mechanical durability of reentrant microstructures, reentrant microstructures promise to impact many high-performance technologies that utilize tailored wettability.

3.5 Methods

Fabrication of Surfaces

The fabrication procedure of both normal and reentrant channels is depicted in Figure 17a and b. Each step is described in further detail here.

Photoresist Exposure and Development (Figure 17a and b i)

A 2.5 μm layer of photoresist (Microposit S1822) was spin coated on polished silicon wafers that had a 1 μm thick silicon dioxide layer on the surface. The photoresist was exposed using an MLA150 Maskless Aligner. The resist was developed for 120 seconds in Microposit MF CD26 developer.

Reactive Ion Etch (Figure 17a and b ii)

The silicon dioxide was first etched using CF_4 (MPX/LPX RIE, STS). Then, the channels were etched in the silicon with deep reactive ion etching (Rapier DRIE, SPTS).

Oxide Removal (Figure 17a iii)

For normal channels, the silicon dioxide was removed by placing the samples in 7:1 buffered oxide etch solution for 10 minutes.

SF_6 Etch (Figure 17b iii)

An isotropic SF_6 etch (Rapier DRIE, SPTS) was used to remove silicon below the silicon dioxide to create the reentrant geometry.

C_4F_8 Deposition (Figure 17a and b iv)

A conformal, 60 nm thick hydrophobic polymer (C_4F_8) was deposited (Rapier DRIE, SPTS). This allowed a large range of intrinsic contact angles to be tested and also created surfaces with uniform and consistent wettability.

Contact Angle Measurements

A custom-built experimental setup was used to measure contact angle (Figure 24a). The air and liquid temperature remained close to the surrounding laboratory temperature. A syringe pump (Micro4, World Precision Instruments) was used to add and remove water from a droplet on the surface. Note that the liquid was added and removed slowly enough that there was no dynamic effect on the contact angle, i.e., the capillary number was small. A DSLR camera (EOS Rebel T3, Cannon) and macro lens were used to collect images of the droplet advancing on the surface. Lighting of the droplet was supplied with a light source (Intenselight C-HGFI, Nikon) and lens (C-HGFIB, Nikon). Contact angle was extracted from the images using ImageJ. For contact angle measurements of reentrant surfaces in the repellent state, the droplet was added to a dry surface, i.e., air within the surface structures. For the hemiwicking state, the droplet was added to a surface prefilled with the same liquid as that in the syringe.

Capillary Height Measurements

A custom-built experimental setup was used to measure the capillary height for each sample (Figure 24b). The samples were attached to a linear stage with a Vernier scale. This allowed the surfaces to be dipped into or withdrawn from a large pool of liquid. The Vernier scale (accurate to $1/100^{th}$ of an inch) was used to determine the capillary height. In order to test the repellent state of reentrant surfaces, the initially dry surface was lowered into the liquid. A camera recorded the surface as it was lowered into the liquid. When the maximum negative capillary height into the liquid was exceeded, liquid entered the structures. The height at which this occurred was recorded. Similarly, to test the hemiwicking state of reentrant surfaces, the

surfaces were prefilled with the liquid to be tested. The surface was then withdrawn from the pool of liquid. When the maximum positive capillary height of the liquid was exceeded, air entered the structures and the liquid receded. The height at which this occurred was recorded.

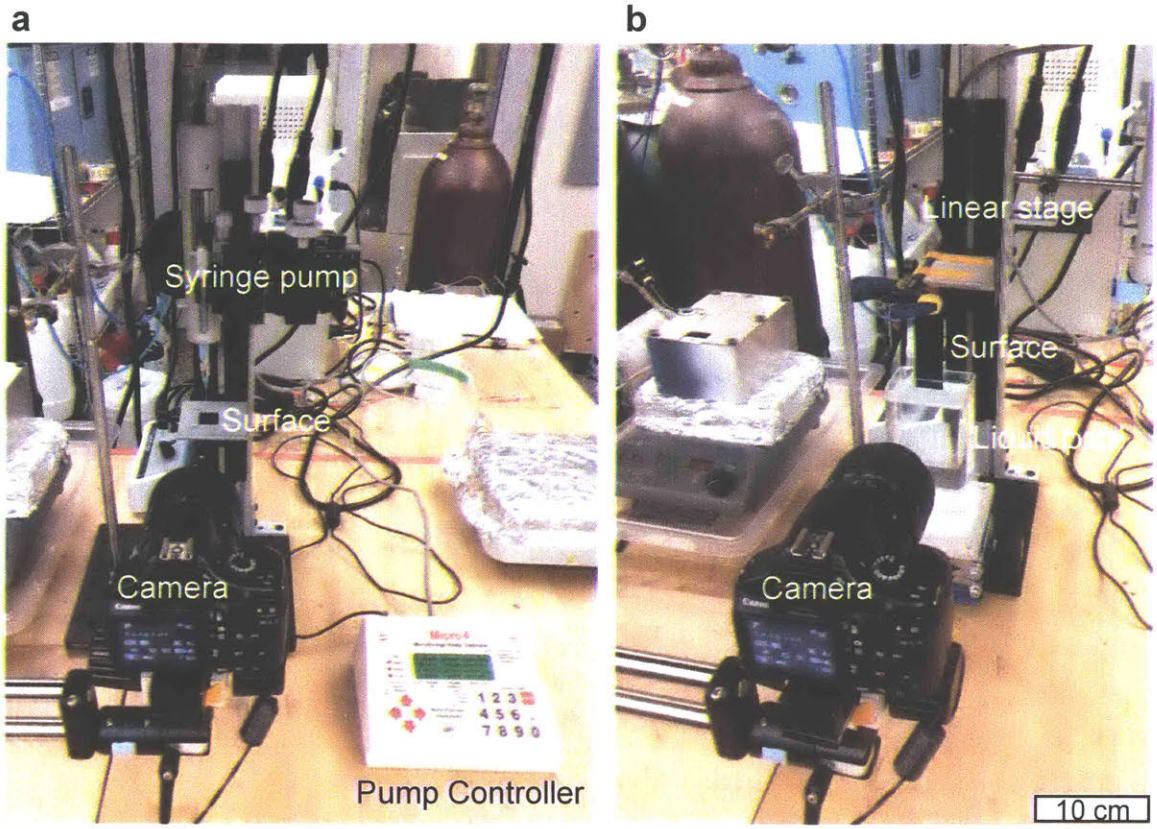

Figure 24: Experimental setups.

***a**, Image of the custom-built contact angle measurement setup. A syringe added and removed liquid from a droplet on the surface while a camera recorded the contact angle. A light source (not shown) provided illumination of the droplet. **b**, Image of the custom-built capillary height measurement setup. The sample was attached to a linear stage with a Vernier scale to allow accurate measurement of the capillary height. The sample was then raised out of or lowered into a pool of liquid and the corresponding capillary height measured.*

Prefilling Surface Structures

Prefilling the reentrant channels with liquid was achieved using a variety of methods. For naturally wicking liquids, the liquid was added to one end of the channels and in turn, filled the channels spontaneously. For ethanol/water mixtures that were not wicking, the channels were first filled with pure ethanol. Next, the ethanol filled sample was placed in a large container of

the ethanol/water mixture to be tested. The pure ethanol within the surface structures was allowed to diffuse into the mixture, thereby replacing the ethanol in the channels with the mixture. Note that the volume of ethanol in the channels was on the order of ten microliters, whereas the container was more than one thousand times this size. Therefore, this filling method did not affect the final concentration of the mixture. Samples were then removed from the mixture such that the channels remained filled to conduct contact angle or capillary height measurements. For mercury, prefilling was achieved by vacuum filling the reentrant microstructures. The surface was placed in a small chamber, the chamber was then evacuated of air to less than 10 Pa, after which the chamber was filled with mercury, thereby ensuring the reentrant structures were completely filled with this highly non-wetting liquid.

Selective Wicking and Repellency Experiments

The measurement was done with the same setup for the contact angle measurement. Two immiscible liquids, water and hexane, were used for testing. First, a drop of one of two liquids was placed on a flat surface while the entire surface was submerged in the other liquid to confirm the intrinsic contact angle, θ. Then, the selective wicking was achieved by infusing the same liquid as the droplet into the reentrant structures. On the other hand, the repellency was achieved by infusing the other liquid into the reentrant structures. In the case of testing the wettability of hexane within a water environment, due to the density difference of two liquids, the surface was flipped upside-down and a syringe was placed under the surface to add a hexane droplet.

Switching Between Wicking and Repelling Experiments

To demonstrate the ability to switch between states, the reentrant channels were tilted at an angle of 30°. The surface was initially dry. Therefore, when a syringe added a liquid mixture of 83% water and 17% ethanol to the surface, a droplet was formed in the Cassie state and thereby repelled. However, by adding the same liquid to the channels using a pump, a droplet added to the surface formed the hemiwicking state and was wicked into the surface structures. When enough liquid was added to the tilted surface, hydrostatic pressure from gravity caused the liquid within the structure to spontaneously dewet from the channel, thereby recovering the state filled with air. As such, the repellent Cassie state was recovered. This process was continuously repeated multiple times to highlight reversibility.

Uncertainty Propagation

This section presents the method used for uncertainty propagation of the experimental results. The method for determining uncertainty is described in NIST Technical Note 1297[117]. Individual measurements are assumed to be uncorrelated and random. Therefore, the uncertainty, U, in a calculated quantity, Y, is determined as

$$U = \sqrt{\sum_i \left(\frac{\partial Y}{\partial X_i}\right)^2 U_x^2} \tag{33}$$

where X is the measured variable, and U_x is the uncertainty in the measured variable. Table 6 summarizes the uncertainty associated with each experimental measurement that was then propagated according to Eq. 33 to determine uncertainty.

Table 6: Uncertainties of measurements.

Experimental Measurement	**Uncertainty**
Contact angle measurement (θ)	5°
Capillary height measurement (h)	1 mm
Ethanol/water mixture weight percent	± 2 %

4. Condensation-Resistant Omniphobic Surfaces

Omniphobic surfaces based on reentrant surface structures repel all liquids, regardless of the surface material, without requiring low-surface-energy coatings. While omniphobic surfaces have been designed and demonstrated, they can fail during condensation, a phenomenon ubiquitous in both nature and industrial applications. Specifically, as condensate nucleates within the reentrant geometry, omniphobicity is destroyed. Here, we show a nanostructured surface that can repel liquids even during condensation. This surface consists of isolated reentrant cavities with a pitch on the order of 100 nanometers to prevent droplets from nucleating and spreading within all structures. We developed a model to guide surface design, and subsequently fabricated and tested these surfaces with various liquids. We demonstrated repellency to various liquids up to 10 °C below the dew point and showed durability over three weeks. This work provides important insights for achieving robust, omniphobic surfaces.

4.1 Introduction

Surfaces that are repellent to various liquids during condensation have broad applications in anti-fouling,[46,118] chemical shielding,[113] heat transfer enhancement,[35,49] biomimetics,[47] drag reduction,[119] self-cleaning,[51] water purification,[48] icephobic surfaces,[120] and super-repellent surfaces.[121] Chemical modification of surfaces with low-surface-energy coatings has been used but is typically limited to high-surface-energy liquids, like water.[122] Furthermore, such modifications can degrade over time, where a robust solution - despite more than eight decades of work developing coatings of different types[20,24,47,89] - has yet to be found and widely implemented in applications where condensation occurs.[14,31,123] In contrast to low-surface-energy coatings, reentrant micro and nanostructures allow a surface to repel fluid,[61,124] and even exhibit omniphobicity,[52] without chemical modification. Such surfaces utilize geometry to create a local energy barrier for liquid propagation, thereby maintaining air pockets below the liquid on the surface, suspending the liquid on top of the structures in what is called the Cassie wetting state. Specifically, the three-phase contact line pins at the reentrant feature, which produces a surface tension force that prevents liquid from entering the structure. The development of numerous fabrication methods and geometries has enabled reentrant surfaces to repel many different liquids.[97,125-128] In the extreme case, this repellency is achieved using arbitrary materials.[52]

However, due to the fact that the surface material is often intrinsically wetting, reentrant surfaces fail when the liquid enters the microstructure and propagates. Therefore, in many cases, a single defect or transition to a local Wenzel state can cause the entire surface to lose its omniphobicity. This failure can result from multiple causes, for example: (i) exceeding the breakthrough pressure (the maximum sustainable liquid pressure) of the surface,[124,129] (ii) a

defect in the reentrant structure,[130,131] and (iii) condensation due to the presence of supersaturated vapor[45,52,132-135] or contact with a liquid that is hotter than the surface.[136,137]

Exceeding the breakthrough pressure (Figure 25a) occurs when the pressure of the liquid on the surface is great enough that liquid is pushed past the reentrant geometry. This may occur in multiple ways. A few examples are from a droplet impacting the surface with some velocity, a droplet becoming so small that the curvature of the droplet induces a large pressure (*i.e.*, pressure described by the Young-Laplace equation), or hydrostatic pressure (for example the pressure exerted on someone diving in the ocean). The breakthrough pressure, P, of a reentrant surface scales as $P \propto 2\gamma \sin\theta / l_{char}$ where γ is the liquid surface tension, θ is the contact angle the liquid makes with a flat surface of the same material as the reentrant geometry, and l_{char} is the characteristic length of the surface (where for an estimate, half of the pitch of the reentrant structure can be used). Due to the submicron pitch of the surfaces developed in this work, the breakthrough pressure is large. For water at 20 °C, the breakthrough pressure is expected to be approximately 334 kPa (which is equivalent to a spherical droplet of water with a radius of ~430 nm or 33 meters below the surface of the ocean).

Defects in the structures (Figure 25b) may occur during fabrication or due to physical damage of the surface. This failure mode may be overcome by creating a non-wicking structure so that a defect does not cause the entire surface to fail. Therefore, the surface designed in this work is robust to defects. In fact, a surface with a defect density of similar magnitude to the nucleation density observed in this work should still function.

Failure due to condensation (Figure 25c) occurs because the location of nucleating droplets is difficult to control and may happen anywhere on the surface. Therefore, droplets may condense and grow within the reentrant geometry, destroying the omniphobicity in a similar fashion to defects. Condensation occurs when the surface temperature is below the saturation point of the surrounding vapor, *i.e.*, surface subcooling. This subcool can occur if warm liquid comes in contact with a relatively colder surface. The warm liquid raises the saturation point locally, causing condensation to occur within the vicinity of the liquid in contact with the surface. The subcooling may also occur if the surface is colder than the saturation temperature of the surrounding vapor. In this case, condensation occurs everywhere on the surface, as opposed to only locally around liquid on the surface. Condensation may occur in many potential applications of omniphobic surfaces. A small number of examples for applications are given here.

Anti-fouling: A medical device inserted into the body, such as a catheter, may be initially colder than the body itself. This would induce condensation on the surface.

Heat transfer enhancement: Condensation heat transfer is commonly enhanced in the literature by promoting shedding of condensate *via* chemical modification of the condenser surface. This enables dropwise or jumping-droplet condensation. An omniphobic reentrant surface that is not condensation-resistant could not be used in this case.

Drag reduction: A ship with a drag reduction coating on its hull may pass through a region of relatively warmer water. This would induce condensation on the surface.

Self-cleaning: Dewing (condensation) often occurs on windows, solar panels, and other surfaces. A self-cleaning coating on these surfaces would need to be condensation-resistant to function properly.

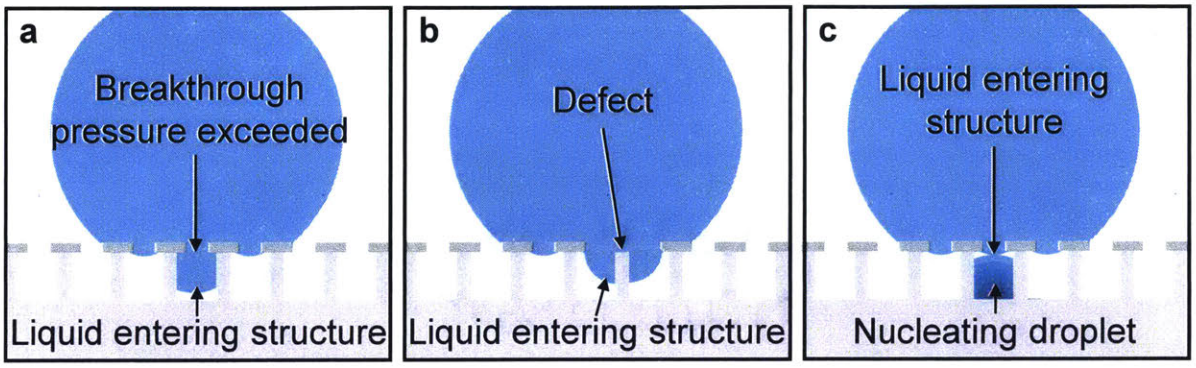

Figure 25: Failure modes of omniphobic reentrant surfaces.

Schematics showing failure modes of reentrant surfaces, including ***a****, exceeding the breakthrough pressure,* ***b****, a defect in the structure, and* ***c****, condensation from supersaturated vapor or relatively warm liquid on the surface.*

Rational design has been used to improve robustness for the first two failure modes, but a surface that adequately addresses all failure modes simultaneously had not yet been developed, greatly limiting application of omniphobic surfaces. Condensation-induced failure has been particularly challenging to address. When liquid is condensed on a reentrant pillar surface that is designed to repel impinging droplets, the repellency is lost (Figure 26a) due to nucleating droplets within the microstructure. As seen in the environmental scanning electron microscope (ESEM), when water condenses on the reentrant pillar surface (Figure 26b), nucleating droplets grow within the structures. The nucleating droplets merge with droplets suspended on the surface, providing a pathway for liquid on top of the microstructure to transition to the Wenzel state, as depicted in Figure 26c. As such, a typical reentrant surface that is considered super-repellent loses its fluid repellency when condensation occurs, as shown in Figure 26d.

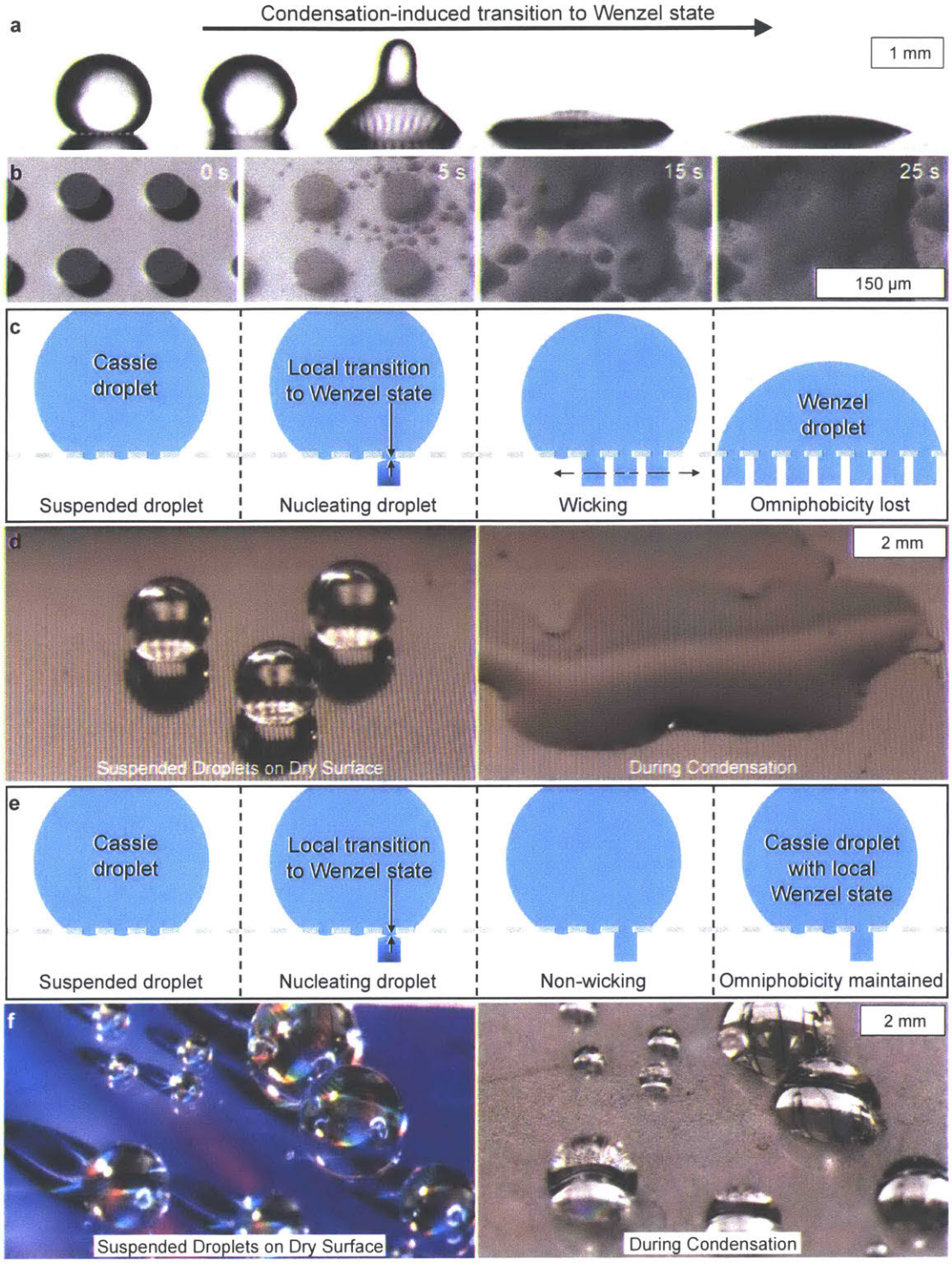

Figure 26: Preventing condensation induced failure of omniphobic surfaces.

***a**, Images of a suspended water droplet on a reentrant pillar surface as condensation began. The contact angle was high initially due to the surface maintaining a Cassie state with trapped air below the droplet. However, during condensation, the surface transitioned to a Wenzel state as nucleating droplets within the structure displaced the trapped air, destroying all repellency. **b**, Time-lapse ESEM images of condensation occurring on the reentrant pillar surface. Condensing droplets form within the microstructure, preventing air from being trapped and droplets in a Cassie state. **c**, Schematic showing a nucleating droplet growing within reentrant structures, causing the suspended droplet to transition to a Wenzel state. **d**, Water droplets placed on a reentrant pillar surface. All repellency was destroyed during condensation due to a transition to the Wenzel state. **e**, Schematic depicting a reentrant surface that prevents wicking of condensate between structures, thereby preserving the Cassie state locally for areas without nucleating droplets. f Water droplets placed on the non-wicking nanostructure developed in this work. The colors in the left image are caused by the periodic nanoscale reentrant features diffracting visible light. In contrast to the reentrant pillar surface, the contact angle of droplets placed on the surface was maintained during condensation as shown in the right image. Diffraction in the right image is not as strong as the left image due to the condensing droplets growing on the surface. The condensing droplets are just visible in the image, appearing as a light speckle on the otherwise shiny surface.*

In contrast, we developed a nanoscale, reentrant cavity surface to prevent nucleating droplets from spreading between structures and thereby preserving the trapped air in any cavity without a nucleating droplet (Figure 26e). As long as a nucleation site does not occur within all cavities (which is achieved by creating structures with characteristic spacing smaller than that of nucleating droplets), the repellency is retained. As such, the fabricated nanoscale reentrant cavity surface maintained its advantageous repellency during condensation of different fluids (Figure 26f). We demonstrated condensation-resistant repellency without a low-surface-energy coating for both water and ethylene glycol. Furthermore, additional benefits of our design are the robustness to large defect densities in the microstructure due to the non-wicking structures and the higher breakthrough pressure due to the nanoscale feature size.[124] Our proof-of-concept work shows the potential use of reentrant geometry to tailor wettability in the presence of condensation, which is necessary for the viability of omniphobic reentrant surfaces in various applications.

4.2 Model for Condensation-Resistant Surface

In order to properly design a condensation-resistant reentrant surface, we developed a model to capture the wetting behavior. Liquid on a reentrant surface forms a

composite interface of air, liquid, and solid material, where the apparent contact angle of liquids has been described by the Cassie-Baxter relation.[4] However, this relation is only valid when the entire surface is in the Cassie wetting state, which is not the case with condensation due to nucleating droplets causing a local transition to the Wenzel state. To design condensation-resistant reentrant surfaces, as well as interpret experimental contact angles of the fabricated surfaces, the effect of the fraction of the cavities beneath the suspended droplet in the "local" Wenzel and Cassie states (Figure S3) is considered. We derived a modified Cassie-Baxter relation for the apparent liquid contact angle with the surface, θ*. A droplet advancing on the reentrant cavity surface used in this study will interact with a composite interface that includes both local Cassie and local Wenzel states, depicted in Figure 27. We can consider the change in the Gibbs free energy, *dG*, of the system for a droplet displacement, *dm*:

$$\frac{dG}{dm} = (\gamma_{sl} - \gamma_{sv})r\phi + \gamma_{lv}\cos\theta^* + (1-\phi)X_{wenzel}\gamma_{lv} - (1-\phi)(1-X_{wenzel})\gamma_{lv} = 0 \quad (34)$$

where γ_{sl} is the solid liquid surface energy, γ_{sv} is the solid vapor surface energy, r is the wetted surface roughness factor, ϕ is the solid fraction of the surface ($\phi = 1 - \frac{(L-D)^2}{L^2}$ for a reentrant cavity surface), γ_{lv} is the liquid vapor surface energy, θ^* is the apparent contact angle of the droplet on the surface, and X_{wenzel} is the fraction of cells in the Wenzel state. The first term on the right-hand side represents the replacement of solid vapor interface with solid liquid interface. The second term represents the creation of liquid vapor interface. The third term represents the removal of liquid vapor interface in cells in the local Wenzel state, and the final term represents the creation of liquid vapor interface in cells in the local Cassie state. Using Young's equation:

$$\gamma_{sv} - \gamma_{sl} = \gamma_{lv}cos\theta \quad (35)$$

where θ is the Young's angle (contact angle of the liquid with a flat surface), a modified Cassie-Baxter equation is derived as:

$$\cos\theta^* = r\phi\cos\theta - (1-\phi)(1-X_{Wenzel}) + (1-\phi)X_{Wenzel} \quad (36)$$

However, a composite interface does not have a single apparent contact angle due to distortion of the three-phase contact line and variation in the surface solid fraction on the heterogeneous surface.[108,138,139] To address the discrepancy in values predicted by the Cassie-Baxter relation with those observed experimentally, the local solid fraction of the

solid-liquid interface at the three-phase contact line, f_{sl}, has been used.[97,109] With this modification, the advancing contact angle, θ_{adv}, of the surface is found to be:

$$\cos\theta_{adv} = r f_{sl}\cos\theta - (1 - f_{sl})(1 - X_{Wenzel}) + (1 - f_{sl})X_{Wenzel} \quad (37)$$

The receding contact angle, θ_{rec}, for the reentrant cavity surface is then:

$$\cos\theta_{rec} = r f_{sl}\cos\theta + (1 - f_{sl})(1 - X_{Wenzel}) + (1 - f_{sl})X_{Wenzel} \quad (38)$$

where f_{sl} is identical in the receding and advancing cases. $f_{sl} = 1 - \sqrt{1 - \phi}$ and $\phi = 1 - (L - D)^2/L^2$ for a reentrant cavity surface.[97] The difference between the advancing and receding angle is known as contact angle hysteresis (CAH) and influences shedding of droplets on the surface. CAH on omniphobic surfaces with interconnected features such as reentrant cavity surfaces tends to be higher than that on surfaces with disconnected features like reentrant pillar surfaces.[97] CAH hysteresis can be reduced using hierarchical textures.[140] Therefore, a hierarchical combination of the reentrant cavity nanostructures developed in this work on disconnected, pillar-like roughness would lead to a super-repellent surface.

In this work, we focus on the advancing contact angle due to its dependence on X_{Wenzel}, as opposed to the receding angle which is independent of X_{Wenzel} for reentrant cavity surfaces. Therefore, based on Equation 37, the maximum advancing contact angle occurs when $X_{Wenzel} = 0$ and reduces as X_{Wenzel} increases. In order for the reentrant surface to maintain its advantageous wetting properties, X_{Wenzel} must remain small, *i.e.*, no nucleating droplet within most cavities.

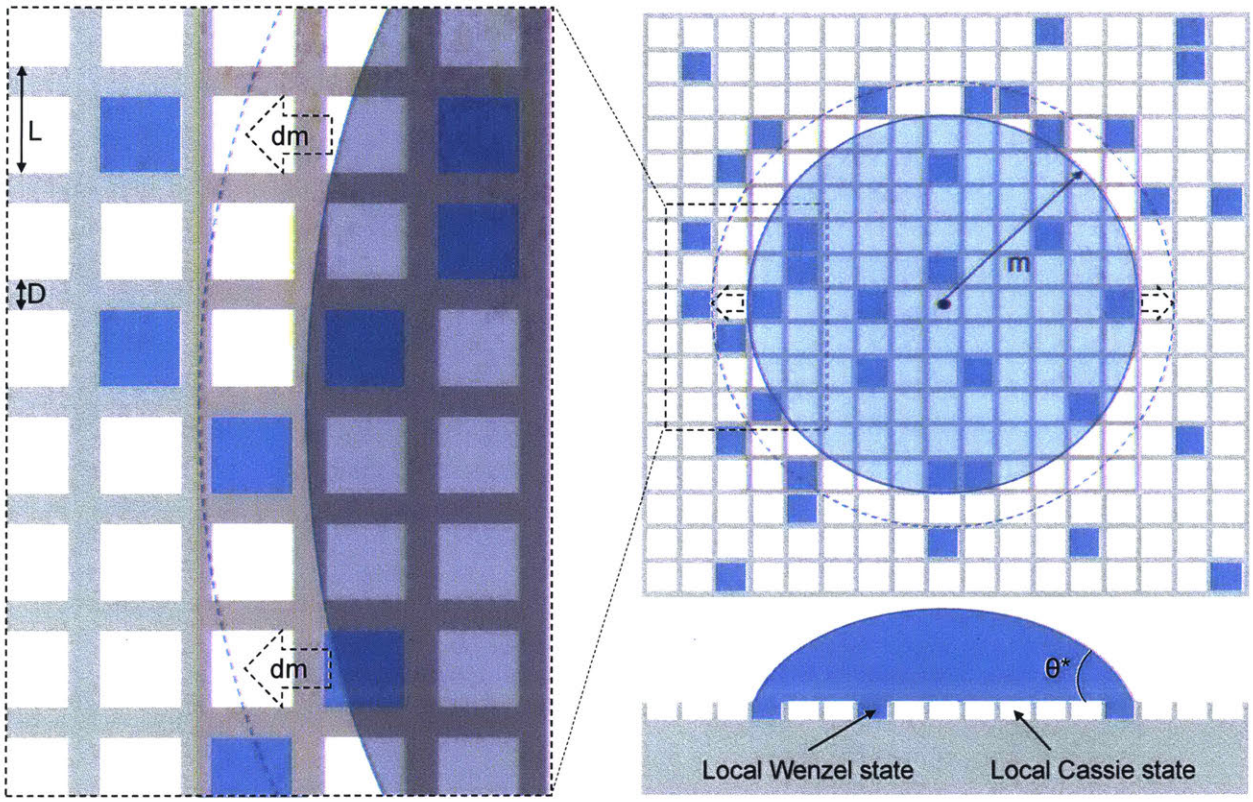

Figure 27: Schematic of droplet on reentrant cavity surface with condensation.

Schematic of an advancing droplet on top of a reentrant cavity surface with a portion of cells filled by condensate and therefore in the local Wenzel state for the advancing droplet. dm is the displacement of the three-phase contact line, θ is the apparent contact angle of the surface, L is the structure pitch, and D is the width of the reentrant cap.*

4.3 Design of Condensation-Resistant Reentrant Geometry

We achieved a low X_{Wenzel} by fulfilling two requirements. First, the structure needs to prevent local transitions to the Wenzel state from propagating. A simple reentrant structure that can achieve this non-wicking behavior is a reentrant cavity structure, depicted in Figure 28a (L is the pitch, H is the height, t is the thickness of the reentrant cap, α is the sidewall angle, and D is the width of the cap). The grid of

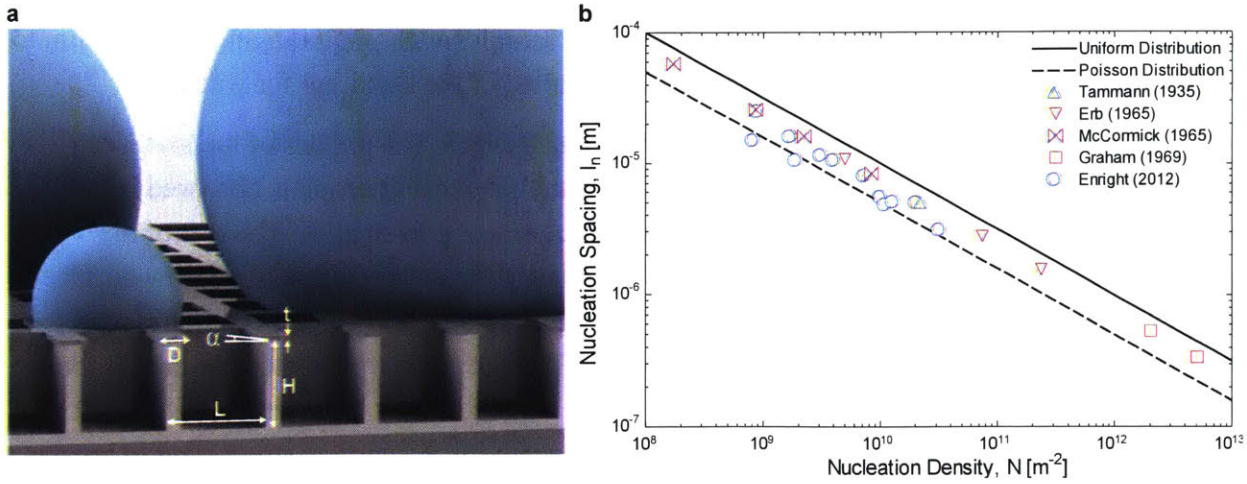

Figure 28: Design of condensation-resistant omniphobic surfaces.

a*, Schematic of a reentrant cavity surface with interconnected features that prevent liquid (blue) flow between cavities. D is the width of the reentrant cap, H is the height of the structures, α is the angle the reentrant geometry forms with the plane parallel to the surface, t is the thickness of the overhang cap, and L is the pitch of the structures.* ***b****, Typical nucleation densities observed in the literature, and nucleation site spacing. The Poisson distribution (dashed line with* $l_n = (1/2)N^{-0.5}$*) and a uniform distribution (solid line with* $l_n = N^{-0.5}$*) are shown. If no nucleation spacing was reported in the reference, the average of the uniform and Poisson distribution was plotted.*

interconnected features prevents propagation of liquid in the local Wenzel state and hence, it maintains a local Cassie state in the cavities without nucleating droplets. Therefore, the second requirement for the surface to maintain its wetting properties with condensation is that the surface needs to prevent droplets from nucleating within the majority of cavities, such that they remain filled with air.

When nucleation occurs on a surface, a finite number of discrete droplets form. Numerous studies have measured nucleation density (number of droplets per area), N, of water on surfaces during condensation.[36,91,141-144] Typical nucleation densities correspond to an average nucleation spacing (distance between droplets), l_n, ranging from hundreds of nanometers to tens of microns (Figure 28b). Nucleation density depends on factors such as surface temperature relative to the vapor temperature, liquid surface tension and contact angle, and roughness.[144] Therefore, the condensing fluid and specific reentrant geometry (roughness) could influence the nucleation density, although similar trends are expected to those reported for water and rough surfaces. In order to prevent nucleation from occurring within every cavity of the surface, the

pitch of the structure should be less than the nucleation spacing. Therefore, for the condensation-resistant reentrant surfaces in this work, we fabricated samples with pitch ranging from 0.5 μm to 108 μm, spanning the range of nucleation spacing reported in the literature for water.

The various geometric parameters are shown in Table 7. The pitches of the surfaces were determined based on typical nucleation spacing between condensing droplets observed in literature, and range from larger-than-typical nucleation spacing to smaller. The rest of the geometry was set to ensure a robust reentrant surface that may repel water without low-surface-energy coatings.[124] The reentrant cap width, *D*, relative to pitch determines the solid fraction and local solid fraction of the surface. Generally, the smaller the cap width the more of the composite interface will be in the Cassie state. For this work, the cap width was kept between 1/4 and 1/2 of the pitch so that enough of the surface was in a Cassie state for the surface structuring to greatly modify wetting behavior compared to a flat surface. Cap thickness, *t*, determines the roughness, *r*, of the surface. A low roughness is desirable. Therefore, cap thickness was kept much smaller than the feature pitch. The height of the structures was set large enough such that the meniscus of the droplet on the surface was unable to contact the bottom surface below the structures, which would cause the surface to transition to a Wenzel state. Other parameters of the fabricated surfaces important for calculating the expected contact angles and fraction of cells in the Wenzel state are shown in Table 8.

Table 7: Geometry of fabricated reentrant samples.

Sample	Geometry Style	Pitch, L [μm]	Cap width, D [μm]	Cap thickness, t [μm]	Structure height, H [μm]	Reentrance angle, α [deg]
1	Cavity	0.5	0.25	0.035	0.5	0
2	Cavity	12	3	0.1	12	0
3	Cavity	36	9	0.1	36	0
4	Cavity	108	27	0.1	36	0
5	Pillar	108	27	0.1	36	0

Table 8: Geometric parameters and expected contact angles of fabricated reentrant samples.

Sample	Roughness, r [-]	Solid fraction, Φ [-]	Local areal fraction, f_{sl} [-]	Maximum expected advancing contact angle, $\theta_{adv,max}$ [deg]	Minimum expected advancing contact angle, $\theta_{adv,min}$ [deg]
1	1.039	0.82	0.58	85.51	24.01
2	1.057	0.4375	0.25	122.20	17.04
3	1.019	0.4375	0.25	122.80	17.21
4	1.006	0.4375	0.25	123.00	17.27
5	1.015	0.05	0.22	180	0

4.4 Fabrication of Reentrant Cavities of Varied Pitch

We fabricated samples with large pitch ($L > 10$ μm) using standard methods previously developed for omniphobic reentrant surfaces (the features were defined using photolithography and the reentrant overhang created with an isotropic XeF_2 silicon etch). The smallest pitch surface ($L = 0.5$ μm), however, could not be fabricated using traditional methods due to limitations in the smallest feature size as well as the lack of precise control over the isotropic etch depth that ultimately creates the reentrant feature. Instead, we developed a method as depicted in Figure 29a for nanoscale pitch reentrant features. We used interference lithography[145] to pattern the photoresist (Figure 29a i), reactive ion etching to transfer the pattern into the silicon nitride and silicon (Figure 29a ii), and oxidation of silicon (Figure 29a iii) with subsequent removal of the oxide using hydrofluoric acid (Figure 29a iv) to create the nanoscale reentrant geometry. Silicon nitride was chosen as the material for the reentrant cap due

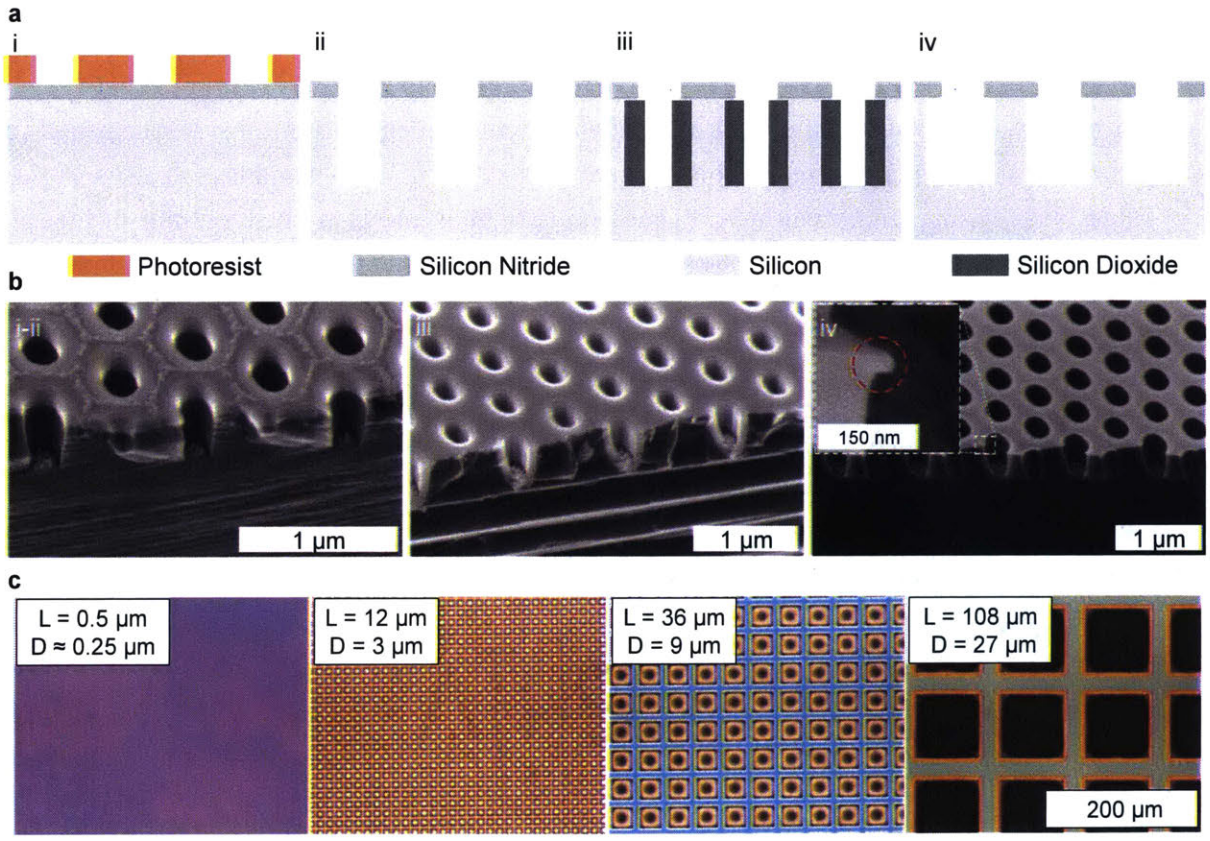

Figure 29: Fabrication of condensation-resistant omniphobic surfaces.

a*, Schematic of fabrication steps for nanoscale pitch reentrant cavities: i) spin, expose, and develop photoresist; ii) reactive ion etch and photoresist removal iii) silicon dioxide growth; iv) removal of silicon dioxide with hydrofluoric acid. (For larger pitch samples, xenon difluoride*

was used to etch silicon to create the reentrant overhang, replacing steps iii and iv.) ***b****, SEM images of the L = 0.5 μm pitch sample at different steps of fabrication. The left image is between steps i and ii before the photoresist was removed, the middle image is after step iii, and the right image is after step iv. The inset shows a magnified view of a single reentrant feature coated with palladium to increase image quality. The reentrant geometry, a 30 nm overhang made of 35 nm thick silicon nitride, is circled in red.* ***c****, Top-down microscope images of all fabricated reentrant cavity surfaces with pitch, L, spanning three orders of magnitude.*

to its use in local oxidation of silicon (LOCOS), and its etch selectivity over silicon dioxide in hydrofluoric acid.[146] The scanning electron microscope (SEM) images in Figure 29b show cleaved sections of the 0.5 μm pitch sample in between steps i and ii (photoresist still on the surface), after step iii, and after step iv. Top-down microscope images of all the fabricated reentrant cavity surfaces are shown in Figure 29c (all images are at the same magnification).

4.5 Contact Angle During Condensation

The advancing contact angles on the reentrant cavity surfaces with pitch between 0.5 μm and 108 μm, along with a reentrant pillar surface with a pitch of 108 μm were measured for various liquids with a custom-built experimental setup (Figure 30a and liquids used listed in Table 9). A syringe pump was used to add and remove liquid from the reentrant surface at various temperatures, T_{surf}, while a camera recorded the contact angle after two minutes at T_{surf}. The ambient temperature (T_{amb}), liquid droplet temperature ($T_{sat,drop}$), and ambient saturation temperature ($T_{sat,air}$) were set inside an environmental enclosure. Representative results for tests with water are shown in Figure 30b (where T_{amb} = 23 °C, $T_{sat,drop}$ = 23 °C, and $T_{sat,air}$ = 12.5 °C). The reentrant pillar surface was initially repellent but failed when the surface temperature decreased below $T_{sat,drop}$ due to condensation caused by the relatively warmer droplet water increasing the saturation temperature locally around the droplet. The reentrant cavity surfaces, however, maintained wetting properties below $T_{sat,drop}$ as well as below $T_{sat,air}$. Large pitch samples (L > 10 μm) failed at small subcooling ($\Delta T = T_{surf} - T_{sat,air}$) once the surface dropped below $T_{sat,air}$, because nucleation occurred within the majority of the cavities on the surface. Smaller pitch (L < 1 μm) samples retained properties until lower temperatures due to a larger fraction of the cavities remaining in the local Cassie state, as expected. Note that a nanocavity surface without reentrance does not exhibit the same behavior (Figure 31).

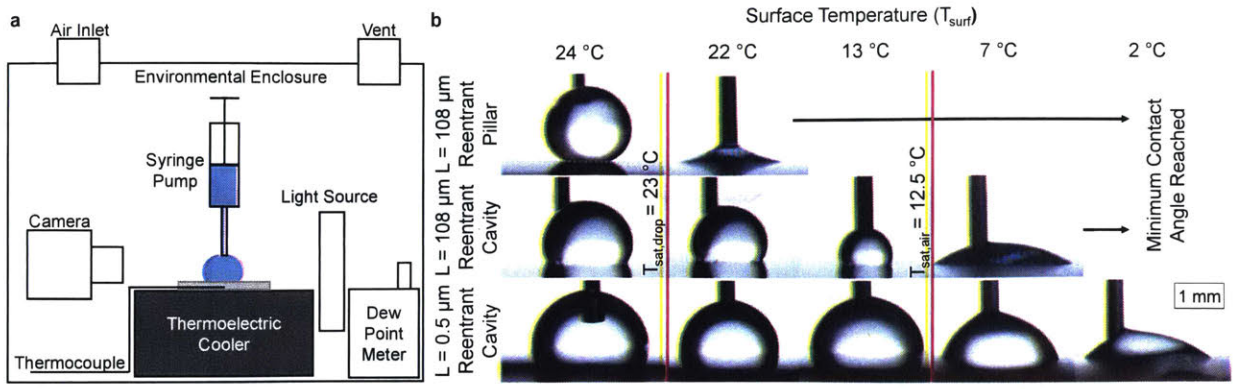

Figure 30: Contact angle measurement with condensation.

***a**, Schematic of experimental setup for measuring contact angle. The samples were mounted on a thermoelectric stage that controls the sample temperature. A syringe added and removed liquid from a droplet on the surface while a camera recorded the droplet growth. **b**, Images of advancing contact angle of water with varied temperature for L=0.5 µm and L=108 µm. The advancing contact angle of the smaller pitch sample (L=0.5 µm) was retained to lower temperatures and still had not reached its minimum expected value of 24 degrees at a temperature more than 10 °C below the saturation temperature of the air.*

Table 9: Young's angle on liquids on silicon nitride.

Young's angle (contact angle on a flat surface) for fluids tested in this work on a flat silicon nitride surface with and without a low-surface-energy coating. The coating used in this work was trichloro(1,1,2,2-perfluorooctyl)silane (TFTS). Because doubly reentrant geometry was not used, a perfectly wetting fluid on silicon nitride cannot be repelled.

Fluid	Surface	Young's Angle [deg]
Water	Silicon Nitride	36
Ethylene Glycol	Silicon Nitride	38
Ethanol	Silicon Nitride	0
Ethanol	TFTS Silicon Nitride	42

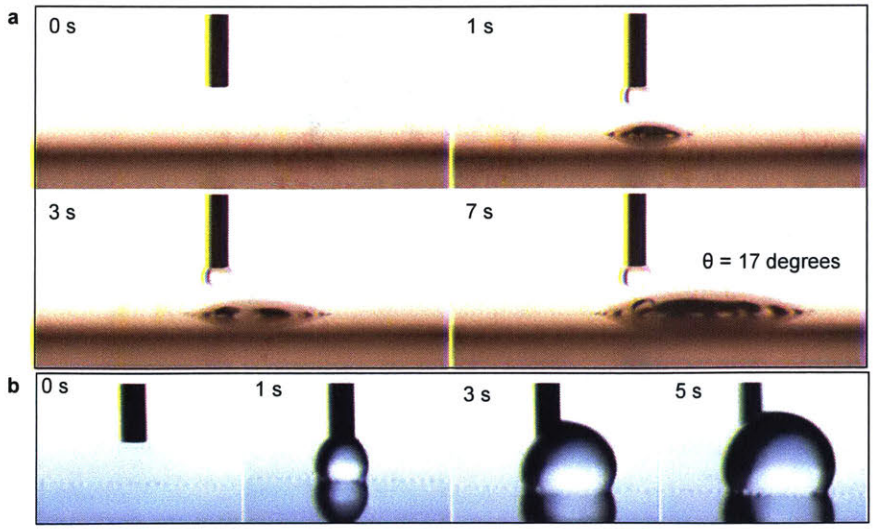

Figure 31: Wetting behavior on cavity surfaces with and without reentrance.

***a**, Time-lapse images of the advancing contact angle of water on a cavity surface with pitch of 108 μm; however, the surface does not have reentrance. Therefore, all cavities are in the local Wenzel state and the observed contact angle is near the minimum expected value predicted by equation S4. This behavior has also been observed on nanocavity surfaces without reentrance.[147] **b**, In contrast, a 108 μm cavity surface with reentrance exhibits an advancing contact angle near the maximum expected value predicted by equation s4 because the cavities are in the local Cassie state.*

4.6 Retention of Wetting Properties During Condensation

The contact angle measurements were normalized as $(\theta_{adv} - \theta_{min})/(\theta_{max} - \theta_{min})$, and are shown as a function of subcooling in Figure 32a for water. The modified Cassie-Baxter relation (eq. 2) was used to predict the maximum and minimum expected contact angles, θ_{max} and θ_{min}, of the surfaces for the normalization. The maximum corresponds to a surface entirely in the Cassie state, whereas the minimum corresponds to the entire surface in the Wenzel state. The reentrant pillar surface (purple vertical bowtie) did not have a contact angle starting at the theoretical maximum contact angle of 180 degrees, as expected, due to external energy input such as laboratory vibrations causing suspended droplets to partially relax.[97] When T_{surf} was set below $T_{sat,drop}$, the advancing contact angle of the reentrant pillar surface dropped to the minimum expected value. The reentrant cavity surfaces, however, maintained the original contact angle below $T_{sat,drop}$, due to their non-wicking behavior even though the relatively warmer droplet induced condensation in the microstructure below the droplet. Once the surface temperature decreased below $T_{sat,air}$, condensation due to surface subcooling began. The contact

angle of large pitch samples (green horizontal bowtie) reduced to the minimum expected value within 2 °C of subcooling. At smaller pitches, the contact angle was maintained to subcooling of a greater magnitude. In fact, the smallest pitch sample (L = 0.5 μm, black square) had not reached the minimum expected value at a subcooling beyond 10 °C (freezing of water on the surface prevented further subcooling). This result suggests a fraction of the cavities remained in the local Cassie state which is a vast improvement over both reentrant pillar surfaces and larger pitch reentrant cavity surfaces. Once a cavity transitioned from the local Cassie to the local Wenzel state, however, it could only be reversed by drying the surface. Point 1 (filled black square) in Figure 32a was measured immediately after the lowest subcooling of sample L = 0.5 μm without drying in between. Thus, the advancing contact angle remained low. The measurement indicated by point 2 was conducted after the condensate had evaporated and the original contact angle of the sample was recovered.

To support the claim that nucleation did not occur within all cavities, experiments were conducted in an ESEM to visualize droplet nucleation and growth (Figure 32b). Tests were conducted in a pure water vapor environment (saturation temperature of 12 °C) with low surface subcooling (~0.1 °C). The L = 12 μm pitch reentrant cavity surface was used because the microstructures were easily visible in the ESEM and the surface maintained its contact angle better than larger pitch surfaces (Figure 32a). The spacing between nucleating droplets was larger than the structure pitch as nucleation occurred on the surface (Figure 33). Therefore, as the droplets grew, a high advancing contact angle was maintained due to the local Cassie state of the surrounding cavities.

The fraction of cavities that had nucleation sites and were therefore in the local Wenzel state, X_{Wenzel}, was determined based on experimental data and the modified Cassie-Baxter relation (Figure 32c). As expected, the reentrant pillar surface transitioned completely to the Wenzel state immediately after any condensation occurred on the surface due to the ability of a single nucleation site to cause the entire surface to manifest in the Wenzel state; whereas the reentrant cavity surfaces prevented liquid spreading and did not fail due to a small number of nucleation sites. However, because large pitch structures were larger than the typical nucleation spacing, the surfaces transitioned completely to the Wenzel state once the surface dropped below $T_{sat,air}$, which induced condensation in the majority of the cavities on the surface. As pitch was reduced, the fraction of the surface in the local Wenzel state was reduced for a given subcooling, leading to enhanced retention of wetting properties.

Our results highlight the ability of non-wicking nanoscale reentrant features to maintain wetting properties during condensation, and as such the viability of such structures to tailor wettability in many applications. Tests were done without any chemical modification of the

surface, *i.e.*, no low-surface-energy coating and intrinsically wetting materials. Therefore, the geometry presented in this work represents a potential alternative to low-surface-energy coatings. Because the wetting properties are achieved *via* geometry rather than material choice, surfaces that use more robust materials for the micro/nanostructures (such as the silicon nitride used in this work) may be created, aiding the transition to realistic applications.[148] This was demonstrated in Figure 32d by condensing water on a surface continuously (ΔT = -2.5 °C, $T_{sat,air}$ = 12.5 °C) for three weeks and

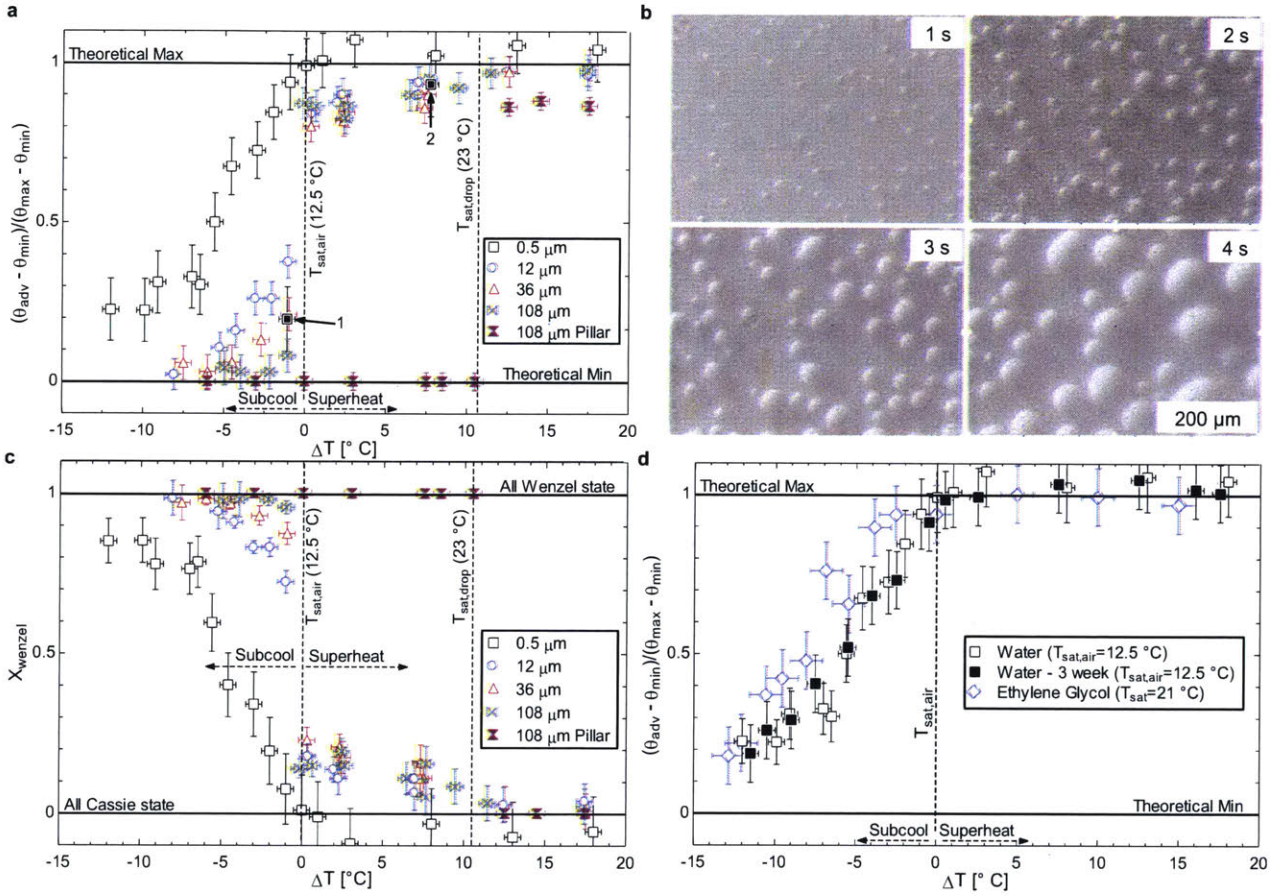

Figure 32: Retention of wetting behavior during condensation.

***a**, Normalized advancing contact angle of the different pitch surfaces for various surface temperatures relative to the saturation temperature of the air ($\Delta T = T_{surf} - T_{sat,air}$). As subcooling increased the advancing contact angle of all samples decreased. The smaller the pitch of the structures, the greater the retention of wetting properties with subcooling. Point 1 was measured immediately after the lowest subcooling of sample L = 0.5 µm without drying in between. Point 2 was measured after point 1, after the condensate had evaporated. This*

observation highlights that the wetting properties were only recoverable by removing liquid from filled cavities. ***b****, Time-lapse of environmental scanning electron microscope images during condensation on a surface in saturated water vapor with L = 12 μm and ~0.1 °C subcooling. Nucleation sites did not occur in all cavities of the surface, allowing the advancing contact angle to be maintained.* ***c****, Fraction of filled cavities,* X_{Wenzel}*, for different subcooling. The smaller pitch samples maintained a larger advancing contact angle at a given subcooling due to a larger percentage of cavities remaining unfilled with condensate. The reentrant pillar surface failed immediately due to the ability of liquid to spread between structures.* ***d****, Normalized advancing contact angle on the 0.5 μm pitch sample with ethylene glycol (blue diamonds), a common heat transfer fluid, with a saturation temperature of 21 °C compared to water for a just fabricated surface (open black squares) and a surface after three weeks of continuous testing (filled black squares). No degradation in performance was observed.*

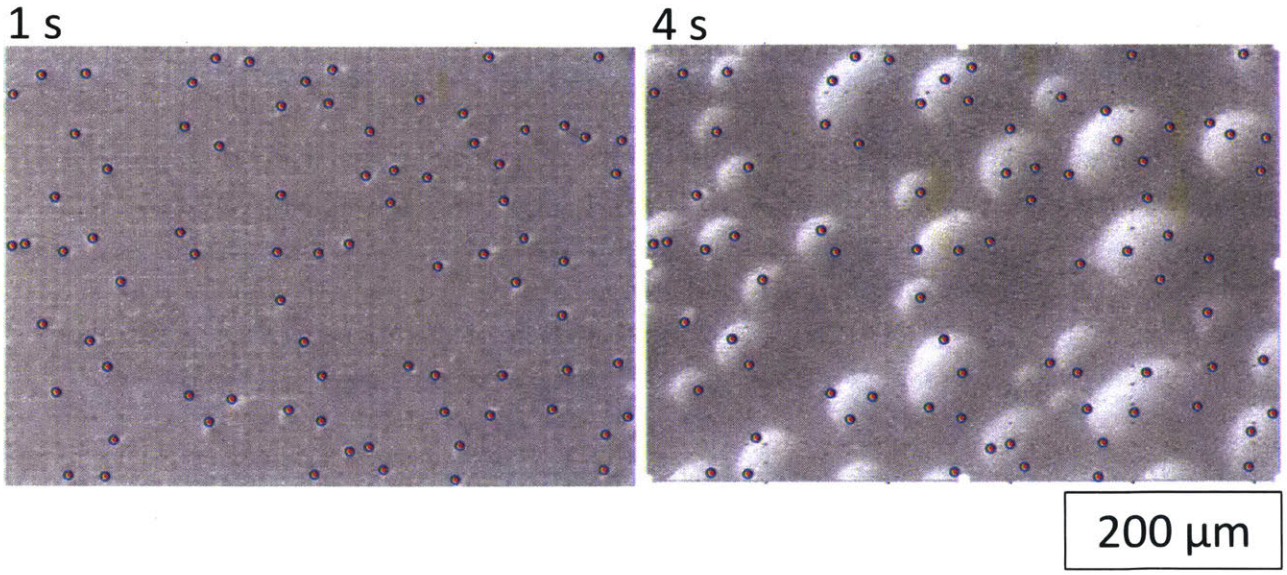

Figure 33: Nucleation on reentrant cavity surfaces.

Time-lapse of environmental scanning electron microscope images during condensation on a surface in saturated water vapor with L = 12 μm and ≈ 0.1 °C subcooling. Nucleation sites (red circles) did not occur in all cavities of the surface. A nucleation spacing of ≈ 54 μm was calculated based on the images. This is significantly larger than the pitch, allowing the advancing contact angle to be maintained.

remeasuring the contact angle during condensation (filled black squares). No degradation in performance was observed relative to a newly fabricated surface (open black squares), indicating the surface nanostructure was unaltered.

Furthermore, because reentrant surfaces have been developed to repel many fluids, the surface fabricated in this work presents an opportunity to also tailor the wettability during condensation of fluids other than water. The 0.5 μm pitch reentrant cavity surface successfully maintained wetting properties for ethylene glycol, a common heat transfer fluid, during condensation (blue diamonds in Figure 32d). The contact angle measurements lead to a number of important considerations.

The decrease in contact angle with increasing subcool of the surface is associated with an increase in nucleation density on the surface. Nucleation density is also affected by other factors, such as the liquid being condensed, condensation conditions such as saturation temperature, the surface geometry, and the surface chemistry. Figure 34 shows normalized contact angle measurements varying some of these parameters. First, water was condensed at a higher saturation temperature (21 °C), which has been observed to increase the nucleation density for a given subcool. Accordingly, the contact angle of the surface was also less for the same subcool.

Second, because reentrant surfaces have been developed to repel many fluids, the surface structure fabricated herein presents an opportunity to also tailor the wettability during condensation of fluids other than water. The 0.5 μm reentrant cavity surface successfully maintained wetting properties for ethylene glycol, a common heat transfer fluid, during condensation at $T_{sat,air} = 21$ °C. Performance is comparable or slightly better than water, likely due to the low vapor pressure of ethylene glycol causing nucleation density to be low.

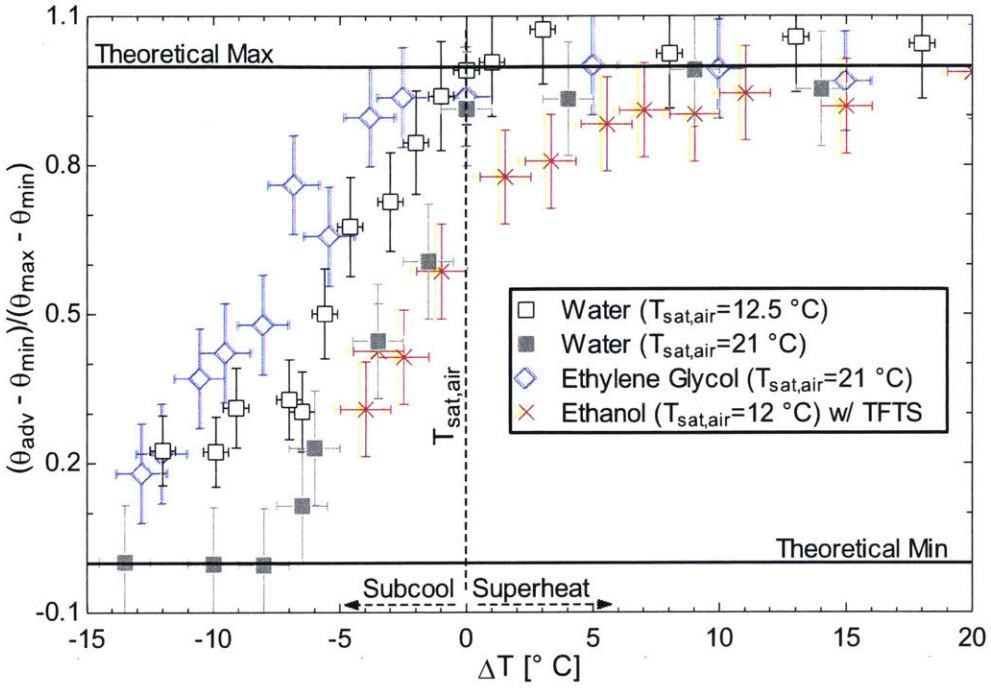

Figure 34: Advancing contact angle measurements on reentrant cavity surface during condensation of a variety of fluids.

Normalized advancing contact angle on the 0.5 μm pitch sample with a variety of fluids and water at different saturation conditions. Ethylene glycol, a common heat transfer fluid, and water at different saturation temperatures were successfully repelled without a low surface energy coating. Because the geometry developed here is not doubly reentrant, ethanol (which is perfectly wetting on silicon nitride) was only repelled with a low-surface-energy coating to increase the intrinsic contact angle with silicon nitride. This could be also be addressed by using different geometry (i.e., doubly reentrant) or a different material with a non-zero contact angle with the liquid.

However, because the current design is not doubly reentrant, it is not able to repel perfectly wetting fluids. Ethanol, a low surface tension fluid, has a Young's angle of 0 degrees on silicon nitride and wets the cavities of the surface. These very low surface tension fluids may be successfully repelled with the addition of a low-surface-energy-coating, through a different material choice, or through the creation of doubly reentrant geometry. To demonstrate this, the sample was coated with trichloro(1,1,2,2-perfluorooctyl)silane, which increased the Young's angle for ethanol to 42 degrees, after which similar behavior was observed and wetting properties maintained during condensation. The slight reduction in performance compared to

water may be a result of the lower surface tension and higher vapor pressure of ethanol, which would increase nucleation density.

Finally, it is important to note that the structure and fabrication method developed in this work is not necessarily ideal for all applications. The solid fraction of the 0.5 μm pitch surface was too high to achieve very large contact angles as seen in Figure 30b, but this behavior can be addressed with improved fabrication. For example, the theoretical minimum solid fraction for the hexagonal array of circular cavities used in this work is ≈ 0.1, which would produce an advancing contact angle of 156 degrees based on Equation 2. Furthermore, reentrant cavity surfaces tend to have higher contact angle hysteresis (CAH) than reentrant pillar surfaces, which prevents shedding of droplets. CAH may be reduced by using hierarchical structures that incorporate the nanoscale reentrant cavities in this work onto existing surface roughness, such as pillars (Supplementary Material, S3).

4.7 Conclusions and Outlook

We demonstrated a reentrant cavity surface design that achieves and maintains fluid repellency during condensation without the need for low-surface-energy coatings. This is important for the viability of omniphobic surface modification in light of the prevalence of condensation in nature and industrial applications. For example, dew commonly forms on surfaces that would benefit from self-cleaning coatings, and condensation is an important process for electricity production. The surface demonstrated in this work incorporated cavities to prevent wicking between structures and defined pitches smaller than typical nucleation densities to prevent nucleation within all structures. Furthermore, due to the specific nanoscale geometry used, the surface was robust in terms of breakthrough pressure and defects. Modeling of the expected contact angle suggests the surface retained fluid repellency during condensation due to a fraction of the surface structures remaining in the Cassie state. This retention of repellency is important for use of reentrant surfaces in applications including anti-fouling, heat transfer enhancement, drag reduction, and self-cleaning surfaces.

4.8 Methods

Contact Angle Measurements

The custom-built experimental setup depicted in Figure 30a was used to measure contact angle. The humidity of the enclosure was set using a humidifier (Ultrasonic Humidifier, Taotronics) and measured with a humidity meter (RH820U, Omega). The dew point of liquids other than water were measured with a chilled mirror dew point meter. The air and liquid temperature within the enclosure remained close to the surrounding laboratory temperature and pressure. A small fan within the enclosure gently circulated air to maintain uniform conditions. The sample was attached to a thermoelectric temperature-controlled stage (CP-031, TE

Technology, Inc.) and controller (TC-720, TE Technology, Inc.) using conductive copper tape. A thermocouple (K-type, Omega) on the stage next to the surface monitored temperature. A syringe pump (Micro4, World Precision Instruments) was used to add and remove water from a droplet on the surface. A DSLR camera (EOS Rebel T3, Cannon) and macro lens were used to collect images of the droplet advancing on the surface. Lighting of the droplet was supplied with a collimated light source (Intenselight C-HGFI, Nikon) and lens (C-HGFIB, Nikon). Contact angle was extracted from the images using ImageJ. The surface was maintained at temperature for two minutes before conducting the contact angle tests. The surface was dried between tests unless stated otherwise.

Photoresist Exposure and Development

We used interference lithography to define the etch mask for samples with a pitch of 0.5 μm. An 80 nm thick silicon dioxide layer was deposited with electron beam evaporation. Then, a 180 nm thick antireflection coating (Brewer Xhri-16) was spin coated on the surface, followed by a 190 °C bake on a hotplate for 60 s. A 440 nm of photoresist (NR7-250) was subsequently spin coated and baked at 150 °C for 60 s. A custom built Lloyd's mirror was then used to expose a hexagonal array with pitch of 0.5 μm. This was developed for 90 s in a 3:1 mixture of RD6 and deionized water. For all of the larger pitch samples, a 2 μm layer of photoresist (Microposit S1813) was used and exposed using an MLA150 Maskless Aligner. The resist was developed for 90 s in CD26.

Reactive Ion Etch

Samples with a pitch of 0.5 μm were first etched (790 series, Plasmatherm) in helium and oxygen to remove the antireflection coating. Next, CF4 was used to etch the silicon dioxide and silicon nitride. Finally, HBr was used to etch the silicon. All larger pitch samples were first etched using CF4 (MPX/LPX RIE, STS) to remove the silicon nitride. Then, the silicon was etched with deep reactive ion etching (Rapier DRIE, SPTS).

Oxide Growth and Etch

Samples with a pitch of 0.5 μm used oxidation of silicon and subsequent removal of the oxide with hydrofluoric acid (HF) to create the reentrant feature. Silicon was oxidized *via* dry oxidation at 1000 °C. This silicon was then removed with HF.

Xenon Difluoride Etch

All larger pitch samples used a xenon difluoride etch (ES-2000XM, SE Tech) to create the reentrant geometry. Chamber etch pressure was set to 2800 mTorr, with a 60 second hold time, and 20 second evacuation time for each etch cycle. Cycles were repeated until the desired etch depth was reached and varied between samples of different pitch.

Surface Cleaning

After fabrication, all samples had the photoresist removed *via* a combination of solvent cleaning and plasma cleaning, were RCA cleaned, and were finally oxygen plasma cleaned for 30 minutes (Expanded Plasma Cleaner PDC-001, Harrick Plasma). Samples were tested after roughly one day in the laboratory environment after plasma cleaning.

Environmental Scanning Electron Microscopy

Environmental scanning electron microscope images were taken in a Zeiss EVO 50 scanning electron microscope. Samples were mounted on a temperature-controlled stage. After evacuating the ESEM, pure water vapor was added and the saturation temperature was set at 12 °C. The surface temperature was set slightly below the saturation temperature *via* the temperature-controlled stage and images were taken with a secondary electron detector. The accelerating voltage (EHT) was 15 kV and probe current was 2 nA.

Uncertainty Propagation

This section presents the method used for uncertainty propagation of the experimental results. The method for determining uncertainty is described in NIST Technical Note 1297.[117] Individual measurements are assumed to be uncorrelated and random. Therefore, the uncertainty, U, in a calculated quantity, Y, is determined as

$$U = \sqrt{\sum_i \left(\frac{\partial Y}{\partial X_i}\right)^2 U_x^2} \tag{39}$$

where X is the measured variable, and U_x is the uncertainty in the measured variable. Table 10 summarizes the uncertainty associated with each experimental measurement that was then propagated according to Equation 39 to determine uncertainty.

Table 10: Uncertainties corresponding to experimental measurements.

Experimental Measurement	Uncertainty
Ambient Temperature (T_{amb})	0.5 °C
Saturated vapor temperature for water ($T_{sat,air}$)	0.5 °C
Saturated vapor temperature for fluids other than water ($T_{sat,air}$)	1 °C
Contact angle measurement (θ)	5 degrees

5. Fabrication of Doubly Reentrant Surfaces via Stress-induced Bending

We developed omniphobic, doubly reentrant surfaces fabricated with a simple method suitable for use with traditional microfabrication processes. Intrinsic stresses in deposited layers of silicon nitride induced bending of a singly reentrant microstructure, creating the doubly reentrant geometry. Due to the use of standard microfabrication processes, this approach may be extended to a variety of materials and feature sizes, increasing the viability of applying omniphobic doubly reentrant structures for use in areas such as superomniphobicity, anti-corrosion, heat transfer enhancement, and drag reduction.

5.1 Introduction

Doubly reentrant microstructures enable omniphobic surfaces that repel even completely wetting (i.e., low surface tension) fluids without the use of low-surface-energy coatings [52,149,150]. Such surfaces have use in a range of applications such as anti-fouling[46], chemical shielding [113], heat transfer enhancement [49], drag reduction [50], self-cleaning [51], and water purification [48]. In order to achieve omniphobicity, reentrant microstructures with characteristic length smaller than the liquids capillary length are required [52]. The level of reentrance necessary depends on the fluid's intrinsic contact angle, θ, with the surface material (Figure 35). The black arrow in the figure represents the contact line force. In order for liquid to be repelled, a component of the contact line force must act in the vertical direction. Therefore, a regular microstructure without reentrance only repels liquids with $\theta > 90\ °$. This large intrinsic contact angle is not possible for many liquids on solid surfaces or requires chemical modification for many others. Adding reentrant geometry can reduce the necessary contact angle to below 90 °. However, for a small θ, the vertical component of the contact line force is also small, making it difficult to repel highly wetting liquids. Therefore, to repel all liquids, including those with a small contact angle, a large degree of reentrance is required (i.e., doubly reentrant), which has been difficult to fabricate at the necessary characteristic length scales (100s of microns or smaller). Due to these difficulties, the fabrication of doubly reentrant surfaces has been limited in materials used, i.e., specialized polymers [149], or required complex fabrication techniques, i.e., high temperature

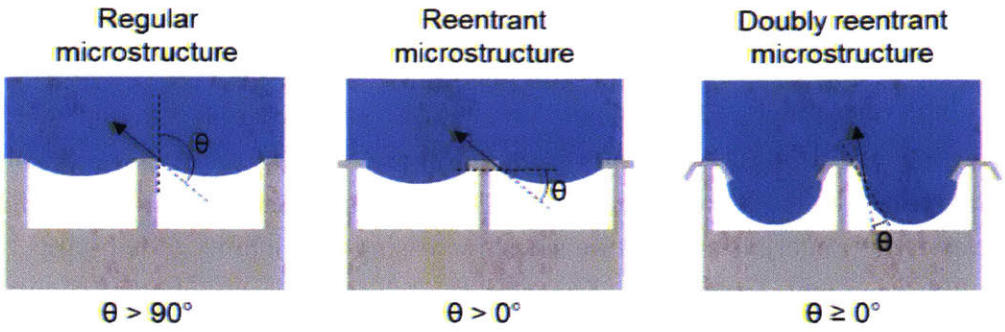

Figure 35: Reentrant structures for omniphobic surfaces.

Types of microstructures along with corresponding intrinsic contact angle, θ, for which the structure can practically repel liquid. The black arrow represents the contact line force that prevents liquid from entering the structure, which must act in the vertical direction in order to repel the liquid. To successfully repel liquids with low contact angle, doubly reentrant structures are necessary.

oxidation of silicon (not suitable for other materials) and multiple etch steps [52].

In this work, we developed a simple fabrication method using traditional microfabrication processes and demonstrated omniphobicity of the surface. The method relies on intrinsic stresses of deposited materials to induce bending of singly reentrant structures to create doubly reentrant geometry. Because this fabrication technique is based on singly reentrant surfaces, for which robust, scalable processes are already well-developed [61,97,124], it enables simple fabrication of doubly reentrant structures for a wide variety of materials.

5.2 Design

The level of double reentrance, α, influences the component of contact line force that acts in the vertical direction, F_y, which prevents liquid from entering the structures and maintains omniphobicity. Figure 36 shows the vertical component of F, for different θ and α, normalized by the theoretical maximum that occurs when the force is completely vertical, $F_{y,max}$, and is defined as:

$$F_{norm} = \frac{F_y}{F_{y,max}} = \frac{P\gamma \sin(\theta + \alpha)}{P\gamma} \tag{40}$$

where P is the length of the contact line (determined by microstructure geometry), and γ is the surface tension of the liquid. If the sum of θ and α is greater than 90 °, then $F_{norm} = 1$ due to the fact that a maximum occurs in F_y for a contact angle below the intrinsic value, which is still a stable state. This is why the curves for different θ reach a stable value of 1 with increasing α.

This figure highlights a number of key points. First, in order to produce adequate repellency of fluids with $\theta = 0\ °$, α must be larger than 0. Second, the repellency force increases with α, which creates a more

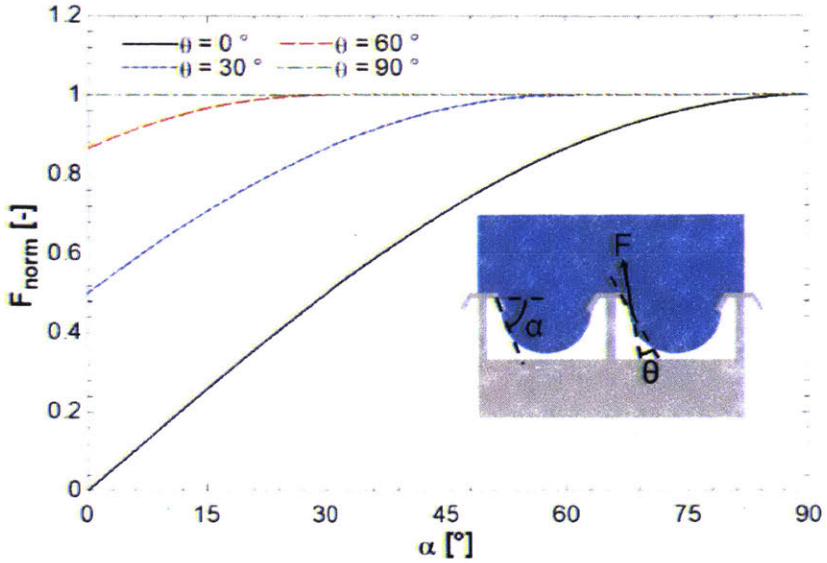

Figure 36: Enhanced repellency with double reentrance.

The normalized vertical component of the contact line force for different contact angle, θ, and level of reentrance, α. For a perfectly wetting liquid, α must be greater than 0 ° for the surface to have repellency. The maximum is reached when θ + α = 90 °.

robust omniphobicity, but reaches its maximum value when $\theta + \alpha = 90\ °$. We note that though the maximum repellency is reached at $\theta + \alpha = 90\ °$, a lesser value of α may still produce adequate repellency.

5.3 Fabrication

Figure 37 shows our fabrication process. Thin films of silicon nitride with intrinsic stresses were deposited on the polished silicon wafer with an STS PECVD system, which allowed stresses in the deposited material to be controlled (i). Next, features were defined with photolithography (ii). A 2.5 μm thick layer of Microposit S1823 was spin coated on the wafer and exposed using an MLA150 Maskless Aligner. The resist was developed in CD-26 for 90 seconds. Structures were then etched with DRIE (iii). An STS ICP RIE was used to etch the silicon nitride layers. Subsequently, an SPTS Rapier DRIE was used to etch the underlying silicon. Finally, an isotropic silicon etch was used to undercut the thin films of silicon nitride (iv). Both XeF_2 and SF_6 were successfully used for the isotropic etch due to the etch selectivity between silicon nitride and silicon. Due to the intrinsic stresses in the nitride films, tunable

bending (based on film thickness, stress, and undercut distance) occurred and formed the doubly reentrant surface.

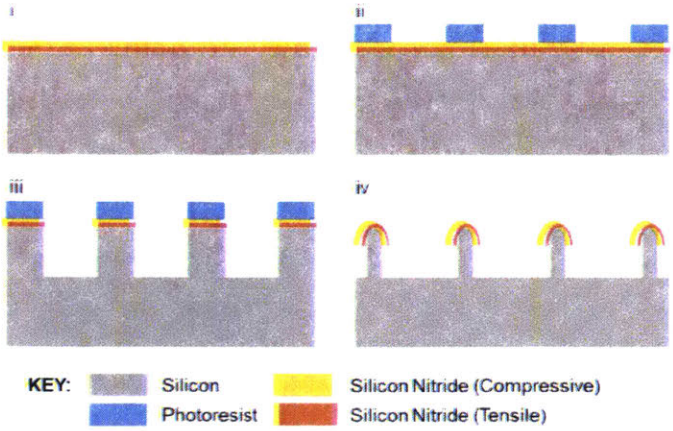

Figure 37: Fabrication of doubly reentrant structures via stress induced bending.

Fabrication method of doubly reentrant structures. i: Deposition of films with tensile and compressive stress. Silicon nitride was deposited with PECVD in this study. The film stresses induce bending in the final fabrication step to create the doubly reentrant geometry. Stresses and film thicknesses were chosen based on modeling of the bending ii: Etch mask defined using standard photolithography. iii: Deep reactive ion etch (DRIE) of structures. iv: Isotropic silicon etch with SF6 in the DRIE to create doubly reentrant feature due to stress induced bending.

Figure 38a shows a cross-section SEM of a fabricated doubly reentrant stripe-textured hoodoo (type of reentrant surface with parallel lines as features) surface with $\alpha = 62$ °. The bottom film of silicon nitride was 100 nm thick and low stress (less than 50 MPa), while the upper layer was 100 nm and had compressive stress (763 MPa measured using an FLX-2320 S), which induced the bending. Finite element analysis was used to choose the necessary film thicknesses, stresses, and geometry (Figure 38b) to achieve a high level of double reentrance, and showed reasonable agreement with fabricated surfaces. For stresses achievable in PECVD silicon nitride, this required the length, L, of the undercut to be between 10 and 100 times larger than the combined thickness of the deposited films. This ratio between film thicknesses and undercut length is a key parameter and will vary depending on material choice.

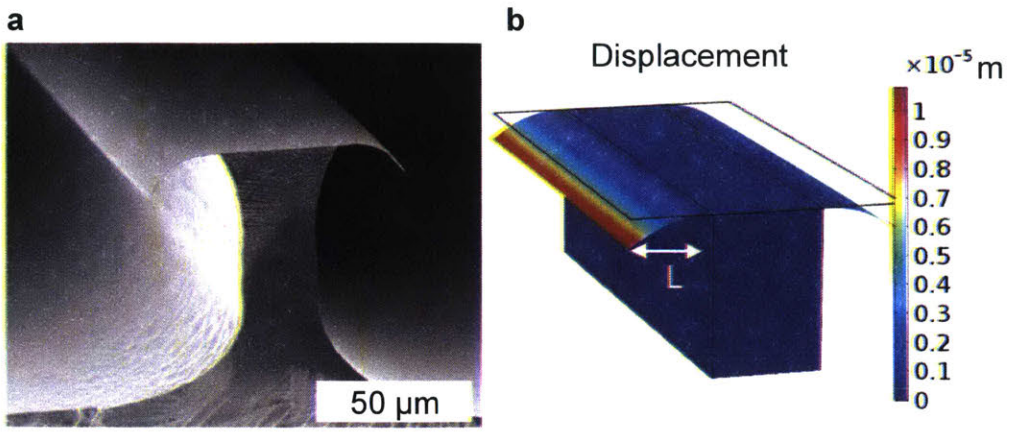

Figure 38: Fabricated surfaces and COMSOL prediction of bending.

***a**, Cross-section SEM of the fabricated doubly reentrant (α = 62 °) stripe-textured hoodoo surface. **b**, COMSOL model used to predict surface bending based on stresses and film thicknesses. This model determined the necessary stresses and thicknesses to realize a doubly reentrant surface with significant bending. For silicon nitride, this required the ratio of the length of the feature undercut, L, to the combined film thicknesses to be between 10 and 100, where 100 is shown in this figure.*

5.4 Contact Angle Measurement

We characterized the apparent advancing and receding contact angle of the fabricated surface for a variety of liquids using the experimental setup depicted in Figure 39. A syringe was used to add and remove liquid from a droplet on the surface. A collimated light source behind the droplet illuminated it while a DSLR camera recorded video as the droplet grew and shrunk. The video was then used to extract the advancing and receding contact angles in ImageJ.

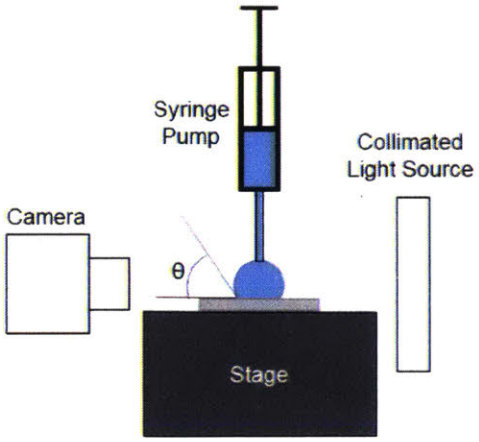

Figure 39: Contact angle measurement setup.

Schematic of experimental setup for characterizing contact angle. A syringe is used to add and remove liquid from a droplet on the surface, creating an advancing and receding contact line, respectively.

Images of the apparent advancing contact angle of both water, with a surface tension of 72.8 mN/m and FC 40, a common refrigerant with a very low surface tension of 16 mN/m, are shown in Figure 40. Due to the double reentrant structures and surface omniphobicity, both fluids were repelled regardless of the liquid surface tension.

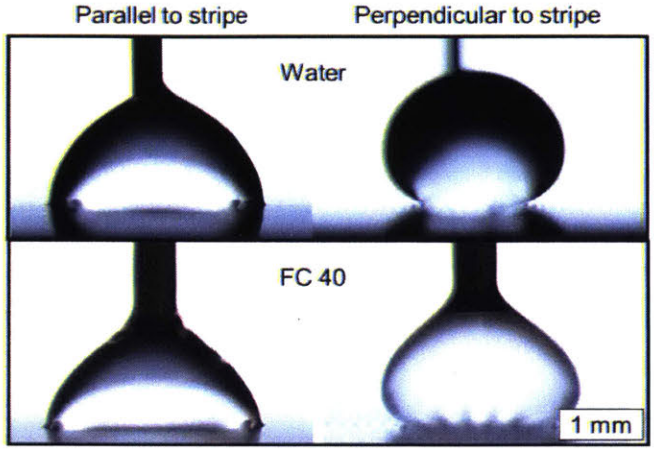

Figure 40: Omniphobicity via stress induced bending.

Images of advancing contact angle on the stripe-textured hoodoo surface, both parallel and perpendicular to the stripe for both water and FC 40. Both fluids were repelled due to the surface omniphobicity.

Advancing and receding contact angle measurements were conducted for liquids with a wide range of surface tensions (FC-40, ethanol, isopropanol, ethylene glycol, and water) in Figure 41. The observed contact angles agree well with theoretical values [97]. For the stripe-textured hoodoo surfaces the advancing contact angle perpendicular to the stripes, $\theta_{adv,perpendicular}$, is given by:

$$\cos\theta_{adv,perpendicular} = -1 \tag{41}$$

which gives an expected value of 180 °. The observed values are slightly lower due to vibrations in the laboratory causing the droplets to partially relax. The advancing contact angle parallel to the stripes, $\theta_{adv,parallel}$, is given by:

$$\cos\theta_{adv,parallel} = r\phi\cos\theta - (1-\phi) \quad (42)$$

where r is the roughness of the wetted solid (taken as 1 in this work due to the thin nitride films), and ϕ is the local areal solid fraction of the advancing droplet, 0.5 for the surface demonstrated here. This gives a predicted value of 90 °, similar to the experimentally observed values. Finally, the receding contact angle in both the parallel and perpendicular directions, θ_{rec}, is given by:

$$\cos\theta_{rec} = r\phi\cos\theta - (1-\phi) \quad (43)$$

For the stripe-textured surface used here the predicted receding angle is the same as the advancing angle parallel to the stripes, leading to a low contact angle hysteresis, which is necessary for liquid shedding. Furthermore, due to the doubly reentrant geometry the fluid properties do not appear in equations 41 through 43. Therefore, measured contact angles in Figure 41 are independent of the liquid contacting the surface, which agrees well with observed values. The advancing contact angles on a flat silicon nitride surface are also shown. Despite the nearly perfectly wetting liquids used, they were still successfully repelled.

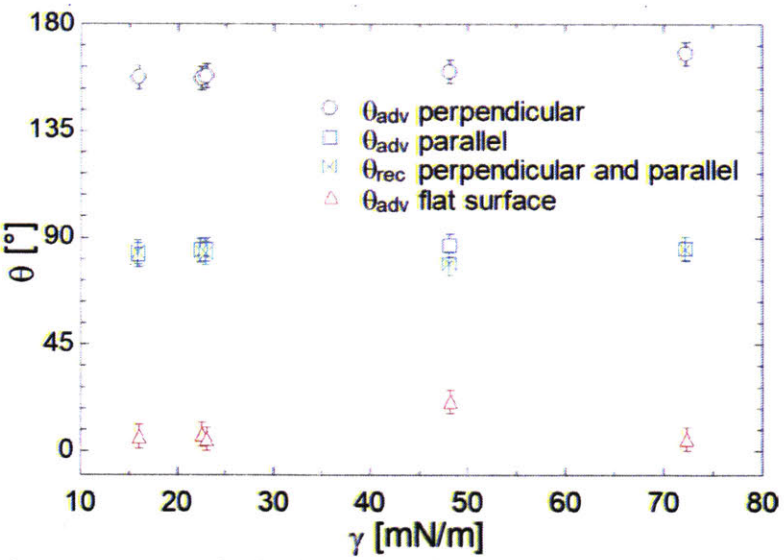

Figure 41: Advancing contact angle for liquids with varied surface energy.

Apparent advancing and receding contact angle of liquids with different surface tension, γ, both parallel and perpendicular to the stripe. Receding angle was the same in both directions. Advancing contact angle on a flat silicon nitride surface is also shown. All fluids were repelled, highlighting the omniphobicity, which can only be achieved with doubly reentrant geometry.

We are currently working to demonstrate different material sets and types of reentrant geometry (other than stripe-textured). Though silicon nitride was used in this work, other

materials also have controllable stresses (including metals, oxides, nitrides, and polymers) and are potential material choices. Table 11 lists a variety of materials and residual stresses observed in literature after growth/deposition with different techniques such as chemical vapor deposition (CVD), plasma-enhanced chemical vapor deposition (PECVD), magnetron sputtering, spin coating, and atomic layer deposition (ALD). Although this incomplete list represents candidate materials, further research should be done to determine necessary deposition parameters, how stresses in the films may evolve with time, as well as what α may be achieved. Furthermore, in order to fabricate the reentrant geometry, etch selectivity between the deposited material and the underlying substrate is necessary, which may limit material choices.

Table 11: Materials and intrinsic stresses.

Possible materials, deposition techniques, and residual stresses reported in the literature. A negative stress is compressive.

Material	**Deposition Technique**	**Residual Stress [MPa]**	**Reference**
Silicon nitride	PECVD	300 to -600	151
Metals	Sputtering	1000 to -2000	152
Parylene	CVD	50 to 20	153
Polyimide	Spin coat	30	154
Aluminum Oxide	ALD	500 to 200	155

5.5 Conclusions and Outlook

This fabrication procedure simplifies the ability to create doubly reentrant surfaces. Stress induced bending of singly reentrant geometry into doubly reentrant geometry was achieved by relying on intrinsic stresses of deposited silicon nitride films. Finite element analysis (FEA) was used to predict the necessary stresses, film thicknesses, and undercut length, L, to achieve a high level of reentrance. A stripe-textured hoodoo surface was fabricated and good agreement was observed with the FEA model. Due to the high level of reentrance achieved ($\alpha = 62$ °), the fabricated surface was able to repel all tested liquids with surface tension ranging from 16 to 72.8 mN/m, including liquids with very small intrinsic contact angle on silicon nitride. Furthermore, the observed contact angles matched well with predicted values based on previously developed models. Due to the use of standard microfabrication processes, the process developed here expands the potential materials sets, and widens the potential application of doubly reentrant omniphobic surfaces.

6. Nonuniform Pillar Arrays for Enhanced Wicking

Micro and nanostructured surfaces are commonly used to enhance fluid supply in thermal management, e.g., in thin film evaporation, flow boiling, and pool boiling. Capillary wicking within the structures passively supplies liquid to the evaporating interface where phase change occurs. In this work, we explored enhanced wicking for thin film evaporation in nonuniform structures by varying the geometry of a wicking pillar array in the direction of fluid propagation. Specifically, pillar pitch and diameter were varied along the wick in order to enhance performance (as opposed to uniform wicks used in previous studies). Constraints on the pitch and diameter were used in order to both ensure a feasible wick design that satisfied the criteria for imbibition and the validity of the used permeability relation. The nonuniform pillar array allowed the pressure drop to be minimized at each location by determining the best combination of pitch and diameter based on the relative liquid pressure at that location, leading to an increased dry-out heat flux. For example, an optimized uniform pillar array with a wicking length of 5 mm and a pillar height of 25 μm (diameter of 10 μm and pitch of 30 μm) had a dry-out heat flux of 61 W/cm^2, whereas the nonuniform array designed in this work had a dry-out heat flux of 172 W/cm^2. This modelling work demonstrates the potential of variable permeability wicking structures for enhanced thermal management systems, and shows that dry-out heat flux can be increased nearly 3x compared to uniform structures.

6.1 Introduction

Capillary-driven flow in porous media has broad applications in microfluidics [63] such as in lab-on-a-chip [64], electro-chromatography [65], resin molding [66], biomedical devices [67], and thermal management [68-70]. In particular, wicking in micro/nano scale wicks has emerged as a promising method to enhance thermal management techniques such as thin film evaporation [43,71-73], pool boiling [74,75], and flow boiling [76-78]. In these thermal management schemes, cooling is achieved via liquid-vapor phase change which takes advantage of the large latent heat of evaporation. Once liquid to be evaporated can no longer be adequately supplied the cooling scheme fails, which happens at the dry-out heat flux in thin film evaporation or the critical heat flux (CHF) in boiling. To prevent dry-out and CHF, micro/nanostructures have been introduced to the surface. Wicking due to the capillary pressure produced by the surface structuring provides passive supply of liquid to be evaporated, as seen in Figure 42a for thin film evaporation. How well the surface wicks liquid has been shown to determine the heat transfer enhancement for both thin film evaporation and boiling [43,72,75,79]. Therefore, a variety of wicks have been tested, with features ranging from nanoscale to microscale and with different feature shapes and designs [80,81].

A commonly used wicking structure is a micropillar array due both to the ability to model flow in the well-defined structure and the effectiveness of the design for wicking. Previous studies have typically modelled flow in a pillar array using either the Brinkman equation or Darcy's law,

treating the array as an isotropic porous medium [82-87]. The permeability of a quadratic pillar array, for example, needed to use the Brinkman equation or Darcy's law has also been determined computationally and confirmed experimentally [84,88]. More detailed numerical models to accurately capture wicking in pillar arrays accounting for such effects as meniscus curvature have also been developed [43]. In all of these studies, the pillar arrays used have been uniform (i.e. same pillar pitch (l), diameter (d), and height (h) everywhere in the array). In a uniform array, the competing effects of capillary pressure and viscous resistance give rise to an optimum pillar pitch and diameter (for a given pillar height) to maximize the ability of the surface to wick fluid [83]. The liquid pressure along the wicking direction (generated via capillarity) for one such array (h = 25 μm), calculated using the model described in section 2 of this manuscript, is shown in Figure 42b. As the heat flux, q'', increases the pressure drop also increases. Eventually, the pressure drop becomes large enough that the maximum possible capillary pressure sustainable by the wick is reached and dry-out occurs at q'' = 61 W/cm^2.

However, a variable wick (depicted in Figure 42c) that allows the array geometry to vary along the wicking direction could improve the thin film evaporation performance. Figure 42d shows the effective permeability (solid lines and left axis) and maximum capillary pressure (dashed line and right axis) of pillar arrays with different pillar diameter and pitch (h = 25 μm). The permeability increases as pitch increases and diameter decreases, but the capillary pressure has the opposite behaviour, which leads to an optimum design for uniform arrays. However, as seen in Figure 42b, the relative liquid pressure only reaches the maximum capillary pressure at the end of the uniform wick. Therefore, in earlier regions of the wick, the large capillary pressure is not needed. Instead, the array at that location could be designed for a smaller capillary pressure, which would result in a higher permeability as seen in Figure 42d. Similarly, towards the end of the wick, where relative liquid pressure is lowest, the capillary pressure could be increased at the expense of the permeability, allowing the dry-out heat flux to be increased.

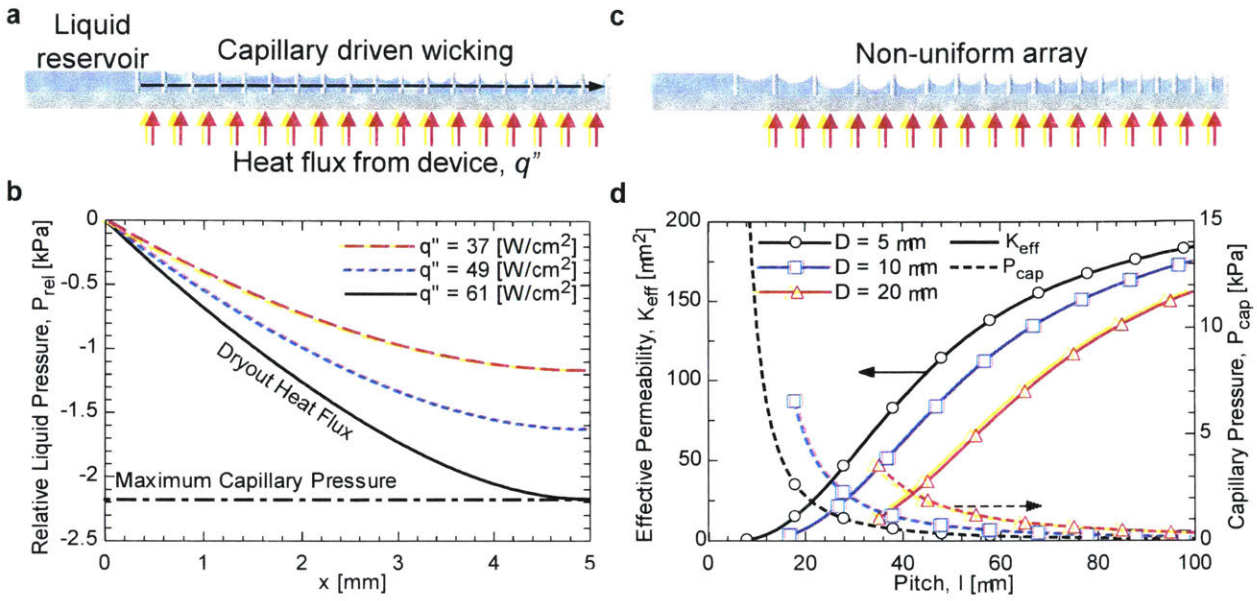

Figure 42: Uniform vs non-uniform pillar arrays.

***a**, Schematic of thermal management based on thin film evaporation from porous wicks. Fluid for evaporation is supplied passively via capillary driven wicking. **b**, Relative liquid pressure at different applied heat fluxes along a 5 mm wicking length for a uniform square pillar array with pillar height, pitch, and diameter of 25 μm, 30 μm, and 10 μm, respectively. At a heat flux of 61 W/cm^2, the maximum possible capillary pressure sustainable by the surface is reached and dry-out occurs. **c**, Schematic of the proposed concept of a pillar array that allows the diameter and/or pitch to vary along the wicking direction. This allows the maximum capillary pressure of the surface to be matched to the relative liquid pressure along the wicking direction, thereby increasing the permeability of the surface structures and, consequently, the dry-out heat flux achievable. **d**, The permeability, K_{eff} (assuming a flat interface) and maximum capillary pressure (assuming receding contact angle of 15 deg., value for water on silicon dioxide [156]) of pillar arrays of various diameters and pitches relevant to thin film evaporation devices. Higher permeability corresponds to a lower capillary pressure and vice versa.*

In this work, we model and design a variable wick for thin film evaporation with enhanced dry-out heat flux by minimizing the pressure drop at each location along the pillar array. This is done by determining the combination of pitch and diameter with the lowest pressure drop at each location that remains within design constraints. The constraints ensure spontaneous wicking of the liquid, a wick design that can be easily fabricated, and the validity of previously developed

relationships for effective wick permeability. The nonuniform wick was compared to the optimum uniform pillar array, and dry-out heat flux enhancement between 2.5x and 3x was observed.

6.2 Modeling a Variable Permeability Wick

To design and model the variable permeability wick, we built on previous modeling efforts for flow in uniform pillar arrays. The array is shown schematically in Figure 43 along with the control volume used in a single cell of the array. Water at 100 °C flows into the array at $x = 0$ from a large fluid reservoir. The relative fluid pressure at this location, $P_{rel,0}$, is 0 Pa. It is assumed that no sensible heating of the fluid occurs as it flows through the wick.

A mass and energy balance on the entire pillar array in Figure 43 was used to solve the volume flow rate of liquid as a function of x, which is found to be:

$$\dot{V}(x) = \frac{q''(L-x)}{\rho_l h_{fg}} \tag{44}$$

where $\dot{V}$ is the volume flow rate per unit width, L is the total length of the wick, x is the distance along the wicking direction, ρ_l is the liquid density, and h_{fg} is the enthalpy of vaporization (the difference in enthalpy of vapor and liquid at 100 °C, $h_v - h_l$). Therefore, the average velocity, u_{avg}, along x is given by:

$$u_{avg}(x) = \frac{\dot{V}(x)}{h_{eff}} = \frac{q''(L-x)}{\rho_l h_{fg} h_{eff}} \tag{45}$$

where h_{eff} is the effective height of the pillar accounting for meniscus curvature and is defined as [84]:

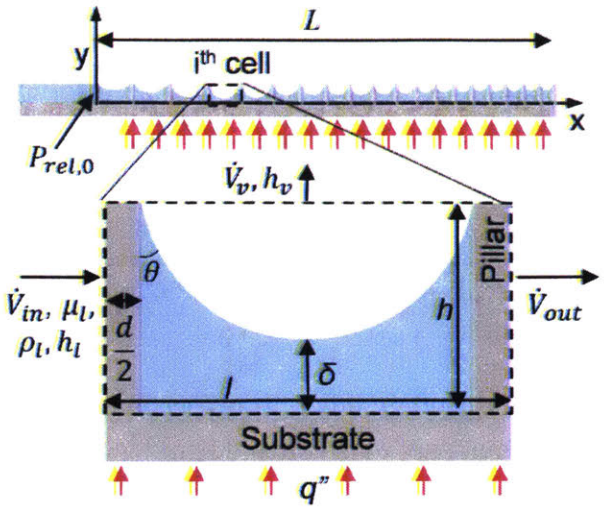

Figure 43: Schematic of parameters of a variable permeability wick.

Schematic of the variable pillar array and a single cell in the array depicting the relevant geometry as well as heat and mass transfer.

$$h_{eff} = h - \left(0.01476 + 0.85009\cos\theta + 0.215\left(\frac{d}{l}\right) + 0.18979\cos^2\theta - 3.46929\left(\frac{d}{l}\right)\cos\theta - 0.28868\left(\frac{d}{l}\right)^2 + 1.05357\left(\frac{d}{l}\right)\cos^2\theta + 3.12583cos\theta\left(\frac{d}{l}\right)^2 - 1.4243\left(\frac{d}{l}\right)^2\cos^2\theta\right)d \quad (46)$$

in which θ is the liquid-solid contact angle. In order to determine the velocity, u, of the liquid within the wick and connect that to the pressure drop along the wick, the Brinkman equation, a modified version of the Navier-Stokes equation that incorporates a permeability term for flow through porous media, was used:

$$\frac{\mu}{\varepsilon}\frac{d^2u}{dy^2} - \frac{dP_{rel}}{dx} - \frac{\mu}{K_{eff}}u = 0 \quad (47)$$

where ε is the porosity of the array ($\varepsilon = 1 - \pi d^2/4l^2$), μ is the liquid viscosity, and K_{eff} is the effective permeability accounting for meniscus curvature. Solving the Brinkman equation with a no-slip boundary at $y = 0$ and a no-shear boundary at $y = h_{eff}$ results in the following velocity profile:

$$u(x,y) = A\exp\left(\sqrt{\frac{\varepsilon}{K_{eff}}}y\right) + B\exp\left(-\sqrt{\frac{\varepsilon}{K_{eff}}}y\right) - \frac{K_{eff}}{\mu}\frac{dP_{rel}}{dx} \tag{48}$$

such that:

$$A = \frac{\frac{dP_{rel}}{dx}\left[\exp\left(-h_{eff}\sqrt{\frac{\varepsilon}{K_{eff}}}\right)K_{eff}\right]}{\mu\left[\exp\left(h_{eff}\sqrt{\frac{\varepsilon}{K_{eff}}}\right)+\exp\left(-h_{eff}\sqrt{\frac{\varepsilon}{K_{eff}}}\right)\right]} \text{ and } B = \frac{\frac{dP_{rel}}{dx}\left[\exp\left(h_{eff}\sqrt{\frac{\varepsilon}{K_{eff}}}\right)K_{eff}\right]}{\mu\left[\exp\left(h_{eff}\sqrt{\frac{\varepsilon}{K_{eff}}}\right)+\exp\left(-h_{eff}\sqrt{\frac{\varepsilon}{K_{eff}}}\right)\right]} \tag{49}$$

The effective permeability, K_{eff}, of quadratic pillar arrays accounting for the curvature of the meniscus has also been studied previously by Byon and Kim [84], who developed the following expression:

$$K_{2D} = \frac{l^2\ln(s^{-0.5} - 0.738 + s - 0.887s^2 + 2.038s^3)}{4\pi} \tag{50}$$

$$K_{eff} = K_{2D}\left[1 - \frac{\exp\left(2\sqrt{\frac{\varepsilon}{K_{2D}}}h_{eff}\right) - 1}{\sqrt{\frac{\varepsilon}{K_{2D}}}h_{eff}\left(\exp\left(2\sqrt{\frac{\varepsilon}{K_{2D}}}h_{eff}\right) + 1\right)}\right]\Lambda_1\Lambda_2 \tag{51}$$

where K_{2D} is the permeability of a quadratic pillar array without accounting for curvature and s is the surface solid fraction ($s = 1 - \varepsilon$). Λ_1 accounts for variation in wetted area and Λ_2 for variation in the channel cross-section area, A_c, and are defined as:

$$\Lambda_1 = \frac{h_{eff} + \frac{\varepsilon d}{4(1-\varepsilon)}}{h + \frac{\varepsilon d}{4(1-\varepsilon)}}, \quad \Lambda_2 = \frac{h_{eff}}{h} \tag{52}$$

The velocity profile $u(x,y)$ in eq. 48 can now be averaged to connect the mean velocity in eq. 45 to the pressure drop along the array as:

$$u_{avg}(x) = \frac{1}{h_{eff}}\int_{y=0}^{y=h_{eff}} u(x,y)dy \tag{53}$$

Furthermore, the capillary pressure, P_{cap}, (and therefore the shape of the meniscus) can be approximated with the following force balance and must equal the relative liquid pressure along the surface [72]:

$$P_{cap} = \frac{4\sigma\cos\theta}{d\left(\frac{4}{\pi}\left(\frac{l}{d}\right)^2 - 1\right)} = P_{rel} \tag{54}$$

where σ is the surface tension of the liquid. These equations allow us to relate the applied heat flux and pillar geometry to the relative liquid pressure and meniscus shape along the wick. In order to solve for $P_{rel}(x)$, we used a cell-by-cell (forward) approach since P_{rel}, u_{avg}, and the pillar geometry are all known at $x = 0$. This allows dP_{rel}/dx to be solved for the first cell, which in turn determines P_{rel} at the start of the second cell, allowing dP_{rel}/dx and the optimum geometry for that cell to be solved, and so forth for the rest of the surface.

6.3 Design Constraints and Pressure Drop Minimization

In order to solve the equations in section 6.2 and also design a surface that can be reasonably fabricated, constraints must be applied to pillar pitch, diameter, and height (in this work, the pillar height is constant across the array). Figure 44a summarizes the constraints placed on pillar geometry for a pillar height of 25 μm. First, eq. 51 is only valid for arrays with $h/l > 0.2$ and $0.06 < d/l < 0.6$. Second, a minimum pillar diameter is set at 4 μm to ensure the pillars can be fabricated and are also strong enough to withstand the forces applied by liquid surface tension. Third, in order for the pillar array to be spontaneously wicking, it must satisfy the imbibition criterion $\cos\theta_{rec} = (1 - s)/(r - s)$, where θ_{rec} is the receding contact angle and r is the roughness ($r = (l^2 + \pi dh)/l^2$). Finally, the contact angle must always be greater than or equal to the receding contact angle, $\theta \geq \theta_{rec}$, which was set to 15 degrees (value for water on silicon dioxide [156]) in this work. The distance between the lowest point of the meniscus and the bottom of the pillar array was also constrained to always be greater than 0, $\delta > 0$, as seen in Figure 43 (i.e., the meniscus cannot come in contact with the bottom of the array). Assuming the meniscus is a spherical cap, we obtain that $\delta = h - (\sqrt{2}l - d)(1 - \sin\theta)/(2\cos\theta)$ [72].

Subject to the constraints listed above, the pressure drop across each cell was then minimized based on the relative liquid pressure. The minimization was carried out using the Conjugate Directions method, also known

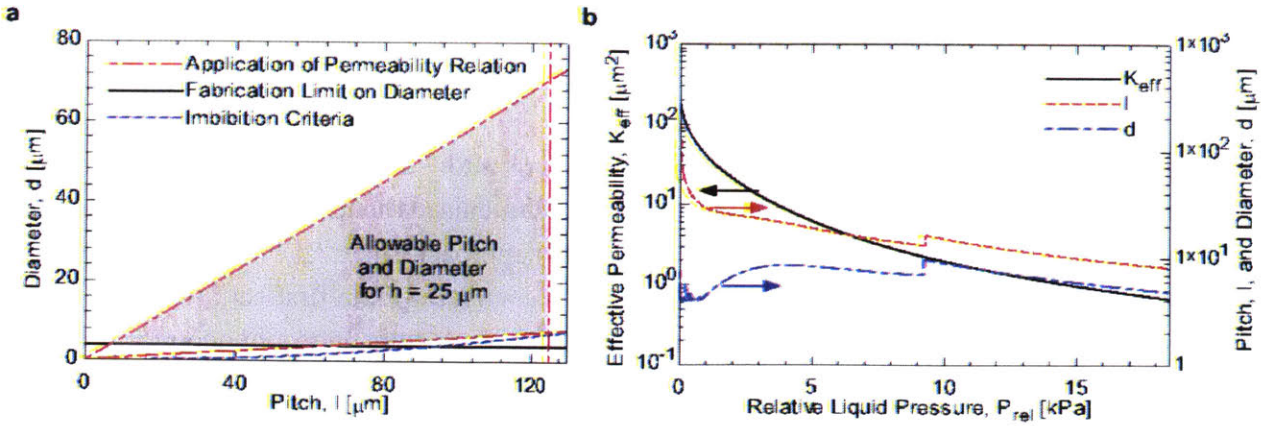

Figure 44: Design Constraints and Minimization of Pressure Drop.

***a**, Constraints on the diameter and pitch of the pillar array used to determine allowable values. Imbibition ensures spontaneous wicking. The fabrication limit on the diameter is imposed to ensure the ability to fabricate robust structures via standard silicon microfabrication processes. Finally, the range of possible pitches and diameters used in the relations for effective permeability,* K_{eff}, *and effective height,* h_{eff}, *(Eq. 51 and 46, respectively) is limited to ensure the validity of the proposed design. Note that these constraints are not all fundamental in nature, and some constraints can be overcome to further enhance performance. **b**, Effective permeability, diameter, and pitch to minimize* dP_{rel}/dx *for different relative liquid pressures subject to the constraints in Figure 44a.*

as the direct search method or Powell's method, which uses a series of one-dimensional searches to locate the optimum of a function of multiple variables [157]. The result of the minimization is shown in Figure 44b, which shows the effective permeability for all relative liquid pressures in this study, as well as the corresponding pitch and diameter, subject to the constraints in Figure 44a, that results in the minimum. The permeability, pitch, and diameter shown in Figure 44b were then used to set the geometry of each cell dependent on the relative liquid pressure of that cell in the cell-by-cell (forward) approach used.

6.4 Results and Discussion

Nonuniform arrays and optimum uniform arrays were considered for a variety of pillar heights commonly found in literature (h = 15 μm to 55 μm). Figure 45a shows the diameter and pitch for both types of arrays with L = 5 mm and taking h = 25 μm. The optimum pitch and diameter for the uniform array were found to be ~30 μm and ~10 μm, respectively. The nonuniform array diameter and pitch, on the other hand, varied along the surface in order to minimize the pressure drop. The dry-out heat flux for the uniform array was 61 W/cm^2. The effective permeability and

relative liquid pressure along the uniform array are shown in Figure 45b. The permeability decreases with x for the uniform array due to increasing curvature of the meniscus. The nonuniform array shown in Figure 45c, however, had a dry-out heat flux of 172 W/cm^2, about 2.8x that of the uniform array. This is a direct result of the permeability at the beginning of the array being higher than that of the uniform array (due to the larger pitch and smaller diameter), as well as the maximum sustainable capillary pressure at the end of the array also being higher (due to smaller pitch and diameter). It is also important to note that the constraints used in Figure 44a limit the performance and are not all fundamental in nature. For example, maximum and minimum pitch and diameter are set by the fabrication limit and constraints to properly apply the permeability relation. Therefore, overcoming these limits could further enhance performance of the nonuniform wick.

Figure 45d shows the dry-out heat flux for the two designs (optimized uniform and nonuniform) for different pillar heights. It also shows the enhancement achieved by using the nonuniform wick (ratio of the corresponding dry-out heat fluxes). The nonuniform wick showed enhancement ranging between 2.5x and 3x for the pillar heights modelled. The reduced enhancement at smaller pillar heights is a result of the constraints on the pillar geometry becoming more restrictive.

6.5 Conclusions and Outlook

The results of this study demonstrate that enhanced wicking can be achieved by allowing wick geometry to vary along the wicking direction. This variation benefits the wick in two ways. First, it allows the wick permeability to be increased towards the beginning of the wick where liquid velocity is high, greatly reducing the pressure drop. Second, towards the end of the wick, the variation allows the maximum sustainable capillary pressure to be greatly increased compared to uniform wicks. Combined, these two effects lead to an improvement of dry-out heat flux between 2.5x and 3x for a range of pillar heights commonly used for wicking enhancement in thin film evaporation. This improvement was achieved for a wick design constrained to ensure feasibility of fabrication as well as appropriate use of permeability relations. Therefore, it is expected that these constraints could be loosened to achieve even greater enhancement. Further studies in this area should experimentally validate the enhancement. As thin film evaporation in wicks is pushed to higher heat fluxes, it is possible for unexpected issues to occur, such as nucleate boiling within structures. We expect these issues could be addressed by incorporating further constraints on wick geometry. The permeability relation used in this study ultimately constrained the final design. By developing new relationships with less restrictive constraints, the enhancement could be increased further. It must also be kept in mind that the relationships used in this study were designed/developed (first and foremost) for uniform arrays. In our work (with nonuniform arrays), though, it was assumed that variation in geometry across one cell was small enough for

the relationships to still be valid. While this was generally true, significant variation in pitch was observed near the beginning of the wick. Future studies could consider the effect of the nonuniform cells on permeability, capillary pressure, and meniscus shape.

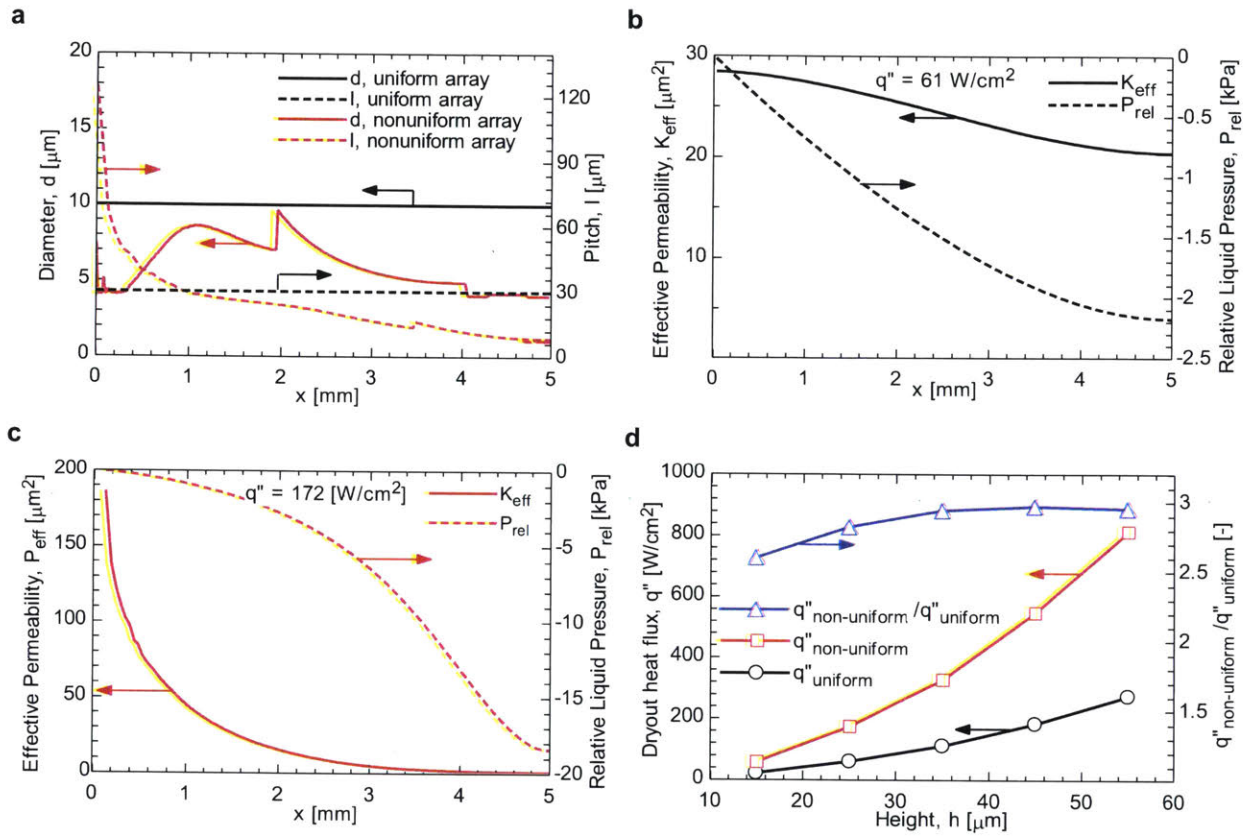

Figure 45: Modeling Results of Varied Permeability Pillar Array.

***a**, Pitch and diameter along x for the optimized uniform pillar array as well as the nonuniform array designed based on the proposed modelling framework. Both use a pillar height of* h = *25 μm. The nonuniform array is constrained by imbibition at small x, after which it is constrained by the minimum diameter and the region of validity of the permeability relation. (b,c) Effective permeability and relative liquid pressure at dry-out for **b**, the optimum uniform array (l = 30 μm, d = 10 μm) and **c**, the nonuniform array. The nonuniform array exhibits higher permeability at small x and larger capillary pressure at larger x than the uniform array, leading to enhanced performance. **d**, Dry-out heat flux for the optimized uniform array and the nonuniform array for different pillar heights. Enhancement of the varied array over a uniform array is also shown and is between 2.5x and 3x for a wide range of pillar heights. The changing degree of enhancement is due to the constraints on pillar geometry becoming more restrictive at smaller pillar heights.*

In summary, nonuniform pillar arrays for enhanced wicking were modelled, with enhancement of dry-out heat flux between 2.5x and 3x predicted for a range of pillar heights. The enhancement was achieved by minimizing the pressure drop at each wick location via variation of the pillar diameter and pitch. The results of this study will enable improved performance in phase-change based thermal management techniques, such as thin film evaporation and pool boiling, that use capillary-assisted wicking.

7. Summary and Perspectives

In classical wetting theory, the necessity to tailor the chemistry, and to a lesser extent the geometry, of a surface to achieve desired wetting behavior leads to significant challenges, particularly when surfaces are exposed to extreme conditions, when extreme combinations of liquids and surface materials are used, and when extreme liquid behaviors are desired. This thesis addressed a number of these challenging areas. In chapter 2, we addressed durability issues with high thermal conductance, hydrophobic coatings for promoting dropwise condensation. In chapter 3-5, we discussed the use of reentrant microstructures to shift the wetting paradigm. This enabled us to achieve any wetting behavior desired independent of the chemical nature of the surface and liquid used. We addressed robustness issues with reentrant surfaces, which were previously unable to maintain repellency during condensation, and we explored alternative fabrication methods to achieve doubly reentrant surfaces. By using intrinsic stresses in thin films, we were able to utilize standard microfabrication processes. In chapter 6, we enhanced wicking in pillar arrays by allowing pillar pitch and diameter to vary, optimizing each section of the wick for minimal pressure drop, increasing the overall wicking performance. Perspectives, challenges, and future directions for each area are presented here.

7.1 Polymer Infused Porous Surfaces

Dropwise condensation, promoted by hydrophobic coatings, can enhance condensation heat transfer by an order of magnitude over the industry standard, filmwise condensation. However, the harsh condenser environments and stringent heat transfer requirements have caused coatings that promote dropwise condensation to be plagued by durability issues[14]. We demonstrated that by simultaneously addressing the poor adhesion to condenser surfaces and the low-thermal-conductivity of hydrophobic polymers by creating composites of nanostructures and polymer, high-performance dropwise condensation can be achieved for periods of time significantly longer than previously demonstrated in literature[24].

This combination of performance and lifetime is exciting. The work in this thesis, however, should be expanded to completely understand if polymer infused porous surfaces represent a path to sustained condensation enhancement. First, although no degradation to condensation heat transfer on PIPS was observed in a pure steam environment over 200 days, degradation rates on the order of 1 μm/year were observed in a sodium chloride solution. It would be valuable to understand specifically how this degradation changes PIPS properties and if it also occurs at a slower rate in a pure steam environment. For example, the embedded nanostructure is more reactive in the sodium chloride solution than the low-surface-energy polymer. If this leads to degradation where the nanostructure is destroyed selectively, leaving the low-thermal-conductivity polymer behind, the adhesion of the polymer could be affected, not to

mention the overall effective thermal conductivity of the composite coating could be reduced, both of which would have adverse effects on the overall coating performance. Therefore, a deeper understanding of how degradation occurs and how it affects performance is important.

In this work, we demonstrated two types of PIPS, one with low-thermal-conductivity copper oxide nanoblades less than a couple μm thick, and one with high-thermal-conductivity copper nanowires that could be thicker than 20 μm, both of which demonstrated significant heat transfer enhancement. This suggests that there is flexibility in the choice and design of PIPS. Future works should consider nanostructure and polymer choice to optimize performance in terms of durability and heat transfer enhancement. Of particular interest would be to explore combinations of nanostructure and polymer that are scalable and economically feasible at powerplant scales. Although we have demonstrated promising performance and lifetime, if the coating is prohibitively expensive it will ultimately have no impact.

Although we demonstrated condensation heat transfer enhancement in this thesis, hydrophobic coatings are also valuable in other areas as well. For example, boiling is also heavily used in power generation and thermal management. Hydrophobic coatings can significantly enhance the boiling heat transfer coefficient by enhancing bubble nucleation. Similarly, by using biphilic surface consisting of a hydrophilic surface with hydrophobic islands to tailor nucleation spacing, the critical heat flux can be increased, which is the maximum heat flux the surface can sustain before undergoing a temperature spike due to a transition to film boiling[15]. Applying similar coating design as PIPS to other heat transfer areas that benefit from low-surface-energy coatings should be explored.

Finally, this work has taken steps to improve performance and lifetime of coatings based on empirical observations, however, underlying degradation mechanisms remain elusive and led to two significant challenges. Previous studies, including research we conducted at the beginning of this project, focused on testing a variety of coatings and observing performance. We chose this approach given numerous degradation mechanisms existed, and it was not initially clear 1. which mechanism dominated degradation and 2. how to decouple different mechanisms from one another. This required testing a variety of coatings for extended periods of time, which ultimately revealed coating adhesion and thickness were crucial factors. Without methods for accelerated testing this approach was inefficient and did not elucidate specific causes for failure due to adhesion. In future studies, exploring causes of coating delamination, as well as methods to prevent it, would provide more concrete design guidelines and potentially superior coatings.

7.2 Reentrant Microstructures

Reentrant micro/nanostructures achieve material/liquid independent wetting behavior. Previously, researchers have shown this enables omniphobic surfaces that are able to repel any

liquid, including liquids that are otherwise naturally wetting[52]. In our work, we extend this material/liquid independent behavior to various other wetting phenomena, including omniphilicity, switchability, and selectivity.

Previously, these wetting behaviors were very difficult to achieve, which constrained the materials used or wetting behavior achieved in a variety of systems. Although we mentioned a number of potential applications in Chapter 3, further thought should be given not only to which applications would benefit from these functionalities, but also to the specific surface designs that should be used. For example, previous work has shown that rational design can improve the robustness of omniphobic reentrant surfaces to various mechanisms of failure, such as exceeding the breakthrough pressure, defects, and condensation[62,124,130]. In these works, design considered improving robustness for repellency only. Given other surface functionalities such as omniphilicity rely on the same physical mechanisms as omniphobicity, i.e., metastable states enabled by contact line pinning, we believe the same design logic used to improve robustness of omniphobic surfaces should apply to the other functionalities reentrant structures enable. However, thought should be given to what specific criteria are important for each application space, and surfaces designed accordingly.

Also, although we demonstrated that rational design can be used to address failure mechanisms, a universal robust design with ideal wetting behavior has not been found. For example, in chapter 4, we created surfaces robust to condensation induced failure. However, in order to achieve this, sacrifices to repellency were made. Specifically, the reentrant cavity design used had increased contact angle hysteresis compared to previous designs, which prevents droplet mobility on the surface. Surface designs that can simultaneously optimize liquid wetting behavior without sacrificing robustness should be explored.

Similar to PIPS, although we demonstrated many exciting functionalities with reentrant microstructures, scalable and cost-effective manufacturing methods must be found. In fact, throughout this thesis, fabrication was the most challenging component. For condensation-resistant omniphobic surfaces we had to develop a new fabrication method to create the nanometer size features required. Currently, reentrant microstructures are typically created using silicon microfabrication processes in cleanrooms. As a result, surfaces with reentrant microstructures tend to be limited in terms of materials used and characteristic sizes that can be achieved, are expensive to fabricate, and must be made on smooth, planar surfaces such as silicon wafers. Each of these limits ultimately also limit the use of reentrant microstructures for practical applications. Scalable fabrication techniques that can be applied to different types of surfaces need to be developed. We believe important steps have already been made and need only to be applied to the field of tailoring wetting behavior. For example, previous works have

created complex nanostructures with controlled shapes on various surface materials, and theorized these nanostructures can exhibit moderate levels of reentrance[140]. Exploration of different methods of creating structured surfaces, with the express purpose of creating reentrant structures scalably, would greatly increase the practicality of the surfaces.

7.3 Nonuniform Wicks for Enhanced Wicking

Wicking surfaces are used in many applications. However, the uniform wicks that are used can limit performance due to a coupling between the capillary pressure that drives the liquid flow and the viscous resistance that hinders it. Our modeling suggested that significant improvement to wicking performance (3x) can be achieved simply by allowing the wick properties to vary along the surface, thereby allowing wick dimensions at each location to be chosen to minimize pressure drop. However, this work should be experimentally validated to demonstrate the enhancement, and the modeling refined to account for different effects. For example, it was assumed that each cell behaves as if it were a cell with uniform pitch. This assumption is certainly valid in regions on the surface where wick dimensions change slowly. However, certain regions, particularly at the beginning of the wick, have dimension that change rapidly. The validity of this assumption and its effect on the end result should be more carefully explored.

The modeling in chapter 6 also only considered the case where the wick is completely filled with liquid while evaporation occurred from the surface. Although this is a highly relevant scenario to thermal management of electronics, certain applications have fundamentally different behavior. For example, when a dry wicking surface is first brought into contact with a liquid, a wicking front propagates through the surface structures as they fill. It would be interesting to explore if this scenario with a propagating wicking front can have similar enhancement to wicking, and how that changes the design relative to the scenario considered in chapter 6.

Finally, there are other wick designs that also improve performance. For example, hierarchical wicks that consist of a nanoporous membrane supported on top of larger structures allow the capillary pressure that drives the liquid flow and the viscous resistance that hinders it to be largely decoupled[70]. Therefore, a properly designed hierarchical wick would have superior performance to a nonuniform wick. Understanding the advantages and disadvantages of uniform, nonuniform, and hierarchical wicks and in which applications each should be used is necessary to create high performance devices using these strategies.

8. Bibliography

1 Quéré, D. Wetting and roughness. *Annual Review of Materials Research* **38**, 71-99 (2008).

2 Dettre, R. & Johnson, R. Contact angle hysteresis, I. Study of an idealized rough surface. *Advances in Chemistry Series* **43**, 112 (1964).

3 Wenzel, R. N. Resistance of solid surfaces to wetting by water. *Industrial & Engineering Chemistry* **28**, 988-994 (1936).

4 Cassie, A. & Baxter, S. Wettability of porous surfaces. *Transactions of the Faraday Society* **40**, 546-551 (1944).

5 Bico, J., Tordeux, C. & Quéré, D. Rough wetting. *EPL (Europhysics Letters)* **55**, 214 (2001).

6 Beér, J. M. High efficiency electric power generation: The environmental role. *Progress in Energy and combustion science* **33**, 107-134 (2007).

7 Glicksman, L. R. & Hunt Jr, A. W. Numerical simulation of dropwise condensation. *International journal of heat and mass transfer* **15**, 2251-2269 (1972).

8 Schilling, H. Improving the Efficiency of Pulverised Coal Fired Power Generating Plant. *VGB KraftwerksTechnik (English edition)* **73**, 564-576 (1993).

9 Humplik, T. *et al.* Nanostructured materials for water desalination. *Nanotechnology* **22**, 292001 (2011).

10 Andrews, H., Eccles, E., Schofield, W. & Badyal, J. Three-dimensional hierarchical structures for fog harvesting. *Langmuir* **27**, 3798-3802 (2011).

11 Khawaji, A. D., Kutubkhanah, I. K. & Wie, J.-M. Advances in seawater desalination technologies. *Desalination* **221**, 47-69 (2008).

12 Leach, R., Stevens, F., Langford, S. & Dickinson, J. Dropwise condensation: experiments and simulations of nucleation and growth of water drops in a cooling system. *Langmuir* **22**, 8864-8872 (2006).

13 Peters, T. B. *et al.* Design of an integrated loop heat pipe air-cooled heat exchanger for high performance electronics. *IEEE Transactions on Components, Packaging and Manufacturing Technology* **2**, 1637-1648 (2012).

14 Rose, J. Dropwise condensation theory and experiment: a review. *Proceedings of the Institution of Mechanical Engineers, Part A: Journal of Power and Energy* **216**, 115-128 (2002).

15 Cho, H. J., Preston, D. J., Zhu, Y. & Wang, E. N. Nanoengineered materials for liquid–vapour phase-change heat transfer. *Nature Reviews Materials* **2**, 16092 (2017).

16 Penniman, A. L. (Google Patents, 1935).

17 Drew, T., Nagle, W. & Smith, W. The conditions for dropwise condensation of steam. *AIChE Transactions* **31**, 605-621 (1935).

18 Nagle, W. u., Bays, G., Blenderman, L. & Drew, T. Heat-transfer coefficients during dropwise condensation of steam. *Trans. AIChE* **31**, 593-621 (1935).

19 Blackman, L., Dewar, M. & Hampson, H. An investigation of compounds promoting the dropwise condensation of steam. *Journal of Applied Chemistry* **7**, 160-171 (1957).

20 Vemuri, S., Kim, K., Wood, B., Govindaraju, S. & Bell, T. Long term testing for dropwise condensation using self-assembled monolayer coatings of n-octadecyl mercaptan. *Applied thermal engineering* **26**, 421-429 (2006).
21 Das, A., Kilty, H., Marto, P., Andeen, G. & Kumar, A. The use of an organic self-assembled monolayer coating to promote dropwise condensation of steam on horizontal tubes. *Journal of heat transfer* **122**, 278-286 (2000).
22 Chen, L. *et al.* n-Octadecanethiol self-assembled monolayer coating with microscopic roughness for dropwise condensation of steam. *Journal of Thermal Science* **18**, 160-165 (2009).
23 Love, J. C., Estroff, L. A., Kriebel, J. K., Nuzzo, R. G. & Whitesides, G. M. Self-assembled monolayers of thiolates on metals as a form of nanotechnology. *Chemical reviews* **105**, 1103-1170 (2005).
24 Marto, P., Looney, D., Rose, J. & Wanniarachchi, A. Evaluation of organic coatings for the promotion of dropwise condensation of steam. *International Journal of Heat and Mass Transfer* **29**, 1109-1117 (1986).
25 Holden, K., Wanniarachchi, A., Marto, P., Boone, D. & Rose, J. The use of organic coatings to promote dropwise condensation of steam. *Journal of heat transfer* **109**, 768-774 (1987).
26 Ma, X. *et al.* Influence of processing conditions of polymer film on dropwise condensation heat transfer. *International Journal of Heat and Mass Transfer* **45**, 3405-3411 (2002).
27 Haraguchi, T., Shimada, R., Kumagai, S. & Takeyama, T. The effect of polyvinylidene chloride coating thickness on promotion of dropwise steam condensation. *International Journal of Heat and Mass Transfer* **34**, 3047-3054 (1991).
28 Paxson, A. T., Yagüe, J. L., Gleason, K. K. & Varanasi, K. K. Stable dropwise condensation for enhancing heat transfer via the initiated chemical vapor deposition (iCVD) of grafted polymer films. *Advanced Materials* **26**, 418-423 (2014).
29 Anand, S., Paxson, A. T., Dhiman, R., Smith, J. D. & Varanasi, K. K. Enhanced condensation on lubricant-impregnated nanotextured surfaces. *Acs Nano* **6**, 10122-10129 (2012).
30 Weisensee, P. B. *et al.* Condensate droplet size distribution on lubricant-infused surfaces. *International Journal of Heat and Mass Transfer* **109**, 187-199 (2017).
31 Preston, D. J. *et al.* Heat transfer enhancement during water and hydrocarbon condensation on lubricant infused surfaces. *Scientific reports* **8**, 540 (2018).
32 Xiao, R., Miljkovic, N., Enright, R. & Wang, E. N. Immersion condensation on oil-infused heterogeneous surfaces for enhanced heat transfer. *Scientific reports* **3**, 1988 (2013).
33 Preston, D. J., Mafra, D. L., Miljkovic, N., Kong, J. & Wang, E. N. Scalable graphene coatings for enhanced condensation heat transfer. *Nano letters* **15**, 2902-2909 (2015).
34 Boreyko, J. B. & Chen, C.-H. Self-propelled dropwise condensate on superhydrophobic surfaces. *Physical review letters* **103**, 184501 (2009).
35 Miljkovic, N. *et al.* Jumping-droplet-enhanced condensation on scalable superhydrophobic nanostructured surfaces. *Nano letters* **13**, 179-187 (2012).

36 Enright, R., Miljkovic, N., Al-Obeidi, A., Thompson, C. V. & Wang, E. N. Condensation on superhydrophobic surfaces: the role of local energy barriers and structure length scale. *Langmuir* **28**, 14424-14432 (2012).
37 Miljkovic, N. & Wang, E. N. Condensation heat transfer on superhydrophobic surfaces. *MRS bulletin* **38**, 397-406 (2013).
38 Enright, R., Miljkovic, N., Dou, N., Nam, Y. & Wang, E. N. Condensation on superhydrophobic copper oxide nanostructures. *Journal of heat transfer* **135**, 091304 (2013).
39 Preston, D. J. *et al.* Gravitationally driven wicking for enhanced condensation heat transfer. *Langmuir* **34**, 4658-4664 (2018).
40 Wanniarachchi, A., Marto, P. & Rose, J. Film condensation of steam on horizontal finned tubes: effect of fin spacing. *Journal of heat transfer* **108**, 960-966 (1986).
41 Comanns, P. *et al.* Directional, passive liquid transport: the Texas horned lizard as a model for a biomimetic 'liquid diode'. *Journal of the Royal Society Interface* **12**, 20150415 (2015).
42 Wang, R. *et al.* Light-induced amphiphilic surfaces. *Nature* **388**, 431 (1997).
43 Zhu, Y. *et al.* Prediction and characterization of dry-out heat flux in micropillar wick structures. *Langmuir* **32**, 1920-1927 (2016).
44 Faghri, A. *Heat Pipe Science and Technology*. (Global Digital Press, 1995).
45 Lafuma, A. & Quéré, D. Superhydrophobic states. *Nature Materials* **2**, 457-460 (2003).
46 Leslie, D. C. *et al.* A bioinspired omniphobic surface coating on medical devices prevents thrombosis and biofouling. *Nature Biotechnology* **32**, 1134-1140 (2014).
47 Wong, T.-S. *et al.* Bioinspired self-repairing slippery surfaces with pressure-stable omniphobicity. *Nature* **477**, 443-447 (2011).
48 Lee, J., Boo, C., Ryu, W.-H., Taylor, A. D. & Elimelech, M. Development of omniphobic desalination membranes using a charged electrospun nanofiber scaffold. *ACS Applied Materials & Interfaces* **8**, 11154-11161 (2016).
49 Liu, T. & Kim, C.-J. in *Micro Electro Mechanical Systems (MEMS), 2015 28th IEEE International Conference on.* 1122-1124 (IEEE).
50 Choi, C.-H. & Kim, C.-J. Large slip of aqueous liquid flow over a nanoengineered superhydrophobic surface. *Physical Review Letters* **96**, 066001 (2006).
51 Lu, Y. *et al.* Robust self-cleaning surfaces that function when exposed to either air or oil. *Science* **347**, 1132-1135 (2015).
52 Liu, T. & Kim, C.-J. Turning a surface superrepellent even to completely wetting liquids. *Science* **346** (2014).
53 Ellison, A. H., Klemm, R., Schwartz, A. M., Grubb, L. & Petrash, D. A. Contact angles of mercury on various surfaces and the effect of temperature. *Journal of Chemical and Engineering Data* **12**, 607-609 (1967).
54 Smith, T. The hydrophilic nature of a clean gold surface. *Journal of Colloid and Interface Science* **75**, 51-55 (1980).
55 Kavousanakis, M. E. *et al.* How to achieve reversible electrowetting on superhydrophobic surfaces. *Langmuir* **34**, 4173-4179 (2018).

56 Li, J.-J., Zhou, Y.-N. & Luo, Z.-H. Polymeric materials with switchable superwettability for controllable oil/water separation: a comprehensive review. *Progress in Polymer Science* (2018).
57 Yang, J. *et al.* Superhydrophilic–superoleophobic coatings. *Journal of Materials Chemistry* **22**, 2834-2837 (2012).
58 Feng, L. *et al.* A super-hydrophobic and super-oleophilic coating mesh film for the separation of oil and water. *Angewandte Chemie* **116**, 2046-2048 (2004).
59 Krupenkin, T. N., Taylor, J. A., Schneider, T. M. & Yang, S. From rolling ball to complete wetting: the dynamic tuning of liquids on nanostructured surfaces. *Langmuir* **20**, 3824-3827 (2004).
60 Chen, Y., Doshi, N., Goldberg, B., Wang, H. & Wood, R. J. Controllable water surface to underwater transition through electrowetting in a hybrid terrestrial-aquatic microrobot. *Nature Communications* **9**, 2495 (2018).
61 Tuteja, A. *et al.* Designing superoleophobic surfaces. *Science* **318**, 1618-1622 (2007).
62 Wilke, K. L., Preston, D. J., Lu, Z. & Wang, E. N. Toward condensation-resistant omniphobic surfaces. *ACS nano* **12**, 11013-11021 (2018).
63 Squires, T. M. & Quake, S. R. Microfluidics: Fluid physics at the nanoliter scale. *Reviews of modern physics* **77**, 977 (2005).
64 Cui, H.-H. & Lim, K.-M. Pillar array microtraps with negative dielectrophoresis. *Langmuir* **25**, 3336-3339 (2009).
65 He, B., Tait, N. & Regnier, F. Fabrication of nanocolumns for liquid chromatography. *Analytical Chemistry* **70**, 3790-3797 (1998).
66 Patel, N., Rohatgi, V. & Lee, L. J. Micro scale flow behavior and void formation mechanism during impregnation through a unidirectional stitched fiberglass mat. *Polymer Engineering & Science* **35**, 837-851 (1995).
67 Nagrath, S. *et al.* Isolation of rare circulating tumour cells in cancer patients by microchip technology. *Nature* **450**, 1235-1239 (2007).
68 Lips, S., Lefèvre, F. & Bonjour, J. Thermohydraulic study of a flat plate heat pipe by means of confocal microscopy: application to a 2D capillary structure. *Journal of Heat Transfer* **132**, 112901 (2010).
69 Nam, Y., Sharratt, S., Byon, C., Kim, S. J. & Ju, Y. S. Fabrication and characterization of the capillary performance of superhydrophilic Cu micropost arrays. *Journal of Microelectromechanical Systems* **19**, 581-588 (2010).
70 Wilke, K. L., Barabadi, B., Lu, Z., Zhang, T. & Wang, E. N. Parametric study of thin film evaporation from nanoporous membranes. *Applied Physics Letters* **111**, 171603 (2017).
71 Wilke, K. L., Barabadi, B., Zhang, T. & Wang, E. N. Controlled Wetting in Nanoporous Membranes for Thin Film Evaporation. *Journal of Heat Transfer* **138**, 080906 (2016).
72 Adera, S., Antao, D., Raj, R. & Wang, E. N. Design of micropillar wicks for thin-film evaporation. *International Journal of Heat and Mass Transfer* **101**, 280-294 (2016).
73 Antao, D. S. *et al.* Dynamic Evolution of the Evaporating Liquid–Vapor Interface in Micropillar Arrays. *Langmuir* **32**, 519-526 (2016).
74 Kim, B. S., Lee, H., Shin, S., Choi, G. & Cho, H. H. Interfacial wicking dynamics and its impact on critical heat flux of boiling heat transfer. *Applied Physics Letters* **105**, 191601 (2014).

75 Dhillon, N. S., Buongiorno, J. & Varanasi, K. K. Critical heat flux maxima during boiling crisis on textured surfaces. *Nature Communications* **6** (2015).
76 Zhu, Y., Antao, D. S., Zhang, T. & Wang, E. N. Suppressed Dry-out in Two-Phase Microchannels via Surface Structures. *Journal of Heat Transfer* **138**, 080905 (2016).
77 Zhu, Y. *et al.* Surface structure enhanced microchannel flow boiling. *Journal of Heat Transfer* **138**, 091501 (2016).
78 Zhu, Y. *et al.* Suppressing high-frequency temperature oscillations in microchannels with surface structures. *Applied Physics Letters* **110**, 033501 (2017).
79 Rahman, M. M., Olceroglu, E. & McCarthy, M. Role of wickability on the critical heat flux of structured superhydrophilic surfaces. *Langmuir* **30**, 11225-11234 (2014).
80 Ranjan, R., Patel, A., Garimella, S. V. & Murthy, J. Y. Wicking and thermal characteristics of micropillared structures for use in passive heat spreaders. *International Journal of Heat and Mass Transfer* **55**, 586-596 (2012).
81 Jo, H. S. *et al.* Effects of Capillarity on Pool Boiling Using Nanotextured Surfaces through Electrosprayed BiVO 4 Nanopillars. *Chemical Engineering Science* (2017).
82 Hale, R., Ranjan, R. & Hidrovo, C. Capillary flow through rectangular micropillar arrays. *International Journal of Heat and Mass Transfer* **75**, 710-717 (2014).
83 Xiao, R., Enright, R. & Wang, E. N. Prediction and optimization of liquid propagation in micropillar arrays. *Langmuir* **26**, 15070-15075 (2010).
84 Byon, C. & Kim, S. J. The effect of meniscus on the permeability of micro-post arrays. *Journal of Micromechanics and Microengineering* **21**, 115011 (2011).
85 Ravi, S., Horner, D. & Moghaddam, S. Monoporous micropillar wick structures, I-Mass transport characteristics. *Applied Thermal Engineering* **73**, 1371-1377 (2014).
86 Horner, D., Ravi, S. & Moghaddam, S. Monoporous micropillar wick structures, II-optimization & theoretical limits. *Applied Thermal Engineering* **73**, 1378-1386 (2014).
87 Brinkman, H. A calculation of the viscous force exerted by a flowing fluid on a dense swarm of particles. *Applied Scientific Research* **1**, 27-34 (1949).
88 Sangani, A. & Acrivos, A. Slow flow past periodic arrays of cylinders with application to heat transfer. *International journal of Multiphase flow* **8**, 193-206 (1982).
89 Schmidt, E., Schurig, W. & Sellschopp, W. Versuche über die Kondensation von Wasserdampf in Film-und Tropfenform. *Technische Mechanik und Thermodynamik* **1**, 53-63 (1930).
90 Fitzpatrick, J., Baum, S. & McAdams, W. Dropwise condensation of steam on vertical tubes. *Trans. AIChE* **35**, 97-107 (1939).
91 McCormick, J. & Westwater, J. Nucleation sites for dropwise condensation. *Chemical Engineering Science* **20**, 1021-1036 (1965).
92 Umur, A. & Griffith, P. Mechanism of dropwise condensation. *Journal of heat transfer* **87**, 275-282 (1965).
93 Kollera, M. & Grigull, U. Über das Abspringen von Tropfen bei der Kondensation von Quecksilber. *Wärme-und Stoffübertragung* **2**, 31-35 (1969).
94 Chemours. *Teflon AF amorphous fluoroplastics*, <https://www.chemours.com/Teflon_Industrial/en_US/products/product_by_name/teflon_af/index.html> (2019).

95 Neumann, A., Abdelmessih, A. & Hameed, A. The role of contact angles and contact angle hysteresis in dropwise condensation heat transfer. *International Journal of Heat and Mass Transfer* **21**, 947-953 (1978).
96 Awaja, F., Gilbert, M., Kelly, G., Fox, B. & Pigram, P. J. Adhesion of polymers. *Progress in polymer science* **34**, 948-968 (2009).
97 Choi, W., Tuteja, A., Mabry, J. M., Cohen, R. E. & McKinley, G. H. A modified Cassie–Baxter relationship to explain contact angle hysteresis and anisotropy on non-wetting textured surfaces. *Journal of Colloid and Interface Science* **339**, 208-216 (2009).
98 Burger, N. *et al.* Review of thermal conductivity in composites: mechanisms, parameters and theory. *Progress in polymer science* **61**, 1-28 (2016).
99 MANTLE, W. J. & CHANG, W. S. Effective thermal conductivity of sintered metal fibers. *Journal of Thermophysics and Heat Transfer* **5**, 545-549, doi:10.2514/3.299 (1991).
100 Singh, B., Dybbs, A. & Lyman, F. Experimental study of the effective thermal conductivity of liquid saturated sintered fiber metal wicks. *International Journal of Heat and Mass Transfer* **16**, 145-155 (1973).
101 Wen, R., Xu, S., Ma, X., Lee, Y.-C. & Yang, R. Three-dimensional superhydrophobic nanowire networks for enhancing condensation heat transfer. *Joule* **2**, 269-279 (2018).
102 Hager, M. D., Greil, P., Leyens, C., van der Zwaag, S. & Schubert, U. S. Self-healing materials. *Advanced Materials* **22**, 5424-5430 (2010).
103 Blaiszik, B. J. *et al.* Self-healing polymers and composites. *Annual Review of Materials Research* **40**, 179-211 (2010).
104 Morra, M., Occhiello, E. & Garbassi, F. in *High Energy Density Technologies in Materials Science* 161-168 (Springer, 1990).
105 McCafferty, E. Validation of corrosion rates measured by the Tafel extrapolation method. *Corrosion Science* **47**, 3202-3215 (2005).
106 Kwon, G., Post, E. & Tuteja, A. Membranes with selective wettability for the separation of oil–water mixtures. *MRS Communications* **5**, 475-494 (2015).
107 Vazquez, G., Alvarez, E. & Navaza, J. M. Surface tension of alcohol + water from 20 to 50 degree C. *Journal of Chemical and Engineering Data* **40**, 611-614 (1995).
108 Gao, L. & McCarthy, T. J. How Wenzel and Cassie were wrong. *Langmuir* **23**, 3762-3765 (2007).
109 McHale, G. Cassie and Wenzel: were they really so wrong? *Langmuir* **23**, 8200-8205 (2007).
110 Panchagnula, M. V. & Vedantam, S. Comment on how Wenzel and Cassie were wrong by Gao and McCarthy. *Langmuir* **23**, 13242-13242 (2007).
111 De Gennes, P.-G. Wetting: statics and dynamics. *Reviews of Modern Physics* **57**, 827 (1985).
112 Weirauch, D. Interfacial phenomena involving liquid metals and solid oxides in the Mg–Al–O system. *Journal of Materials Research* **3**, 729-739 (1988).
113 Pan, S., Kota, A. K., Mabry, J. M. & Tuteja, A. Superomniphobic surfaces for effective chemical shielding. *Journal of the American Chemical Society* **135**, 578-581 (2012).
114 Xin, B. & Hao, J. Reversibly switchable wettability. *Chemical Society Reviews* **39**, 769-782 (2010).

115 Wang, B., Liang, W., Guo, Z. & Liu, W. Biomimetic super-lyophobic and super-lyophilic materials applied for oil/water separation: a new strategy beyond nature. *Chemical Society Reviews* **44**, 336-361 (2015).
116 Preston, D. J., Song, Y., Lu, Z., Antao, D. S. & Wang, E. N. Design of lubricant infused surfaces. *ACS Applied Materials & Interfaces* **9**, 42383-42392 (2017).
117 Taylor, B. N. & Kuyatt, C. E. *Guidelines for evaluating and expressing the uncertainty of NIST measurement results*. (Citeseer, 1994).
118 Amini, S. *et al.* Preventing mussel adhesion using lubricant-infused materials. *Science* **357**, 668-673 (2017).
119 Cottin-Bizonne, C., Barrat, J.-L., Bocquet, L. & Charlaix, E. Low-friction flows of liquid at nanopatterned interfaces. *Nature Materials* **2**, 237 (2003).
120 Meuler, A. J., McKinley, G. H. & Cohen, R. E. Exploiting topographical texture to impart icephobicity. *ACS Nano* **4**, 7048-7052 (2010).
121 Deng, X., Mammen, L., Butt, H.-J. & Vollmer, D. Candle soot as a template for a transparent robust superamphiphobic coating. *Science* **335**, 67-70 (2012).
122 Quéré, D. Non-sticking drops. *Reports on Progress in Physics* **68**, 2495 (2005).
123 Wang, N. *et al.* Robust superhydrophobic coating and the anti-icing properties of its lubricants-infused-composite surface under condensing condition. *New Journal of Chemistry* **41**, 1846-1853 (2017).
124 Tuteja, A., Choi, W., Mabry, J. M., McKinley, G. H. & Cohen, R. E. Robust omniphobic surfaces. *Proceedings of the National Academy of Sciences* **105**, 18200-18205 (2008).
125 Dufour, R. *et al.* From micro to nano reentrant structures: hysteresis on superomniphobic surfaces. *Colloid and Polymer Science* **291**, 409-415 (2013).
126 Wu, Y., Zhou, S., You, B. & Wu, L. Bioinspired design of three-dimensional ordered tribrachia-post arrays with re-entrant geometry for omniphobic and slippery surfaces. *ACS Nano* **11**, 8265-8272 (2017).
127 Davis, A., Mele, E., Heredia-Guerrero, J. A., Bayer, I. S. & Athanassiou, A. Omniphobic nanocomposite fiber mats with peel-away self similarity. *Journal of Materials Chemistry A* **3**, 23821-23828 (2015).
128 Kim, D. S., Suh, A., Yang, S. & Yoon, D. K. Grooving of nanoparticles using sublimable liquid crystal for transparent omniphobic surface. *Journal of Colloid and Interface Science* **513**, 585-591 (2018).
129 Nhung Nguyen, T. P., Brunet, P., Coffinier, Y. & Boukherroub, R. Quantitative testing of robustness on superomniphobic surfaces by drop impact. *Langmuir* **26**, 18369-18373 (2010).
130 Domingues, E., Arunachalam, S. & Mishra, H. Doubly Reentrant Cavities Prevent Catastrophic Wetting Transitions on Intrinsically Wetting Surfaces. *ACS Applied Materials & Interfaces* (2017).
131 Bocquet, L. & Lauga, E. A smooth future? *Nature Materials* **10**, 334-337 (2011).
132 Rykaczewski, K. *et al.* Dropwise condensation of low surface tension fluids on omniphobic surfaces. *Scientific Reports* **4** (2014).
133 Wier, K. A. & McCarthy, T. J. Condensation on ultrahydrophobic surfaces and its effect on droplet mobility: ultrahydrophobic surfaces are not always water repellant. *Langmuir* **22**, 2433-2436 (2006).

134 Dorrer, C. & Rühe, J. Condensation and wetting transitions on microstructured ultrahydrophobic surfaces. *Langmuir* **23**, 3820-3824 (2007).
135 Jung, Y. & Bhushan, B. Wetting behaviour during evaporation and condensation of water microdroplets on superhydrophobic patterned surfaces. *Journal of Microscopy* **229**, 127-140 (2008).
136 Liu, Y., Chen, X. & Xin, J. Can superhydrophobic surfaces repel hot water? *Journal of Materials Chemistry* **19**, 5602-5611 (2009).
137 Mouterde, T. *et al.* Antifogging abilities of model nanotextures. *Nature Materials* **16**, 658-663 (2017).
138 Dorrer, C. & Rühe, J. Advancing and receding motion of droplets on ultrahydrophobic post surfaces. *Langmuir* **22**, 7652-7657 (2006).
139 Raj, R., Enright, R., Zhu, Y., Adera, S. & Wang, E. N. Unified model for contact angle hysteresis on heterogeneous and superhydrophobic surfaces. *Langmuir* **28**, 15777-15788 (2012).
140 Bielinski, A. R. *et al.* Rational design of hyperbranched nanowire systems for tunable superomniphobic surfaces enabled by atomic layer deposition. *ACS Nano* **11**, 478-489 (2016).
141 Graham, C. *The limiting heat transfer mechanisms of dropwise condensation*, Massachusetts Institute of Technology, (1969).
142 Tammann, G. & Boehme, W. Die Zahl der Wassertröpfchen bei der Kondensation auf verschiedenen festen Stoffen. *Annalen der Physik* **414**, 77-80 (1935).
143 Erb, R. A. *Heterogeneous Nucleation on Single Crystal Silver and Gold Substrates in Cyclic Condensation of Water Vapor*. (University Microfilms, 1965).
144 Mu, C., Pang, J., Lu, Q. & Liu, T. Effects of surface topography of material on nucleation site density of dropwise condensation. *Chemical Engineering Science* **63**, 874-880 (2008).
145 Rodriguez, A. *et al.* Laser interference lithography for nanoscale structuring of materials: From laboratory to industry. *Microelectronic Engineering* **86**, 937-940 (2009).
146 Williams, K. R., Gupta, K. & Wasilik, M. Etch rates for micromachining processing-Part II. *Journal of Microelectromechanical Systems* **12**, 761-778 (2003).
147 Son, J. *et al.* A practical superhydrophilic self cleaning and antireflective surface for outdoor photovoltaic applications. *Sol. Energy Mater. Sol. Cells* **98**, 46-51 (2012).
148 Rosei, F. Nanostructured surfaces: challenges and frontiers in nanotechnology. *Journal of Physics: Condensed Matter* **16**, S1373 (2004).
149 Choi, J. *et al.* Flexible and Robust Superomniphobic Surfaces Created by Localized Photofluidization of Azopolymer Pillars. *ACS Nano* **11**, 7821-7828 (2017).
150 Hensel, R. *et al.* Tunable nano-replication to explore the omniphobic characteristics of springtail skin. *NPG Asia Materials* **5**, e37 (2013).
151 Martyniuk, M. P., Antoszewski, J., Musca, C. A., Dell, J. M. & Faraone, L. in *Device and Process Technologies for MEMS, Microelectronics, and Photonics III.* 451-463 (International Society for Optics and Photonics).
152 Hoffman, D. & Thornton, J. A. Effects of substrate orientation and rotation on internal stresses in sputtered metal films. *Journal of Vacuum Science and Technology* **16**, 134-137 (1979).

153 Harder, T. A., Yao, T.-J., He, Q., Shih, C.-Y. & Tai, Y.-C. in *Micro Electro Mechanical Systems, 2002. The Fifteenth IEEE International Conference on.* 435-438 (IEEE).
154 Allen, M. G., Mehregany, M., Howe, R. T. & Senturia, S. D. Microfabricated structures for the insitu measurement of residual stress, young's modulus, and ultimate strain of thin films. *Applied Physics Letters* **51**, 241-243 (1987).
155 Ylivaara, O. M. *et al.* Aluminum oxide from trimethylaluminum and water by atomic layer deposition: The temperature dependence of residual stress, elastic modulus, hardness and adhesion. *Thin Solid Films* **552**, 124-135 (2014).
156 Raj, R., Maroo, S. C. & Wang, E. N. Wettability of graphene. *Nano letters* **13**, 1509-1515 (2013).
157 Powell, M. J. An efficient method for finding the minimum of a function of several variables without calculating derivatives. *The computer journal* **7**, 155-162 (1964).